ABSTRACT

Title of Dissertation: GROWTH AND CHARACTERIZATION OF SELF-ASSEMBLED FERROMAGNETIC IRON NANOWIRES

Ladan Mohaddes Ardabili, Doctor of Philosophy, 2006

Dissertation Directed By: Professor Ramamoorthy Ramesh

Department of Materials Science and Engineering

In recent years perpendicular ferromagnetic nanowires have attracted considerable interest due to their potential use in many areas of advanced nanotechnology, specifically high-density recording media. An ideal recording medium in this regard consists of a densely organized assembly of nanometer-scale ferromagnets with high magnetization and suitable coercivity.

In this dissertation a novel and simple approach to create self-assembled nanowires of α-Fe through the decomposition of a suitably chosen perovskite is reported. We illustrate the principle behind this approach using the reaction $2La_{0.5}Sr_{0.5}FeO_3 \rightarrow LaSrFeO_4 + Fe + O_2$ that occurs during the deposition of $La_{0.5}Sr_{0.5}FeO_3$ under reducing conditions. This leads to the spontaneous formation of an array of single crystalline α-Fe nanowires embedded in $LaSrFeO_4$ matrix, which grow perpendicular to the substrate.

The embedded iron nanowires are an illustration of three-dimensional heteroepitaxy. The lateral diameter and spacing of the nanowires are strongly dependent on growth temperature. By reducing the temperature of deposition, the size and spacing between the iron nanowires decrease. The changes in the diameter of the nanowires follow an Arrhenius behavior and suggest that the growth of the nanowires is kinetically controlled by diffusion. In addition, their in-plane shape evolves from circular to octahedral and square shape with [110] facets dominating as the growth temperature increases and the elastic energy dominates over the surface energy.

The iron nanowires exhibit square shaped out-of-plane hysteresis loops with a relatively large uniaxial anisotropy with the easy access normal to the film plane. The calculated anisotropy field indicates that the anisotropy observed is due to the cylindrical shape of the nanowires and shape anisotropy.

The nanowires are also used as the nucleation sites for growth of vertically aligned multi-walled carbon nanotubes for field emission applications. The diameter and shape of the carbon nanotubes are controlled by the diameter and length of the nanowires.

It is believed that this approach to self-assembly of the ferromagnetic nanowires is generic and can be expected to yield epitaxial nanocomposites from other complex oxides as well. This opens a new and exciting path for processing of a broad range of nanomaterials through self-assembly.

GROWTH AND CHARACTERIZATION OF SELF-ASSEMBLED FERROMAGNETIC IRON NANOWIRES

By

Ladan Mohaddes Ardabili

Dissertation submitted to the Faculty of the Graduate School of the
University of Maryland, College Park, in partial fulfillment
Of the requirements for the degree if
Doctor of Philosophy
2006

Advisory Committee:

Professor Ramamoorthy Ramesh, Chair/Advisor
Professor Mohamad Al-Sheikhly
Associate Professor Sheryl Ehrman
Professor Lourdes Salamanca-Riba
Professor Manfred Wuttig

DEDICATION

To my mother for all her love and sacrifices

To my father for always believing in me

To my sister and brother for whom I would do anything

I miss every moment living without them all

And

To my partner Greg for every moment we share

ACKNOWLEDGEMENTS

I would like to acknowledge my advisor, Professor Ramesh, and thank him for giving me the opportunity to work on this project. I learned a lot working in his lab and also during our move from Maryland, when we packed all of our lab equipment and then set everything up in Berkeley, with only a few other lab members. During working with him and throughout my PhD period I gained a lot of self-confidence and learned that I can do anything if I set my mind to it.

I am deeply grateful to Professor Mohamad Al-Sheikhly. He has been not only my advisor and teacher but also my friend. I thank him for having faith in me and believing in my abilities and always encouraging me to advance further.

I would like to thank Professor Lourdes Salamanca-Riba for patiently reading all my papers and revising them during my M.Sc. and PhD programs. I have a great deal of respect for her, and her conduct as a Professor is a model for me.

I am also grateful to Professor Wuttig for helping me in better understanding and interpreting my results and also patiently reading my papers even when he was on his sabbatical.

I would also like to thank Dr. Satish B. Ogale for all his guidance and help on my project during the time I was in Maryland. I admire his knowledge and passion for research. I enjoyed working with him very much and I learned that any experimental results are important and can be scientifically interpreted in a way that will enrich the research.

I would like to thank Professor Sheryl Ehrman for agreeing to be on my PhD committee and also taking the time in her busy schedule to evaluate my work.

I would like to acknowledge the important contribution of Professor Béatrice Hannoyer at Université de Rouen in France for Mössbauer spectroscopy measurements and all the scientific and fun discussion we have had by e-mail.

I am grateful to Professor Darrell G. Schlom and Professor Samuel E. Lofland for their scientific input and valuable assistance in my research.

I would like to acknowledge and thank all the group members and friends at University of Maryland, especially Dr. Haimei Zheng, Dr. Seung-Yeul Yang, Dr. Florin Zavaliche, Dr. Tong Zhao, and Dr. Zhengkun Ma for all their contributions and with whom I have great memories and will always look forward to hearing about their achievements.

I want to thank and acknowledge all the new group members at UC Berkeley specially Qian Zhan for doing the TEM analysis. I would also like to thank Rajesh Chopdekar, in Dr. Suzuki's group, for all his help in teaching me SQUID and accommodating my needs when I had to do an urgent measurement.

I would like to acknowledge the National Science Foundation for providing me with the EAPSI fellowship to conduct research in Korea in summer of 2005. This was one of my best experiences in graduate school. I learned a lot on how research is done in the Far East and a lot about their history and culture. This experience has changed the way I perceive many things in life and I owe it to NSF, my host in Korea Professor Yoo and all the wonderful graduate students and scientists at SungKyunKwan University, as well as all the other NSF fellows and friends.

I would like to specially thank all my wonderful friends, the ones who left Iran with me and immigrated, specially Leila, Reza, Amirali and Mariam, for always

being there for me in all the efforts we made to settle down, for all the laughter and cries we shared and for all our reunions; the ones who chose to stay, for always remembering me and for their courage and struggles to make a better life; to the ones whom I got to know here in my new life, for all the happiness and richness they have brought to my life.

I would also like to thank my uncle, Mohammad Mohaddes, for helping me in moving to US. Without his efforts I would have not been here.

I am genuinely grateful to Professor Mohammad Modarres for helping me in the admission process. He was the miracle that I believed it would happen.

I am always grateful to Amirsa Amjadi for everything we have shared, for teaching me to see the world in a deeper and different way and for letting me go although he knew he would lose me.

I would like to thank Debbie Savage, for all her love and support and for all the kind things she has done for me during all these years. I am so happy that she is part of my family.

I would like to thank my father, Ali, for everything he has done for me and for what he is always proud of: raising me independently; my mother, Nasrin, for all her love and support and all the things she does that make me laugh; my sister, Solmaz, for being so kind and caring and for coming here to be with me for the last months of my studies which has been a great motivation for me to finish; and my brother, Reza, for all the great memories I have from him and for every moment he has made me laugh.

And finally, I thank my partner Greg Pugliese for all his love and support during my graduate studies and for making my life in United States so meaningful.

TABLE OF CONTENTS

LIST OF TABLES

LIST OF FIGURES

Chapter 1 Introduction

1.1 Magnetic nanostructures

Nanostructured materials have attracted intense research interest over the past few years, as they provide the critical building blocks for the booming nanoscience and nanotechnology industries. They typically have structural or chemical restrictions on the nanometer scale along one or more of the dimensions. Recent progress in magnetism and magnetic materials has made magnetic nanostructures a particularly interesting class of materials for both scientific exploration and technological applications. Research on magnetic nanostructures has driven the sample physical size towards ever-smaller dimensions.

Fundamentally, novel properties emerge as the sample size becomes comparable to or smaller than certain characteristic dimension scales, such as spin diffusion length, carrier mean free path, magnetic domain wall width, superconducting coherence length, etc. Interest in the study of these fascinating properties has been driven by the success of the semiconductor microelectronics industry, in several different ways. First, demand for magnetic hard disk data storage has grown commensurately with the spread and increase in the capabilities of microprocessors. Hard disks store their data at submicron scale magnetic domains. A detailed understanding of magnetism on the nanometer scale is therefore essential for developing new hard disks. Moreover, it is generally thought that the current growth in performance of hard disks (60–100% per annum compound increase in storage density) can only be sustained into the future if the hard disk itself is replaced by a

massive array of magnetic nanoelements[1]. Second, the art and science of fabricating magnetic structures on the nanometer scale have benefited in large from the exponential shrinking in size of the integrated circuit transistor in accordance with Moore's Law, which has lead to enormous investment in optical and electron beam lithography. Third, the semiconductor industry may itself in the future benefit from nanomagnetism. Many of the problems currently facing future reduction in size of integrated circuits, such as the diminishing number of carriers present in a transistor gate and difficulties in removing heat, may be solved by combining magnetic elements into microchips[2]. This will probably initially be in the form of non-volatile computer memory called MRAM (magnetic random access memory). The recent discovery [3] of the spin polarized current injection from a ferromagnet into a semiconductor means that in the future we may see fully hybrid magnetic–electronic devices which use the spin of the electrons as much as their charge to perform logic operations and processing. Nanomagnets may ultimately even provide a suitable environment for implementing quantum computation[4].

In addition to applications such as data storage in computer and semiconductor industry, magnetic nanostructures are being used in fields as diverse as biology and biotechnology. In these applications, the ability to control particle size, shape, composition, and surface chemistry is critical in obtaining the desired magnetic properties. Suspensions of superparamagnetic particles are of interest in applications such as ferrofluidics[5]. In biomagnetics, superparamagnetic particles are used commercially for cell sorting and are being explored for radiation treatment[6]. Magnetic particles have been used in magnetic tweezers where the force required to

displace magnetic particles bound to cells or proteins and can be used to probe the micromechanics of cells and the torsion of DNA molecules[7,8]. Such particles are also being explored for use in drug delivery and gene therapy[9].

As a result, a significant amount of research has been performed in recent years to address different aspects of magnetic nanostructures, from fabrication to characterization, both theoretically and experimentally[10]. Essential to nanofabrication has been lithography, a term for several closely related processes, including mask design and patterning, resist coating, exposure, and development. But as the device miniaturization trend continues, new sample growth and patterning methods such as self-assembly have been needed to fabricate ferromagnetic nanostructures by efficient growth processes that may allow the realization of length scales far below the limits of conventional photolithography. In this dissertation a simple in-situ growth mechanism for fabrication of ferromagnetic nanowires is introduced which does not rely on photolithography and may open a new avenue for the processing of several ferromagnetic nanostrucures.

1.2 Ferromagnetic nanowires

Magnetic nanowires are interesting for both fundamental science and potential applications in many areas of advanced nanotechnology, including patterned magnetic media[11], magnetic devices and materials for microwave applications. In contrast to unpatterned films and spherical particles, one-dimensional magnetic nanostructures (nanorods or nanowires) exhibit degrees of freedom associated with

their inherent shape anisotropy and their ability to incorporate different components along their length. Therefore, ferromagnetic nanowires exhibit unique and tunable magnetic properties that are very different from those of the bulk ferromagnetic materials, thin films, and spherical particles. As an example, the increase in coercivity, changes in domain structure and reversal mechanisms, quantization of spin wave modes, or dipolar interaction effects can be pointed out. Moreover, fabrication of tailored lines with modified shape has allowed the study of other topics, such as the contribution of the domain wall to the magnetoresistance, the speed of domain wall motion, or different giant magnetoresistance effects.

The introduction of multiple segments along the length of a nanowire can lead to further degrees of freedom associated with the shape of each segment and the coupling between the layers. Both single-component and multiple-segment magnetic nanowires are of interest in these emerging fields, since magnetic properties such as the orientation of the magnetic easy axis, Curie temperature, coercivity, saturation field, saturation magnetization, and remanent magnetization can be tailored by modifying the diameter, shape, composition, and layer thicknesses in multiple-segment ferromagnetic/nonmagnetic nanowires.

Fabrication of periodic arrays of magnetic nanoparticles, nanodots and nanowires started with nanolithography. E-beam lithography was used to fabricate arrays of pillars on silicon. An example of the early work in this field is the fabrication of Ni nanopillars with diameter of d = 35 nm and height of l = 120 nm which were developed by e-beam lithography. A schematic of the e-beam lithography and SEM images of the Ni nanopillars is shown in Fig.1.1[12]. Hehn et al.[13] patterned

single crystalline Co films by x-ray photolithography and made Co nanodots with diameter of 500 nm. Since then, novel lithography techniques have been developed or improved to allow fabrication of ordered magnetic nanostructures with desirable features, including arrays of elements with reproducible sizes in the range of 10 nm, which can be extended over large areas. Often there are many variable parameters that can be used to tune the properties of these nanoelements, such as material's crystallinity (polycrystalline, single crystal, amorphous), structure (single layer, multilayer, etc), array geometry, etc. Also, magnetic nanostructures can be prepared with very controllable shape: from the simplest dots, bars and lines, to rectangles, triangles or zigzag paths.

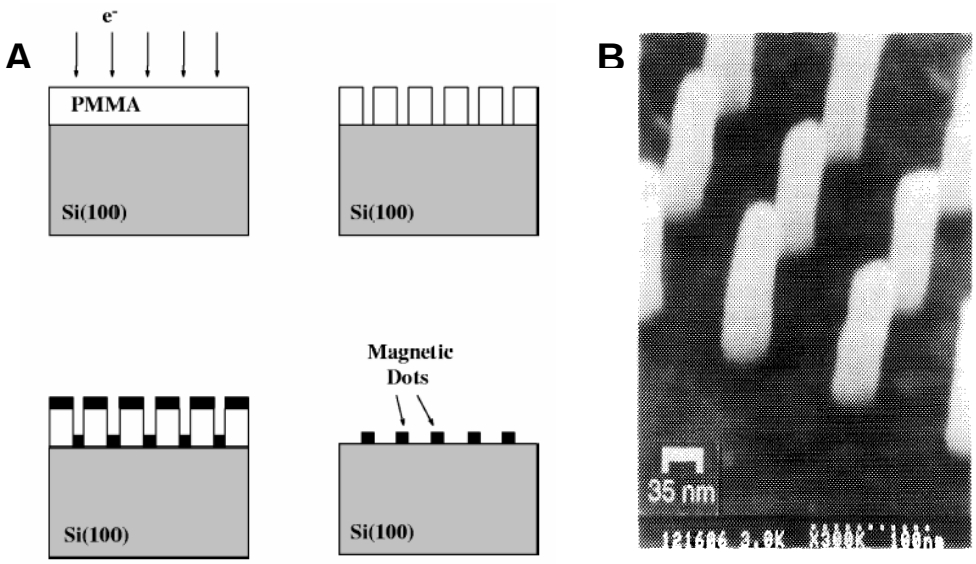

Fig.1.1 A. Schematic of the photolithography process for the nanodot and nanowire formation[12], B. SEM image of the Ni nanowires fabricated through e-beam lithography.

Lithographically defined nanowires have the advantage that their location, size and spacing can be precisely controlled. However the aspect ratio is typically low. In addition, photolithography is comparatively tedious, expensive and not suitable for large-area production.

In recent years an alternative approach has been developed to fabricate ferromagnetic one-dimensional nanostructures using porous media such as molecular sieves[14], track-etched polymer membranes and porous anodic aluminum oxides (alumite)[15,16,17] as a template. This approach is suitable for large-area production of nanowire arrays with high aspect ratios. In the case of nanowires, porous alumina templates are of significant interest due to containing higher pore density and uniformity of the pore distribution. Porous alumina substrates are fabricated by anodizing aluminum in an acidic electrolyte such as sulfuric, oxalic, or phosphoric acid with pH < 4. During the anodization process, the pores nucleate randomly on the surface with a broad size distribution. However, under specific conditions, highly ordered hexagonal arrays are produced. Depending on the anodization condition, the pore diameter can be controlled and ranges from 4 to 200 nm. The pore length can also be varied from 20 nm to 1 μm. Ferromagnetic materials, such as Fe, Co, Ni and their alloys, can be easily electrodeposited into these cylindrical pores using aqueous salt solutions, such as $FeSO_4$ and $CoSO_4$. Magnetic multilayered nanowires such as Co/Cu, Fe/Cu or NiFe/Cu can also be fabricated using this method. In this approach, the metals are deposited from a single solution (single-bath) by switching between the deposition potentials of the two constituents.

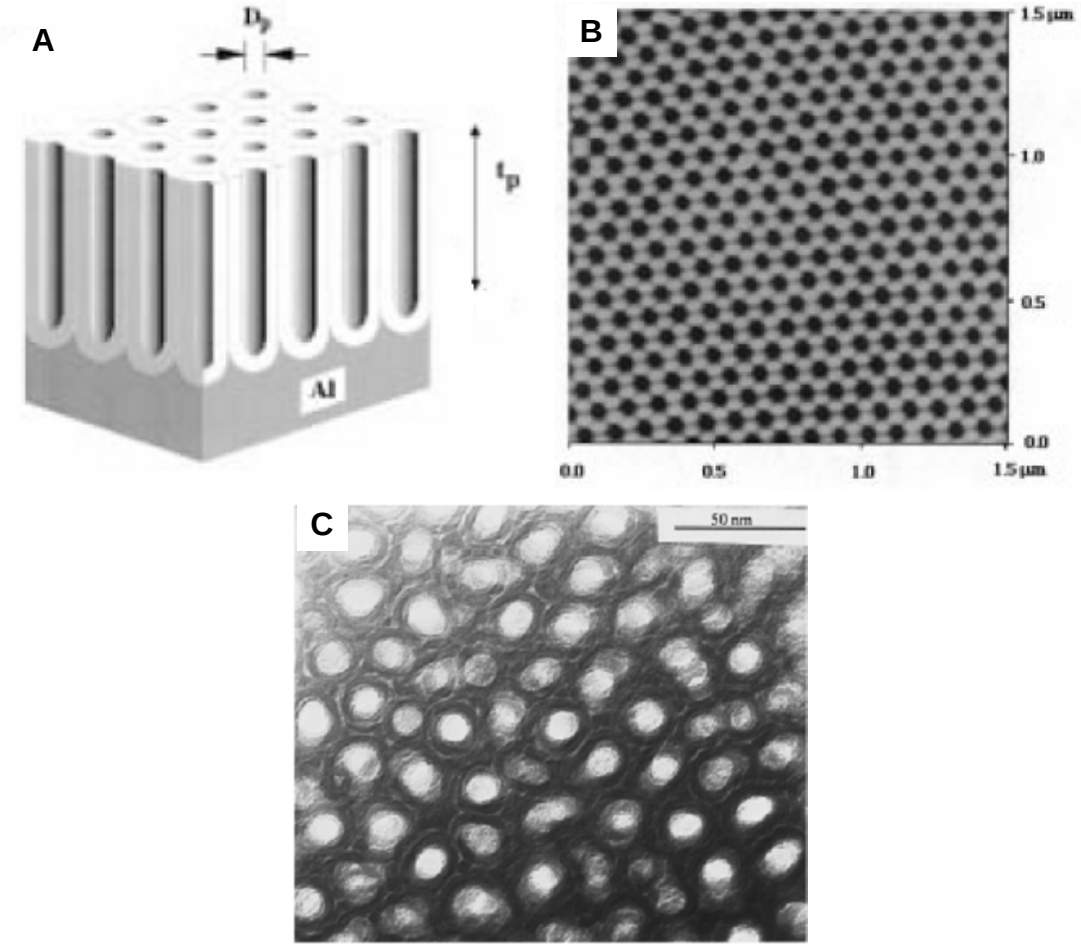

Fig.1.2 A. Schematic of the alumite template for electrodeposition of the ferromagnetic nanowires; B. AFM image of the nanopores; C. TEM image of the iron nanowires electrodeposited in the pores of alumite template.

Fig.1.2 shows atomic force microscopy (AFM) and transmission electron microscopy (TEM) top view images of the nanopores and electrodeposited metal nanowires. Each

electrodeposited nanowire is reported to be polycrystalline, which consists of a chain of single-crystallite segments. High-resolution TEM studies of the nanowires freed from the aluminum oxide template indicate that the nanowire surfaces are not free of defects and inhomogeneities. In addition, electrochemically produced nanowires exhibit a length distribution. These factors greatly influence the magnetic properties of the nanowire arrays and interpretation and theoretical modeling of their magnetic behavior.

Therefore, although the electrodeposition of ferromagnetic metals in alumite template is a promising method, there still exists the need for a single step, time effective method for the fabrication and processing of defect-free and homogeneous nanowires. With respect to this, the notion of self-assembly holds great potential for developing such nanostructures and tailoring their physical properties.

1.3 Present approach: self-assembly of ferromagnetic nanowires

As mentioned above, an ideal recording medium consists of a densely organized assembly of nanometer-scale ferromagnets with high magnetization and suitable coercivity[11]. The formation of such a structure could either be process-directed or self-enabled. While the former is more definitive and controlled, the latter is more desirable and convenient from the standpoint of ease of implementation, scaling up, and cost-effectiveness. There are many examples of process-directed perpendicular nanowires, including those mentioned earlier in section 1.2, in which porous aluminum oxide films are used as a template and ferromagnetic metals such as Fe, Co

and Ni are electrodeposited into the pores of the alumina film[18]. However, much less effort has been put into the self-assembly of perpendicular ferromagnetic nanowires preferentially by themselves.

The formation of nanostructured materials by self-assembly is an attractive processing method, both scientifically and also for industrial applications. In contrast to artificially formed and ordered structures, self-assembly holds promise in that it relies on the system's intrinsic ability to organize itself into ordered patterns. Therefore, the formation of nanostructures through self-assembly has been a topic of experimental and theoretical studies for the past decade.

In this dissertation a simple and novel approach to produce single crystalline ferromagnetic nanowires by means of self-assembly in heteroepitaxial thin film growth is explored[19,20]. The approach is based on the combination of two principles. The first principle is based on the phase control under reduction of perovskite-type oxides of general formula $LaMO_3$ where M is a group VIII metal. The second principle is derived from three-dimensional heteroepitaxy in the nanostructure thin film growth. In this work, the results of these two concepts applied to a single-phase perovskite $La_{1-x}Sr_xFeO_{3-x}$ system are presented. By choosing optimum deposition conditions and oxygen pressure and also a suitable substrate it is shown that it is possible to obtain single crystalline ferromagnetic nanowires with a one step process in a time effective manner.

1.3.1 Reduction of perovskite $LaMO_3$

1.3.1.1 Introduction

In the early 1980's perovskite-type oxides of the general formula $LaMO_3$ (where M is a group VIII metal) gained significant interest as they were used for the oxidation of carbon monoxide and hydrocarbons. These oxides were shown to be very active and selective catalysts for methanol and alcohol synthesis from carbon monoxide (CO) and H_2. Therefore, the reduction of the $LaMO_3$ perovskite oxide series was intensively studied to determine the relationship between reducibility and catalytic activity of the oxides for the oxidation reactions.

Accordingly, it has been shown that these perovskite oxides in bulk form can be reduced to stable compounds having a charge of 1 to 3 electrons per molecule. The fully reduced state of the $LaMO_3$ perovskite is defined when a metal (M) embedded in the La_2O_3 matrix is obtained[21]. This is therefore the reduction of 3 electrons per molecule as shown in the reaction below:

$$2LaMO_3 + 3H_2 \rightarrow 2M + La_2O_3 + 3H_2O \qquad \text{Eq.1.1}$$

This reduction is kinetically controlled by formation and growth of nuclei of metallic species (in the case of full reduction) on the surface of the perovskite grains.

The results of the reduction in 10^{-6} Torr for some important members of $LaMO_3$ are reviewed here. The most easily reducible members of this series are $LaCoO_3$ and $LaNiO_3$. Both perovskite oxides reduce to 3 electron per molecule at relatively low temperatures of around $T = 773$ K resulting in the formation of Co and Ni metals embedded in a La_2O_3 matrix. The second most easily reducible in this oxide series is $LaFeO_3$ which reduces to α-Fe embedded in La_2O_3 oxide at a higher

temperature of T = 1250 K. In the case of $LaMnO_3$, the perovskite reduces only 1 electron per molecule at T = 1073 K and results in the formation of manganese oxide (MnO) in addition to La_2O_3. In some cases the perovskite is not easily reducible even at high temperatures; an example is $LaCrO_3$ which reduces only 0.013 electron per molecule at T = 1250 K. The reducibility of these oxides is summarized in Table 1.1.

Perovskite Oxide	Reduction (e^- per molecule)	Reduction Temp. (K)	Reduction Product
$LaCoO_3$ $LaNiO_3$	$3e^-$	773	La_2O_3 + Co La_2O_3 + Ni
$LaFeO_3$	$3e^-$	1250	La_2O_3 + Fe
$LaMnO_3$	$1e^-$	1073	La_2O_3 + MnO
$LaCrO_3$	$0.013e^-$	1250	---

Table 1.1 The reduction of several perovskite oxides with general formula of $LaMO_3$ where M is a transition metal.

The results of this reduction based phase decomposition can be applied to thin film growth. The phase decomposition if combined with the heteroepitaxy principle in thin film growth can be a useful factor in engineering nanostructures. Depending on the oxidation state of M, these oxides provide an interesting opportunity to create metallic or oxide nanostructures embedded in another complex oxide matrix through

spontaneous phase decomposition. In this dissertation, these two principles are applied to a single-phase $La_{1-x}Sr_xFeO_{3-x}$ perovskite oxide and the structure, chemical status and physical properties of the resulting compounds, iron and $LaSrFeO_4$, are studied. The remarkable feature of such nanostructures is the epitaxial orientation relationship between both phases and the substrate which results in the vertical growth of embedded nanostructure in the form of pillars. We show that this approach is generic and can be expected to yield epitaxial nanocomposites from other complex oxides as well.

1.3.1.2 Properties of the $LaSrFeO_3$ perovskite

The perovskite series of general formula $LaMO_3$ (M = transition metal) constitutes one of the most interesting classes of solids, exhibiting a variety of structures and properties. The nature of metal-oxygen bonding can vary from nearly ionic to highly covalent or metallic. The unusual properties of transition metal oxides are clearly due to the unique nature of the outer d-electrons. The recent interest in transition metal oxides has been mainly due to the discovery of high-temperature superconductivity in curparates and giant magnetoresistance (MR) in manganese oxides which are both due to strong electron correlation. Mixed valence of the transition metal ions can be induced in $LaMO_3$ compounds in two ways: 1) by introducing divalent ions such as Ba, Ca, or Sr at the trivalent La site or 2) by creating oxygen vacancies.

The magnetic properties of these compounds are thought to arise from a super exchange mechanism involving 3*d* electrons of the transition metal ions and oxygen *p*

orbitals. Thus oxygen plays a very important role in magnetic ordering of these compounds[22].

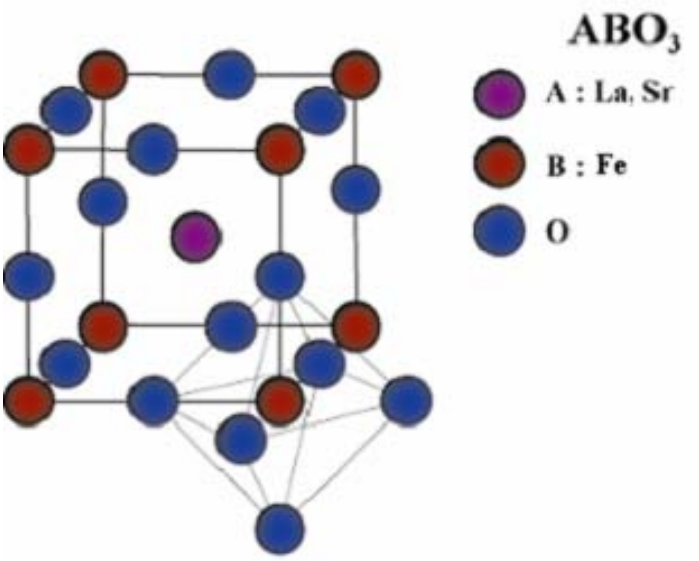

Fig.1.3 Schematic of the $La_{1-x}Sr_xFeO_3$ perovskite unit cell.

$La_{1-x}Sr_xFeO_3$ is an interesting oxide in this group and belongs to the family of mixed-valent transition metal oxide perovskites that support a large oxygen non-stoichiometry and high diffusivity of oxygen ions[23]. A schematic of the $La_{1-x}Sr_xFeO_3$ perovskite unit cell is shown in Fig.1.3 with octahedron O ions on the faces, Fe ions on the corners and La (Sr) ions in the center. The parent material is perovskite $LaFeO_3$ with orthorhombic structure which is a charge transfer type insulator with an energy band gap of 2 eV. It is also antiferromagnetically ordered with a high Néel temperature of around T_N = 750 K and exhibits a weak parasitic ferromagnetism due

to a small canting of the Fe ion magnetic moment. On substituting trivalent La (La^{+3}) with divalent Sr (Sr^{+2}), the orthorhombic perovskite structure becomes pseudocubic for $x \geq 0.4$ in $La_{1-x}Sr_xFeO_3$. Strontium substitution forces the Fe ions into a 4^+ state which is believed to weaken or even destroy the magnetic ordering. Also, on substituting Sr the activation energy of the semiconducting compounds and the antiferromagnetic Néel temperature decreases systematically for increasing Sr content.

It is important to note that while $La_{1-x}Sr_xMnO_3$ and $La_{1-x}Sr_xCoO_3$ become metallic for $x \geq 0.2$, $La_{1-x}Sr_xFeO_3$ does not exhibit a metallic phase until $x \approx 1$. Therefore, only stoichiometric $SrFeO_3$ is metallic but still exhibits antiferromagnetism with Néel temperature around $T_N = 134$ K[24]. $LaFeO_3$ perovskite and its related compounds have been shown to act as good membrane materials that allow transport of oxygen ions.

In this dissertation, perovskite $La_{1-x}Sr_xFeO_3$ with $x = 0.5$ has been used as the target material for the reduction mentioned in Eq.1.1 and the growth of self-assembled iron nanowires embedded in an oxide matrix using the pulsed laser deposition (PLD) method.

1.3.2 Three-dimensional heteroepitaxy in thin film growth

The concept of spontaneous nanostructure formation has been comprehensively studied in metals[25,26,27] and also semiconductor systems[28,29,30]in which significant amount of research has been carried out on the self-assembly and self-organization of these nanostructures on the semiconductor surfaces during epitaxial growth.

Accordingly, the spontaneously formed nanostructures had been classified into five different groups. These groups as shown in Fig.1.4[28] are: 1) periodically faceted surfaces (Fig.1.4 A), 2) periodic structures of planar domains, and monolayer high islands (Fig.1.4 B), 3) ordered arrays of three-dimensional coherently strained islands in lattice-mismatched heteroepitaxial systems (Fig.1.4 C), 4) multisheet arrays of two-dimensional islands (Fig.1.4 D), and 5) multisheet arrays of three-dimensional islands (Fig.1.4 E).

In Fig.1.4 E a particularly interesting mode of self-assembled growth is demonstrated. In this mode it is observed that the nanodots formed in successive layers show a tendency to stack in a vertical manner due to the lateral modulation of the strain. An example is the self-organization of the InAs on GaAs (100)[31]. The initial two-dimensional self-assembly therefore evolves progressively into a three-dimensional self-assembly.

In thin film processing, the embedded nanostructure and the surrounding matrix can be epitaxial with respect to each other as well as to the substrate, providing the possibility of heteroepitaxy in three-dimensions. This depends on the intrinsic similarity in crystal chemistry between the two resulting phases, their close crystal structure and lattice constant and also their ability to behave like line compounds with little solubility into each other. By selecting a suitable common substrate with similar crystal structure and close lattice match with nanostructure and matrix phases, an exciting opportunity for three-dimensional heteroepitaxy (i.e. both in-plane and out-of-plane) can be created. The initial two-dimensional in-plane self-assembly in these

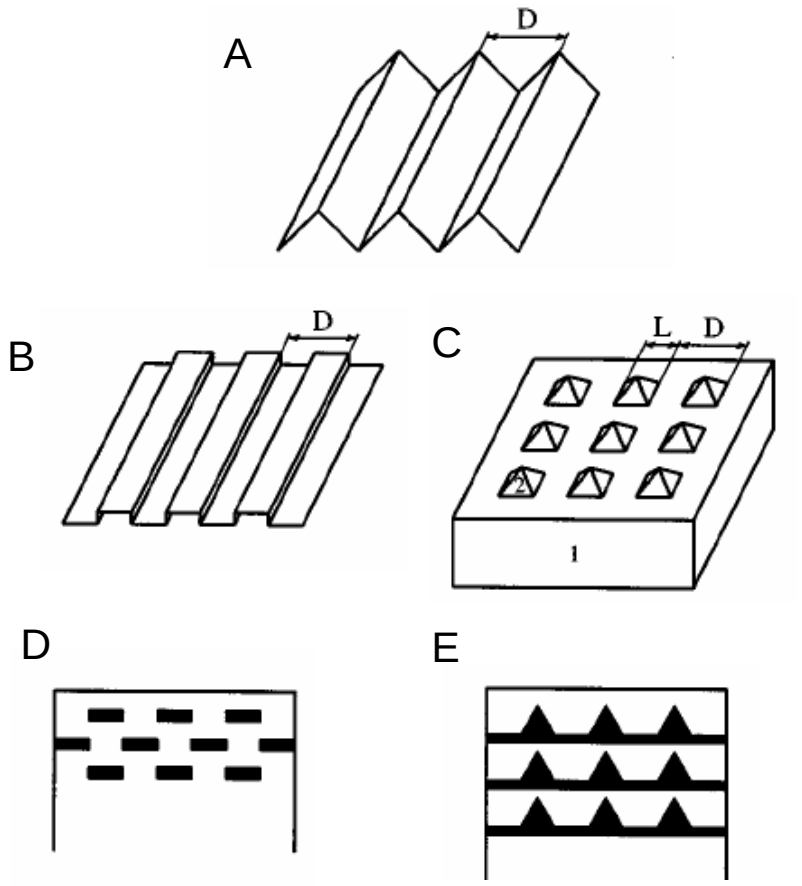

Fig.1.4 Various classes of spontaneously ordered nanostructures[28]: A. periodically faceted surfaces; B. surface structures of planar domains; C. ordered array of three-dimensional coherently strained islands 2 lattice-mismatched to the substrate 1; D. cross-sectional scheme of a multisheet array of twodimensional islands; E. cross-sectional scheme of a multisheet array of three-dimensional islands.

composite systems evolves progressively into three-dimensional self-organization and therefore leads to the formation of the embedded epitaxial and single crystalline nanopillars.

In this dissertation, the two concepts discussed in section 1.3.1 and 1.3.2, namely, the reduction of $La_{0.5}Sr_{0.5}FeO_3$ perovskite-type oxides and three-dimensional heteroepitaxy in nanostructures, are combined. These two aspects present an interesting opportunity to create metal-oxide nanostructures through a spontaneous phase decomposition process. In the course of thin film growth, the two resulting phases can be epitaxial simultaneously with respect to each other as well as with to a common substrate. By selecting a suitable substrate, such as $SrTiO_3$ and $LaAlO_3$, the growth condition can be tuned in such a way that the heteroepitaxy in three-dimensions (meaning both in-plane as well as out-of-plane) will be possible in the thin film growth process.

This experiment was previously performed on $La_{1-x}Sr_xMnO_3$ [32] where the authors were studying the effect of oxygen deficiency on magnetic and electrical transport properties of this perovskite oxide. In their attempt to study the effect of the absence of oxygen during the thin film growth process, they found that the growth of the provskite in the reducing environment resulted in the formation of the MnO nanowires embedded in a tetragonal oxide matrix.

Therefore, although self-assembly and processing of vertically aligned nanostructures in this manner is not a completely new idea, it is still a challenge to synthesize these nanostructures in complex oxide systems in such a way as to have total control over their position, shape, size and spacing so that the properties of the nanostructures can be tailored for a specific desired application. Furthermore, the mechanism of the in-plane self-organization in even the simplest semiconductor thin film systems is still not very clear and needs further careful investigation.

This concept was further applied to the self-assembly of multiferroic nanocomposites, where a ferromagnetic nanopillar is embedded in ferroelectric matrix or vice versa[33,34]. The coexistence of magnetic and electric subsystems builds a material with the "product" property (i.e., the composite exhibits responses that are not available in the individual component phases), thus allowing an additional degree of freedom in the design of actuators, transducers, and storage devices.

1.4 Applications of self-assembled iron nanowires

As mentioned above there are many applications for magnetic nanowires and nanorods such as magnetic devices, materials for microwave applications, drug and gene delivery, and magnetic storage media. This dissertation is written at the time that hard drive manufacturers such as Hitachi and Seagate are making a transition towards perpendicular recording media. It is therefore necessary to point out the importance of studying and fabricating ferromagnetic nanowires with respect to their prospective applications in this industry. In addition, a new type of nanosize microwave oscillator based on the spin-torque and phase-locking effects in self-assembled arrays of magnetic nano-contacts is proposed and reviewed.

1.4.1 Perpendicular recording media

With the thermal stability limit for magnetic recording in conventional longitudinal recording media reaching its maximum predicted values, alternative technologies

have to be considered to allow data densities to continue to increase. Linear density limits are currently determined by the medium noise. The power signal-to-noise ratio (SNR) is determined by the number of grains which build a single bit. For a fixed bit size, the number of grains and SNR could be increased by reducing the dimensions, but this approach is limited by the thermal stability of the magnetized bit, which is mainly determined by the demagnetizing fields and by the energy barrier to magnetization reversal for a magnetic grain. This limit could be relaxed to the superparamagnetic limits if a bit consisted of a single and isolated magnetic unit.

Perpendicular recording improves areal density by re-orienting the data bits so that the north and south poles of the data bits are no longer in a line parallel to the media (longitudinal), but instead perpendicular to the media's surface. This re-orientation allows for a higher recording density and eliminates the issues of data stability of concern in longitudinal recording. Such an ideal magnetic medium would consist of ferromagnetic islands of nanometer scale, placed in an ordered fashion.

As mentioned in section 1.2, lithography and anodized alumina templates are the two known methods to fabricate this perpendicular ordered array geometry. Another candidate material and fabrication method for perpendicular media is Co-alloy. Much of the investigations so far have been based around systems associated with CoCr alloys [35,36]. However, due to the nature of the columnar growth in such systems the tribology performance of such media has been poor, promoting large head to medium separation and hence limiting data density. The CoCr-alloys are deposited on an epitaxial soft underlayer using dc-sputtering. As film growth proceeds, each crystallite exhibits CP (chrysanthemum like pattern) structure with a

periodic stripe pattern. Only crystallites with Cr-rich cores survive. A dense columnar structure with a strong out-of-plane (0001) hcp orientation is obtained which maximizes the perpendicular magnetocrystalline anisotropy[37,38]. A TEM image of the columnar structure in CoCr-alloy is shown in Fig.1.3. This is related to Cr segregation at the grain boundaries. The CP structure growth process is explained using a model based on (1) a phase separation process restricted by grain boundary and surface diffusion, and (2) grain boundary Cr enrichment at the latter stage of segregation. The correlation between CP structure growth and the change in magnetic properties strongly indicates that the perpendicularly formed CP structure is responsible for the magnetic properties of Co-Cr films[39].

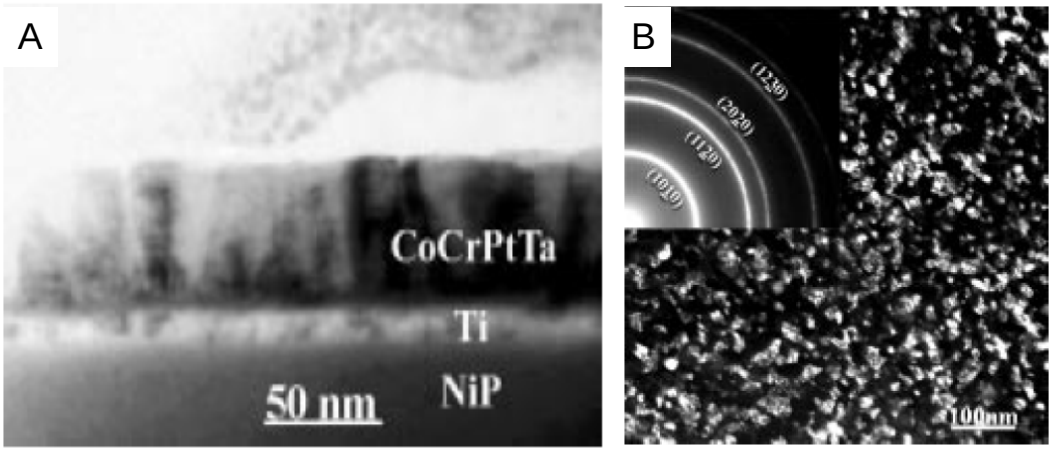

Fig.1.5 A.TEM cross-section image of sputtered columnar CoCr-alloy/Ti bilayer for perpendicular recording media, B. Plan-view dark field image and EDP of CoCrPtTa/Ti on NiP/Al substrate[37].

The storage density of a hard drive, also known as areal density, is measured in terms of data bits per square inch (bin^{-2}) of storage surface. Present longitudinal drives may offer areal densities of 110 $Gbin^{-2}$, and with Seagate's recent initial release of perpendicular drives, an increase to 132 $Gbin^{-2}$ has already been achieved. This instant increase of 20% is trivial considering the potential that this technology will offer in the future. Seagate has successfully demonstrated the ability to provide 245 $Gbin^{-2}$ with perpendicular recording (with a data rate of 480 Mbits per second), and sometime in the near future it is expected that 500 $Gbin^{-2}$ will become a reality.

In addition to an increase in data storage density, there are other important benefits in using perpendicular recording drives compared to conventional longitudinal drives. The improvement in shock tolerance, reduction in power consumption, decrease in noise level, requirement for fewer parts and higher reliability are other important advantages of switching to perpendicular recording media.

In this respect, ordered arrays of self-assembled iron naowires with high magnetization and large magnetic anisotropy coupled with the sizeable coercive field can be desirable candidates for probe based data storage systems.

1.4.2 Compact tunable microwave oscillators in magnetic nano-contact arrays

The emergence of novel electron dynamics phenomena at the nanoscale creates a unique opportunity for theoretical and experimental research to develop a new class

of compact, electrically tunable, narrow band microwave oscillators. A self generated microwave response was recently discovered when a low level dc current was injected into a nanoscale hard-soft magnetic multilayer thin film structure in such a way as to produce highly coherent microwave frequency spin precession in the soft, or free, layer. The response derives from a spin momentum transfer (SMT) or spin-torque (ST) effect in which the spin polarization of the electrons acquired in the course of electron propagation in the hard (fixed) magnetic layer drives a microwave magnetization precession in a soft (free) magnetic layer of the multilayer structure. This, in turn, produces a microwave voltage oscillation through the giant magnetoresistance in the structure. Fig.1.6 shows the general scheme for the current injection, the spin polarization due to a hard or fixed magnetic layer, and the current driven precession realized in the free layer. It should be noted that the electrons are injected from the top, into the free layer. It is the back reflected polarized electrons that drive the precession indicated in the diagram. If the current level is sufficiently high, the injected spin polarized electrons result in a nonlinear gyroscopic precession of magnetization in the free layer. This precession has a rather narrow spectral width. This response and the corresponding giant magnetoresistance (GMR) generated microwave power is obtained only when the current exceeds some threshold, typically in the range of 10^8 A/cm^2 or so. This is a truly nanoscale phenomenon. The high current densities required for the coherent nonlinear precession can only be realized at practical levels of currents through the use of nanosized contact regions on the scale of tens of nanometers.

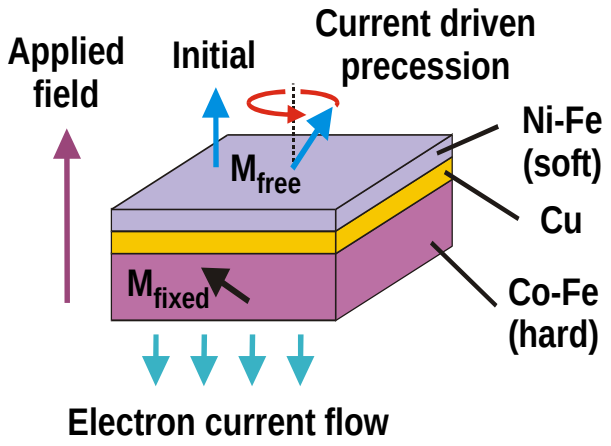

Fig.1.6 Schematic of spin torque process diagram showing Co-Fe (hard) and a Ni-Fe (soft) magnetic multilayer film with fixed and free magnetizations, respectively. Electron injection in the top free layer and spin polarization in the fixed layer yields a nonlinear spin-polarized driven microwave precession.

Such an excitation of spin waves in the microwave and millimeter frequency range by a spin-polarized current was first predicted by Slonczewski and Berger[40,41]. Since then the experimental realization of this novel microwave response has been demonstrated by several groups[42,43,44]. One can use either an extremely narrow pillar shaped film structure to constrict the current, or one can use a wide area film and achieve the needed current densities through the use of a nano-contact. Therefore, spin-current driven magnetization precession in a soft magnetic layer fabricated as part of a nano-contact structure offers unique opportunities for new devices. The major drawback to applications is in the fact that the generated microwave power is

typically very small, on the order of 0.1 nano-Watt or less. This problem can be resolved through phase-locking[45] which arises from the fact that the responses from nano-contact structures in close proximity can be phase locked. It is shown that one can phase lock the self-generated signal to an external microwave reference signal over a fairly wide range of control parameters.

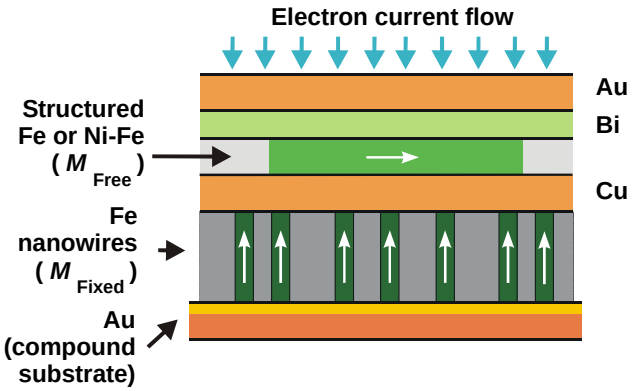

Fig.1.7 Schematic view of the dual function magnetic nanowire structure, with the Au cap and compound substrate (bottom), the self-assembled iron nanowires (dark green), Cu spacer layer, Fe or Ni-Fe (Permalloy) free layer (green), the Peltier Bi layer (light green), and current return Au layer.

It is possible to develop narrow spectral width tunable microwave sources at practical power levels based on the self-phase locking property, not only between two but between many nano-contact structures. Arrays of individual nano-contact devices together can achieve high power microwave generation while retaining all the

advantages of the current tunability and the narrow spectral width of the fundamental effect. The nano-contact arrays can be realized by self-assembly as explored in this dissertation. All of the nano-contact structures can be phase locked. With this approach, it will become possible to substantially increase the generated power of these extremely narrow spectral width and current tunable microwave sources, while at the same time, achieve a considerable simplification in the fabrication technology. Fig.1.7 shows a schematic concept diagram of the full assembly for phase locked microwave generators. The self-assembled iron nanowire arrays form the core of the device. Calculations show that the array does not need to be strictly regular for functional self-phase locking. The electron current flows in from the gold top layer, is injected into the structured free magnetic layer through the nanowires, passes through the bismuth layer, and is collected in the bottom contact gold layers. It should be noted that the fixed layer shown in Fig.1.6 is missing here. The iron nanowires serve this function. Fig.1.7 shows the schematic of this dual purpose concept. The iron nanowires can simultaneously act (1) as the nano-contact to inject electrons into the underneath layers, and (2) as the medium for the spin polarization of these carriers. This dual function eliminates the need for the additional hard or fixed spin polarizing layer shown in Fig.1.6. In this novel approach, the "hard" property is provided by the shape anisotropy of the magnetic nanowires. The saturation induction $\mu_0 M_s$ of the iron (about 2 Tesla) in combination with the wire shape can provide a large shape anisotropy field H_{wire} that maintains the magnetization of the wire in the uniaxial direction. The shape anisotropy field can be large, with a $\mu_0 H_{\text{wire}}$ value of about 1 T for a large aspect ratio nanowire.

The electrons are spin polarized as part of the injection process through the soft or free layer, and the mismatch in polarization with the fixed axially magnetized nanowires produces back reflected spin polarized electrons that drive the precession in the free layer. This layer can be either iron or Permalloy (Ni-Fe), separated from the free ends of the nanowire array by the Cu spacer layer. The in-plane free magnetic layer is subject to its own shape anisotropy field H_{free}. For wide area iron films, for example, the applicable $\mu_0 H_{\text{free}}$ is equal to $\mu_0 M_s$ and is about 2 T. The dual functionality through the axial shape anisotropy for the nanowires and the in-plane shape anisotropy of the structured thin film free layer make this new design much simpler than previous structures. There is no need for a separate hard spin polarizing layer as well as large external magnetic field for device biasing. Relatively small bias fields, in combination with the built-in shape anisotropy for the structured free layer, can be used for the magnetic tuning of the oscillator. This field-shape biasing feature has been checked experimentally by Kuanr et al. in the design and development of Fe film-based band-stop microwave filters[46]. Therefore, by using axially magnetized nanowires for current injection and spin polarization three tuning modes (1) shape, (2) magnetic field, and (3) current can coexist.

1.5 Outline of the dissertation

This dissertation is divided into six chapters. The experimental methods used and the principle behind the equipment operation is discussed in Chapter 2. The growth condition and parameters are discussed in details in Chapter 3. The deposition and

growth of thin films are performed at constant temperature and the result of the growth in the reducing environment is shown. The two resulting epitaxial structures (nanowires and the oxide matrix) are studied and characterized by different methods and electron microscopy as described in Chapter 2. In Chapter 4, the growth mechanism is discussed and the thermodynamics versus kinetics of the growth of iron nanowires is presented for different growth temperatures. In addition, the growth temperature is systematically varied and the effect of the growth temperature on the size and shape evolution of the resulting ferromagnetic α-Fe nanowires is studied. Chapter 5 focuses on measuring the magnetic properties of the iron nanowires. The effect of the changes in the size and length of the ferromagnetic nanowires on saturation magnetization, the squareness of the hysteresis loops, and coercivity is studied. The preliminary results of Ferromagnetic resonance (FMR result is also presented in Chapter 5. In Chapter 6, a radically different experiment is performed. The self-assembled single crystal iron nanowires are used as the nucleation sites for growth of vertically aligned multi-walled carbon nanotubes using the plasma enhanced chemical vapor deposition method. It is shown that the changes in size and length of the iron nanowires affect the diameter and shape of the carbon nanotubes. The field emission properties of the carbon nanotubes are also studied. Chapter 6 is self-contained in that it has its own introduction, experiment, results and discussion section.

Chapter 2 Experimental Techniques

2.1 Pulsed laser deposition

Pulsed laser deposition (PLD) was the primary thin film growth technique used in this work. Theoretically and experimentally PLD is a simple thin film deposition technique. There is one rotating target holder and one substrate holder facing each other in a stainless steel vacuum chamber. A high energy laser beam (most frequently an excimer laser) is used as an external energy source to vaporize materials from the target surface. A set of optical lenses is used to focus the laser beam on the target surface. A schematic of a PLD vacuum chamber is shown in Fig. 2.1. The pulsed laser beam typically has 30 ns pulses with energy in the range of 0.01-1.2 J and at a frequency of 1-20 Hz. As a result, the vapor (plume) which contains materials dissociated from the target is ejected normal to the target surface. The plume expands away from the target with a strong forward-directed velocity distribution of the different particles. The ablated species condense on the substrate placed opposite to the target. The ablation process in the vacuum chamber takes place either in vacuum or in the presence of some background gas. In the case of oxide films, oxygen is the most common background gas.

The principle of pulsed laser deposition, in contrast to the simplicity of the system set-up, is a very complex physical phenomenon. It not only involves the physical process of the laser-material interaction on a solid target and energy transformation, but also the formation of the plasma plume with high energetic

species and the transfer of the ablated material through the plasma plume onto the heated substrate surface[47].

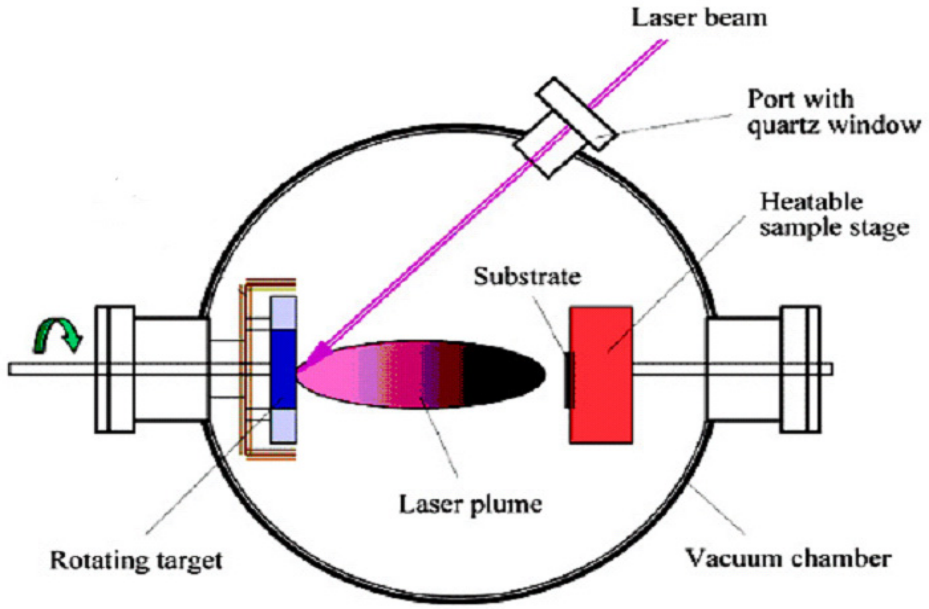

Fig.2.1 Schematic of pulsed laser deposition chamber.

Generally, the PLD process can be divided into the following four steps: 1) laser radiation interaction with the target; 2) dynamics of the ablation materials; 3) deposition of the ablation materials on the substrate; and 4) nucleation and growth of a thin film on the substrate surface. Each of the above steps is critical to the quality and characteristics of the films i.e. crystallinity, stoichiometry, uniformity, and surface roughness. During deposition different parameters including substrate temperature, laser energy density and frequency, target-to-substrate distance, base

pressure and deposition gas pressure are optimized to achieve high quality thin films. The substrate temperature is critical to the crystallinity of the films. Normally, an amorphous phase forms when the substrate temperature is below a certain value. As the substrate temperature increases films start to crystallize. For an epitaxial growth, the substrate temperature should be optimized, which varies for different materials. The energy density of the laser beam has significant effects on the uniformity of the film. Target-to-substrate distance is a parameter that governs the angular spread of the ablated materials. The oxygen partial pressure is also a very important parameter in the growth of oxide films. The chamber is normally pumped down to a base pressure of ~10^{-5} Torr before the reactive gas, such as oxygen, is introduced into the chamber.

The lasers commonly used for PLD include ArF, KrF, XeCl and XeF excimer lasers with wavelength of λ = 193, 248, 308, and 351 nm, respectively. It is generally recognized that the shorter the wavelength, the more effective the laser ablation process. The laser used in this study was a KrF laser with λ = 248 nm and pulse width of 30 ns.

The most important feature of PLD is that the stoichiometry of the target can be retained in the deposited films. This is the result of the extremely high heating rate of the target surface due to pulsed laser irradiation. Because of the very short pulse width of the laser, the evaporation of the target is negligible. When the target material is ejected towards the substrate, different components have similar deposition rates, making the film have the same composition as the target material.

Another advantage of the PLD is its versatility. With the choice of an appropriate laser almost any material can be deposited in a wide variety of gases over

a broad range of gas pressures and substrate temperatures. The targets used in PLD are small compared with the large size required for other sputtering techniques. Also it is quite easy to produce multi-layered films of different materials by sequential ablation of assorted targets held in one target holder. Also, by controlling the number of pulses, fine control of film thickness down to the atomic monolayer can be achieved. Another advantage of PLD is its cost-effectiveness. Several vacuum chambers can be arranged around a single laser source and the laser beam can be directed to each chamber using different mirrors and lenses.

There are, however, two major disadvantages associated with using PLD. One is the lack of uniformity over a large area which is due to the narrow angular distribution of the plume. The other and most important disadvantage is an intrinsic problem called "splashing" which results in deposition of micron sized particulates on top of the film surface. The occurrence of splashing has several origins such as surface boiling, expulsion of liquid by shockwave recoil, and exfoliation[1]. There are several solutions to avoid splashing which include using a high quality target, target surface improvement and smoothing, mechanical particle filter, plume manipulation, off-axis PLD and lowering laser energy density.

With respect to scaling-up due to the demand for metal-oxide based electronics or other multicomponent thin films, the commercial-scale development of PLD systems is possible. It has been reported[48] that some PLD systems can deposit thin films on 8-inch wafers with deposition rates of more than 1 micron-cm^2/s.

The films studied in the present work were deposited in a vacuum where base pressure was below 10^{-6} torr. The substrates were heated at a rate of 20 °C/min and

the growth temperature varied from 480 °C to 850 °C. The substrates were cleaned using a sequence of ultrasonic baths in trichloroethyene, acetone and isopropanol before being attached to the substrate heater. A shutter was used to cover the substrate during pre-ablation to clean the surface of the target with the laser beam without contaminating the substrate. A laser energy density of ~1.5 J/cm^2 was used, which corresponds to a growth rate of 15 nm/min. After deposition the samples were cooled down at a rate of 5 °C/min in vacuum atmosphere.

2.2. Structural characterization

2.2.1. X-Ray diffraction

X-ray diffraction was used as the first step to characterize thin film samples grown on single crystalline substrates. Hard x-rays can penetrate through the epitaxial layers and measure the properties of both the film and the substrate. An X-ray incident upon a sample will either be transmitted, in which case it will continue along its original direction, or it will be scattered by the electrons of the atoms in the material. In general, the scattered waves destructively interfere with each other, with the exception of special orientations at which Bragg's Law is satisfied.

According to Bragg's Law, X-ray diffraction can be viewed as a process that is similar to reflection from planes of atoms in the crystal. The crystal planes are illuminated at a glancing angle θ and X-rays are scattered with an angle of reflection also equal to θ. The incident and diffracted rays are in the same plane as the normal to

the crystal planes. Bragg reasoned that constructive interference would occur only when the path length difference between rays diffracting from parallel crystal planes would be an integral number of wavelengths. When the crystal planes are separated by a distance d, the path length difference would be $2d\sin\theta$ (see Fig.2.2). Thus, for constructive interference to occur the following relation must hold true:

$$n\lambda = 2d\sin\theta \qquad \text{Eq. 2.1}$$

Here, n is an integer, λ is the wavelength of X-rays (1.54056 Å for copper K_α), d is the lattice interatomic spacing and θ is the diffraction angle.

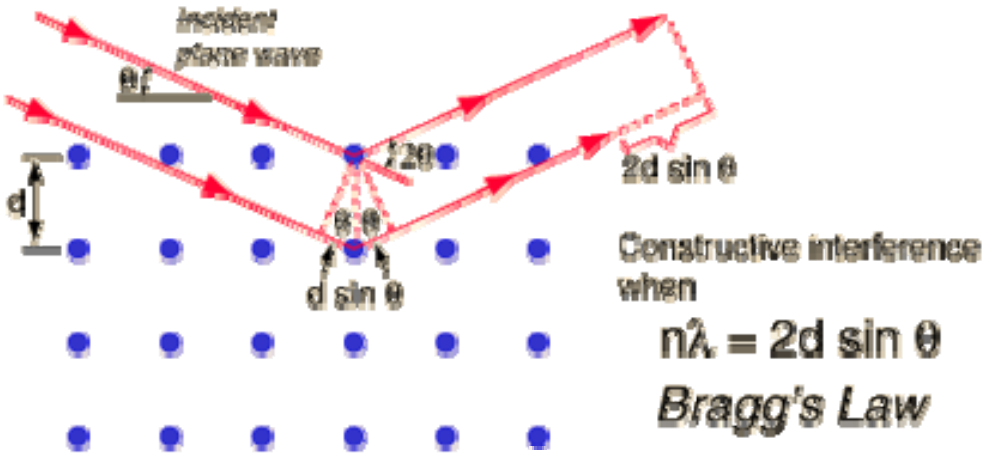

Fig.2.2 Schematic of Bragg's Law.

X-ray structural analysis can be used to determine the quality of the thin films and nanostructures. The techniques include θ-2θ scans, ϕ scans, and rocking curves.

Using θ-2θ scans it is possible to determine the crystalline orientation of the thin films. The source and detector angles are synchronized to each other, so that the Bragg condition is always satisfied for the plane parallel to the surface of the film. As the angle of the incident X-ray beam is varied, the detector will pick up the constructive interference of the reflected X-rays when an angle corresponding to the crystalline lattice spacing of any family planes in the sample is reached. A *c*-axis orientated thin film corresponds to when only one family of planes, i.e. (00*l*), satisfies the Bragg's Law condition during the θ-2θ scan. The degree of *c*-axis orientation can be determined with a rocking curve. By fixing the detector angle to the value for the (001) crystalline plane, i.e. $2\theta_{001}$, the source angle can be varied by as much as two degrees around $2\theta_{001}$. The full width at half maximum (FWHM) of the resulting peak thereby gives an indication of the degree of *c*-axis orientation of the crystal.

X-ray diffraction characterization of the films in this dissertation was conducted by using Cu K_α radiation in a Siemens D5000 four-circle diffractometer.

2.2.2 Transmission electron microscopy

Transmission electron microscopy (TEM) was an essential part of the work done in this dissertation and was used to characterize the phases, their lattice parameters, chemical composition and also to study the shape, size and morphological changes in the obtained nanostructures.

TEM was first developed in the 1930's on the basis that since electrons are smaller than atoms theoretically it would be possible to build a microscope that could image details below the atomic level. According to the famous de Broglie's equation which shows the wavelength of electrons is related to their energy:

$$\lambda \sim \frac{1.22}{E^{1/2}} \qquad \text{Eq.2.2}$$

We find that for 100 keV electrons, $\lambda \sim 0.004$ nm. The resolution of TEM is well below this due to the limitation in making perfect electron lenses. Therefore, TEM functions exactly as its optical counterpart except that it uses a focused beam of electrons instead of light to image the specimen and gain information as to its structure and composition. Instead of glass lenses, TEM focuses electron beams which are emitted from the filament and accelerated by a high voltage (100 kV – 1000 kV) with electromagnetic lenses. A strong magnetic field is generated by passing a current through a set of windings. This field acts as a convex lens, bringing off-axis rays back to focus. A condenser aperture controls the fraction of the beam that is allowed to hit the specimen. The electron beam is scattered by the specimen and the diffracted beams are brought to focus by an objective lens. The objective lens forms an inverted initial image, which is subsequently magnified. In the back focal plane of the objective lens a diffraction pattern is formed. A final TEM image or diffraction pattern can be produced on the fluorescent viewing screen by a series of objective lens, intermediate lens and projector lens.

The main TEM imaging and diffraction techniques include: 1. conventional imaging (bright-field and dark-field TEM); 2. Selected area electron diffraction (SAD); 3. Convergent-beam electron diffraction (CBED); 4. Phase-contrast imaging (high-resolution TEM, HRTEM); and 5. Z-contrast imaging. In addition to diffraction and spatial imaging, the high-energy electrons in TEM cause electronic excitations of the atoms in the specimen. Two important spectroscopic techniques make use of these excitations: i.e. energy-dispersive x-ray spectroscopy (EDS) and electron energy-loss spectroscopy (EELS). In this dissertation, the conventional bright-field and dark-field imaging, SAD, HRTEM and EDS and EELS are used to study the microstructures of the nanostructures in thin films.

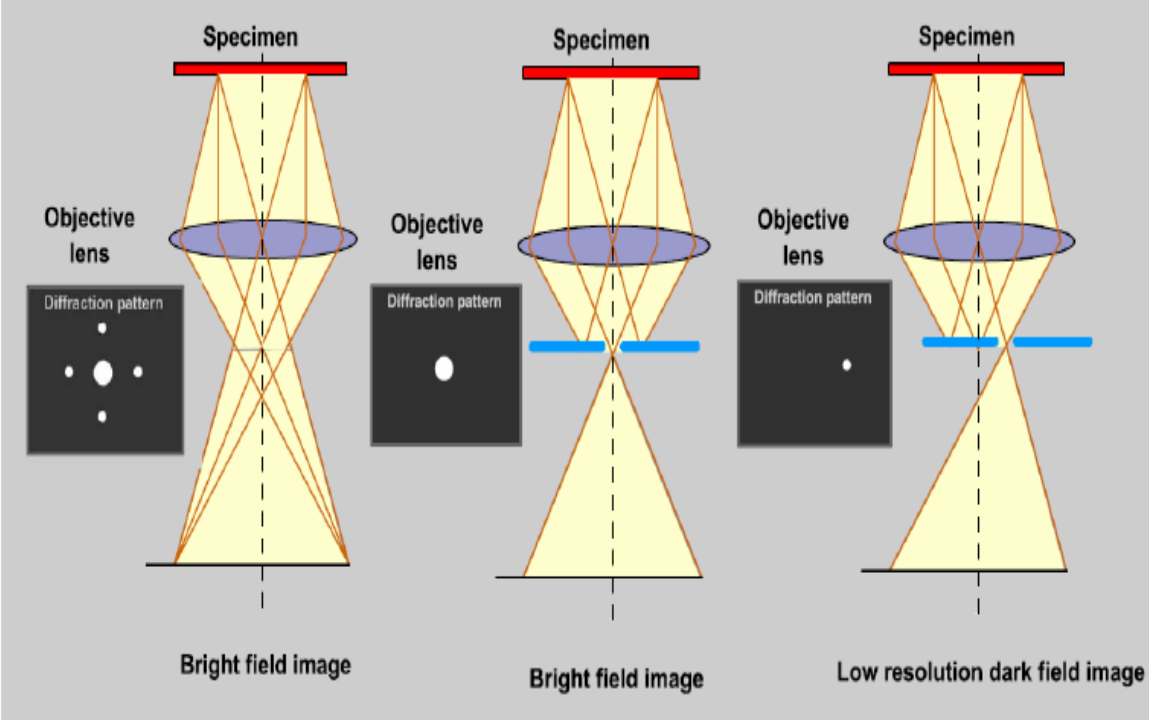

Fig.2.3 Schematic of basic operation modes of TEM imaging: diffraction mode (left), bright field (center) and dark field (right) imaging.

Fig.2.3 shows the basic operation modes in TEM. By inserting the aperture or tilting the beam, different types of images can be formed. In the diffraction mode, the image plane coincides with the back focal plane of the objective lens; while in the image mode, the image plane coincides with the image plane of the objective lens. In SAD mode, a second aperture, an "intermediate aperture" is positioned in the image plane of the objective lens, which is to confirm that the diffraction pattern is produced by a selected area of the specimen. The separation of the diffraction spots on the viewing screen can be used to determine the interplanar spacing in the crystal. The relation between (hkl) planes of a crystal and 2θ is given by the Bragg Law for diffraction:

$$n\lambda = 2d_{hkl}\sin 2\theta \qquad \text{Eq.2.3}$$

In a very similar way, the individual points of electron diffraction patterns can be indexed to (hkl) planes. Fig.2.4 shows a schematic of the geometry of a selected area diffraction pattern. Since $\theta \sim 1^{\circ}$ for low order diffractions from most materials, we can assume:

$$\sin\theta \sim \tan\theta \sim \frac{1}{2}\tan(2\theta) = \frac{R}{L} \qquad \text{Eq.2.4}$$

Then the relation between the distance a given diffraction spot is from the transmitted beam and the (hkl) plane giving rise to that spot is given by

$$\lambda L = Rd_{hkl} \qquad \text{Eq.2.5}$$

where λ is the wavelength of the electron probe, L is the camera length, R is the distance of the spot from the transmitted beam and d_{hkl} is the interplanar spacing of the diffracting (hkl) plane.

Taken as a product, λL is referred to as the camera constant of the TEM. The camera constant will change with different accelerating voltage and camera length (L). So, using this equation, individual spots on the diffraction pattern can be assigned to (hkl) planes.

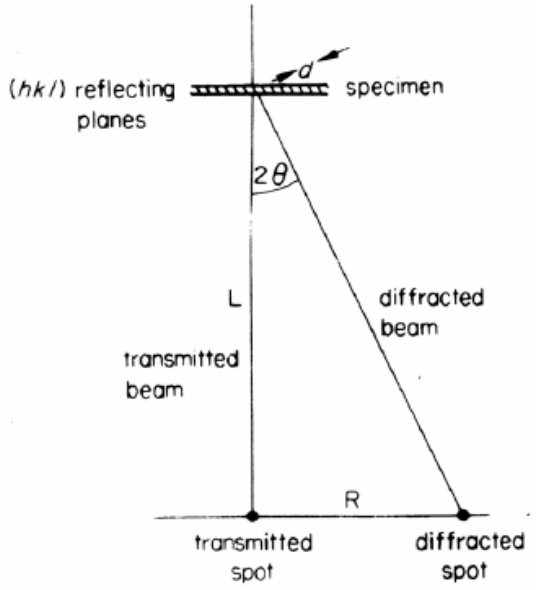

Fig.2.4 Geometry demonstration for electron diffraction in Transmission Electron Microscopy.

In the simple imaging mode, the specimen shows little contrast. To increase the contrast objective apertures are inserted at the back focal plane of the objective lens in

the conventional imaging mode, which is called diffraction contrast. When the aperture is positioned to allow only the transmitted electrons to pass, a bright-field (BF) image is formed, illustrated in the center part of Fig.2.3. When the aperture is positioned to allow only some diffracted electrons to pass, a dark-field (DF) image is formed, shown in the left part of Fig.2.3.

Conventional bright-field and dark-field images cannot be used to study the local structure, interfaces and defects in the nanostructures. Therefore, high resolution TEM (HRTEM) is needed for this purpose. The HRTEM image is obtained when two or more diffracted beams are included in the objective aperture for the image formation and the crystal structure can be determined by applying Fourier transform principles (Fig.2.5). Imaging of the crystal structure therefore becomes a special case of phase-contrast image formation[49,50]. The wave function $\varphi_{ex}(r)$ of electrons at the exit face of the object can be considered as a planar source of spherical waves and the amplitude of a diffracted wave in the direction given by the reciprocal vector g can be expressed by the Fourier transformation of the object function, therefore

$$\varphi(g) = I_g \Psi(r) \qquad \text{Eq.2.6}$$

The intensity distribution in the diffraction pattern is given by $\varphi(g)^2$ in the back focal plane of the objective lens. The second stage of the imaging is described by an inverse Fourier transform which reconstructs an enlarged object function $\varphi(R)$ and the intensity in the image plane is given by $\varphi(R)^2$. Here the electron beam undergoes a phase shift $\chi(R)$ with respect to the central beam. The phase shift is due to the spherical aberration, defocus and incoherent damping function $D(\alpha, \Delta, g)$ (α is the convergent angle of the incident electron beam and Δ is the half-width of the defocus

spread ε due to chromatic aberration) so that the wave function $\varphi_{im}(R)$ at the image plane is given by

$$\varphi_{im}(R) = \Gamma^{1} T(g)\ \varphi(g) \qquad \text{Eq.2.7}$$

Here, $T(g)$ is the contrast transfer function of the object and is described as:

$$T(g) = D(\alpha, \Delta, g)exp[i\chi(g)] \qquad \text{Eq.2.8}$$

where

$$\chi(g) = \pi\varepsilon\lambda g^{2} + \pi C_s\lambda^{3}g^{4}/2 \qquad \text{Eq.2.9}$$

It can be seen from the above equations that phase contrast depends on many parameters, such as the defocus value ε, spherical aberration of the objective lens C_s and sample thickness. Interpretations of high-resolution images involve image simulation, making models of the structure of the specimen, taking into account the constants of the microscope and the conditions used to take the HRTEM image, and fitting these models to the experimental image.

One of the main drawbacks of the TEM is the specimen preparation. The requirement for a thin specimen is a major limitation of the TEM. Since electrons scatter very strongly by the atomic electronic potential of the sample, extremely thin samples (< 1 μm) are required for TEM characterization. Both cross-section and plan-view specimens were prepared for TEM observation in this dissertation. For a cross section sample, the transmitted electron beam is perpendicular to the film growth direction, while for a plan view sample the transmitted electron beam is parallel to the film growth direction. A tripod polishing method[51] was used for the preparation of both cross-section and plan-view samples.

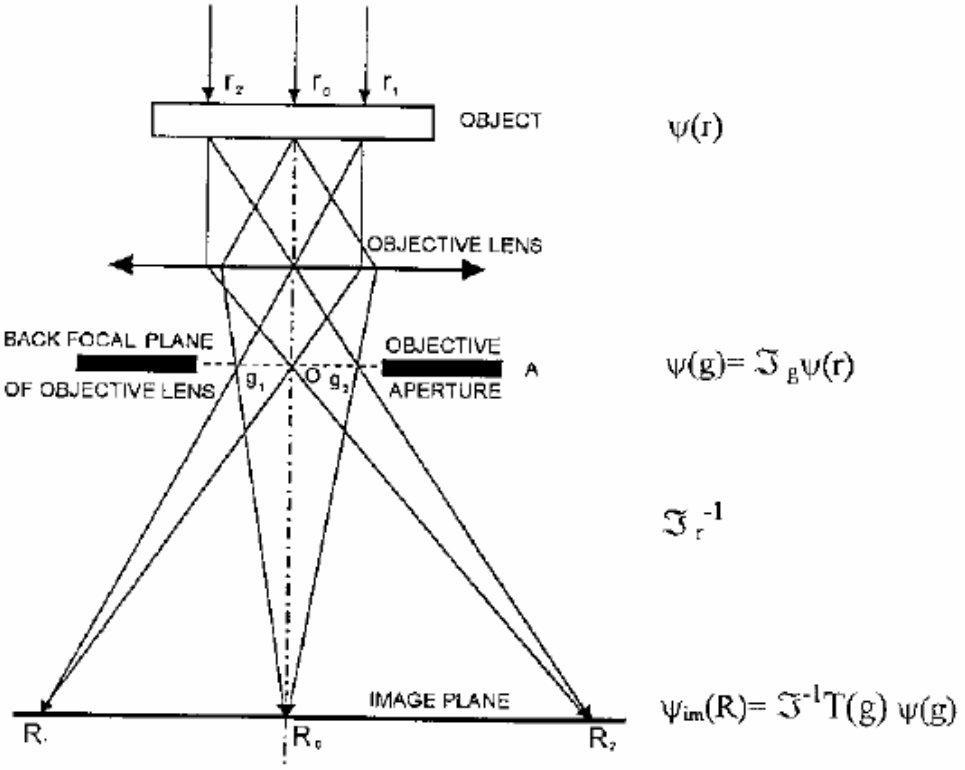

Fig.2.5 The image formation in HRTEM imaging and determination of crystal structure by Fourier transform principles.

The cross-sectional TEM specimen preparation involves several steps. The first step is to cut off two pieces of the sample. The two pieces of sample are then glued together using M-bond 610 adhesive with the film sides facing each other. Subsequently, the glued sample is mounted on a tripod polisher holder with acetone dissolvable wax. The glued sample is mechanically thinned from both sides across the glued interface using diamond lapping paper. The mechanical polishing includes

polishing using 30, 9, 3 and 1 μm diamond lapping paper sequentially and final fine polishing using 0.05 μm silica suspensions on texture. If the sample is not electron transparent after mechanical polishing it is ion-milled for a short time (20-40 min). The tripod polishing method takes advantage of the angle polishing concept to monitor the sample thickness. Initially, a larger angle (~ 5°) is used until an edge appears at the sample. Then, the polishing angle is changed to a smaller angle (~ 1°) for fine polishing. Thus, a shadowed area is created in front of the sample. The sample is polished until the shadow area disappears. Thus, the specimen prepared by the tripod polisher is in a wedge shape with one extremely thin edge (less than 1 μm, ideally). However, the whole sample is still thick enough to avoid mechanical damages. The sample is detached from the holder by dipping the sample into acetone and then glued on a slotted copper grid with the thinner edge at the center of the slot. The supporting copper grid can also be used to assist monitoring the sample thickness. The specimen can be glued on the copper grid holder at the final polishing step. Because of the wedge polishing, one side of the sample is thinner than the other side. When the copper grid is polished it changes color. The sample edge close to the changed color side of the copper grid will be very thin. The process of sample thinning can take more than a day.

The other drawbacks of TEM include observation being limited to a small area of the sample, electron beam damage to the sample and also the fact that the information obtained from TEM is averaged through the thickness of the specimen-a single TEM image has no depth sensitivity.

2.3 Magnetic measurements

2.3.1 Mössbauer spectroscopy

Mössbauer spectroscopy was used to identify the ferromagnetic phases in this work. Mössbauer spectroscopy is a spectroscopic technique based on the Mössbauer effect. This effect is a physical phenomenon which refers to the resonant and recoil-free emission and absorption of gamma rays by atoms bound in a solid form. In its most common form, Mössbauer Absorption Spectroscopy, a solid sample is exposed to a beam of gamma radiation, and a detector measures the intensity of the beam that is transmitted through the sample. The gamma-ray energy is varied by accelerating the gamma-ray source through a range of velocities with a linear motor. The relative motion between the source and sample results in an energy shift due to the Doppler effect (change in the apparent frequency of a wave as observer and source move toward or away from each other). In the resulting spectra, gamma-ray intensity is plotted as a function of the source velocity. At velocities corresponding to the resonant energy levels of the sample, some of the gamma-rays are absorbed, resulting in a drop in the measured intensity and a corresponding dip in the spectrum. The number, positions, and intensities of the peaks provide information about the chemical environment of the absorbing nuclei and can be used to characterize the sample. In order for Mössbauer absorption of gamma-rays to occur, the gamma-ray must be of the appropriate energy for the nuclear transitions of the atoms being probed. Also, the gamma-ray energy should be relatively low; otherwise the system will have a low recoil-free fraction resulting in a poor signal-to-noise ratio. Only a

handful of elemental isotopes exist for which these criteria are met, so Mössbauer spectroscopy can only be applied to a relatively small group of atoms including: ^{57}Co, ^{57}Fe, ^{129}I, ^{119}Sn, and ^{121}Sb. Of these, ^{57}Fe is by far the most common element studied using the technique.

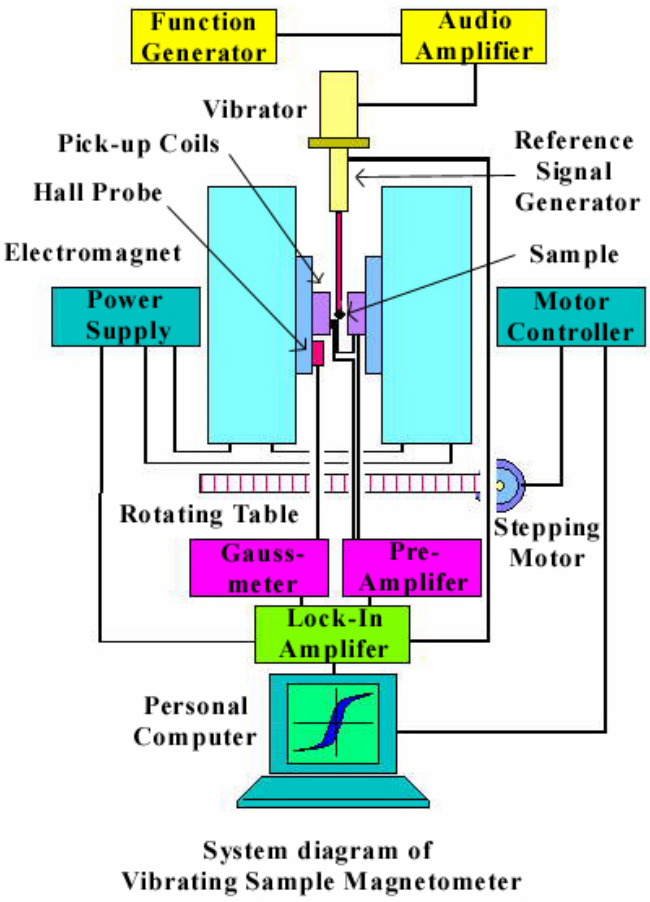

System diagram of Vibrating Sample Magnetometer

Fig.2.6 Schematic of Vibrating Sample Magnetometer

In our experiments conversion electron Mössbauer (CEM) spectra of the samples were observed by detecting resonantly re-emitted electrons with a gas-flow counter

coupled to a Mössbauer spectrometer with a ^{57}Co(Rh) source. The spectra was then computer-fitted assuming a Lorentzian line shape.

2.3.2 Vibrating sample magnetometer

The vibrating sample magnetometer (VSM) was the mostly used for measurements of the magnetic properties of the samples. VSM is a basic instrument for characterization of magnetic materials which was developed in 1956 by S. Foner and Van Oosterhart. The principal behind the measurement is simple: it uses an electromagnet which provides a DC magnetizing field. When a material is placed within a uniform magnetic field a vibrator mechanism vibrates the sample in the magnetic field. This causes the sample to undergo sinusoidal motion and creates a change in the magnetic flux, which is detected by pickup coils as an induction voltage. The flux change is proportional to the magnetic moment in the sample:

$$V(t)=Cd(\varphi)/dt \qquad \text{Eq.2.10}$$

where $\varphi(t)$ represents the change in flux in the pick-up coils caused by the moving magnetic sample. The output measurement displays the magnetic moment M as a function of the field H. A schematic of the VSM system is shown in Fig. 2.6.[52]

VSM provides a fast and easy technique for the measurement of the magnetic properties of a material. The sensitivity of VSM manufactured by Lake Shore is in the range of 10^{-4} emu which is sufficiently accurate for the samples used in this dissertation.

2.3.3 Superconducting quantum interference device magnetometer

To measure the hysteresis loop more accurately and at lower temperatures, a Superconducting quantum interference device (SQUID) magnetometer was used. SQUIDs are very sensitive detectors of magnetic flux. They combine the physical phenomena of flux quantization and Josephson tunneling.

A Josephson junction consists of two weakly coupled superconducting electrodes which are separated by a thin insulating barrier. If superconductors separated by a thin insulating layer are brought very close to each other, tunneling of electrons can occur. If the distance is reduced even more, tunneling of Cooper-pairs will also occur. For currents below a critical value, the pair tunneling constitutes a supercurrent, and no voltage is developed across the junction; however a voltage appears for currents greater than the critical value. The presence of the insulating layer typically restricts the value of the supercurrent flowing in the coil to less than 10^{-5} A. Most low-T_c SQUIDs are made from Niobium thin films which have a transition temperature of around 9.25 K, well above the boiling temperature of liquid helium and are also mechanically very stable. Tunnel junctions are patterned from $Nb/AlO_x/Nb$ trilayers in which a AlO_x barrier is formed by oxidization of a few nanometers of aluminum[53]. Fig. 2.7 shows a schematic of a Josephone junction[54].

There are two types of SQUIDs. The first, DC SQUID, consists of two Josephson junctions connected in parallel on a superconducting loop and is operated in the voltage state with a current bias. The second kind, RF SQUID, consists of a single Josephson junction inserted into a superconducting loop. The sample is placed in a superconducting pick-up coil that is connected to the actual SQUID. Since the

magnetic flux through a superconducting ring is quantized to $f = nf_0$ with $f_0 = h/(2|e|)$ where n is an integer, h is Planck's constant and e is electron charge, the sample will induce a supercurrent in the pick-up coils that will keep the flux at a constant value.

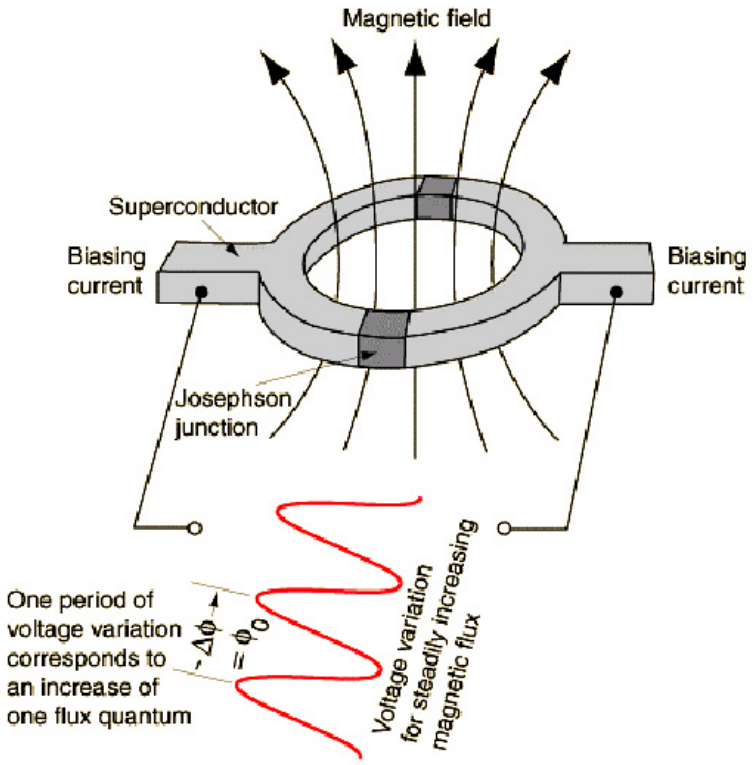

Fig.2.7 Schematic of a Josephson junction consisting of two superconductors separated by thin insulating layers.

Through this supercurrent the flux originating from the sample is transported from the pick-up coil to the SQUID. A schematic of a SQIUD is shown in Fig.2.8. A sensitivity of 10^{-7} emu is claimed by Quantum Design (the manufacturer) but

sensitivity of 10^{-6} emu is typically seen in practice. The temperature can be varied between T = 1.7 K and 400 K.

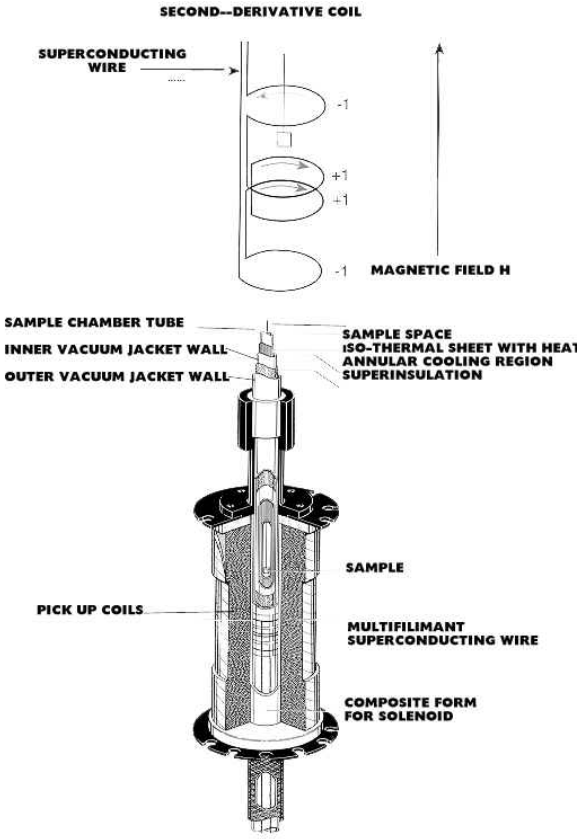

Fig.2.8 Schematic of SQUID system.

2.3.4 Magnetic force microscopy

Magnetic force microscopy (MFM) was used to image the magnetic field gradient and its distribution above the samples surface. The MFM technique is a derivation of Atomic force microscopy (AFM) and measures the change of the interaction force

between a magnetized probe and the local stray magnetic field from the sample, point by point, as the probe is scanned across the surface. The magnetic probe is standard silicon cantilever (or silicon nitride cantilever) coated with a ferromagnetic thin film (Co-Cr). The tip is mounted on a small cantilever which transfers the force into a deflection which can be measured. In MFM, tip-sample interaction is in tapping mode. In this mode the cantilever is oscillated at its resonant frequency (often hundreds of kilohertz) and positioned above the surface so that it only taps the surface for a very small fraction of its oscillation period. The magnetic forces between the tip and the sample are measured by monitoring the cantilever deflection while the probe is scanned at a constant height above the surface. A map of the forces shows the natural or applied magnetic domain structure of the sample.

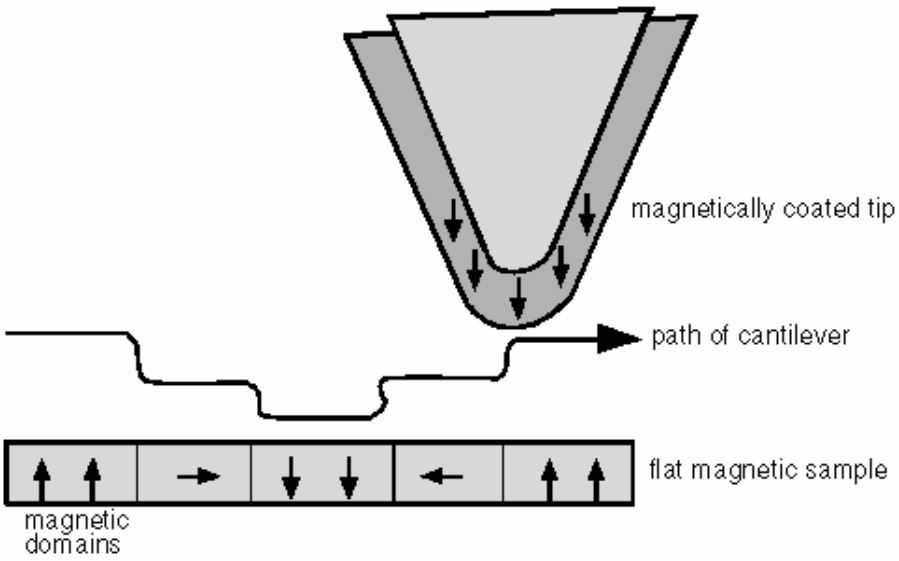

Fig.2.9 Schematic of how MFM maps the magnetic domains of the sample surface**.**

The image taken with a magnetic tip contains information about both the surface structure (topography) and the local magnetic field of a surface. Which effect dominates depends upon the distance of the tip from the surface. Signals from surface topography dominate at close distances to the surface while, at greater distances from the surface (typically beyond 100 nm), the magnetic signal dominates. Consequently, depending on the distance between the surface and the tip, normal MFM images may contain a combination of topography and magnetic signals. Fig.2.9 shows a schematic of how MFM maps the magnetic domains of the sample surface**.** Little sample preparation is required for MFM and a lateral resolution of below 50 nm can be achieved. This makes MFM a powerful method for investigation of magnetism in nanostructures.

Chapter 3 Self-Assembly of Ferromagnetic Iron Nanowires

3.1 Pulsed laser deposition of $La_{0.5}Sr_{0.5}FeO_3$

A single-phase $La_{0.5}Sr_{0.5}FeO_3$ target was used to deposit and grow thin films on single crystalline $SrTiO_3$ (001) substrates by pulsed laser deposition. The laser used was a KrF excimer laser (λ = 248 nm). Two different deposition parameters were chosen and compared to each other. In the first condition, the thin films were deposited in oxygen pressure of P = 200 mTorr and then cooled in atmosphere O_2 pressure. In the second sets of experiments the thin films were deposited and cooled at vacuum atmosphere ($P = 5\times10^{-6}$ Torr). The effect of growth in the vacuum and an oxygen deficient atmosphere on the structure and properties of the deposited thin films was studied. The laser energy density was around 1.4 J/cm^2, and the film growth rate was ~1.5 Å/sec. The temperature of the deposition was systematically varied from T = 560 to 840 ºC. This chapter focuses on the growth of thin films at a constant temperature of T = 760 ºC and later chapters describe the effect of varying the growth temperature on both the structure and properties of the thin films.

3.2 Structure and properties of thin films

3.2.1 X-ray diffraction results

The growth of epitaxial films of multicomponent perovskites such as $La_{0.5}Sr_{0.5}FeO_3$ by PLD is typically carried out under a relatively high oxygen background pressure of

100-200 mTorr. By choosing a lattice matched substrate and proper deposition parameters, epitaxial single-phase thin films can be obtained. Therefore, as expected, growth of $La_{0.5}Sr_{0.5}FeO_3$ in 200 mTorr of O_2 at a substrate temperature of T = 760 ºC yields single-phase epitaxial films with the perovskite structure as shown by the blue curve in the x-ray diffraction results in Fig.3.1. X-ray diffraction of the films grown in a vacuum environment ($P = 5\times10^{-6}$ Torr), however, displays peaks that cannot be assigned to $La_{0.5}Sr_{0.5}FeO_3$ (green curve in Fig.3.1).

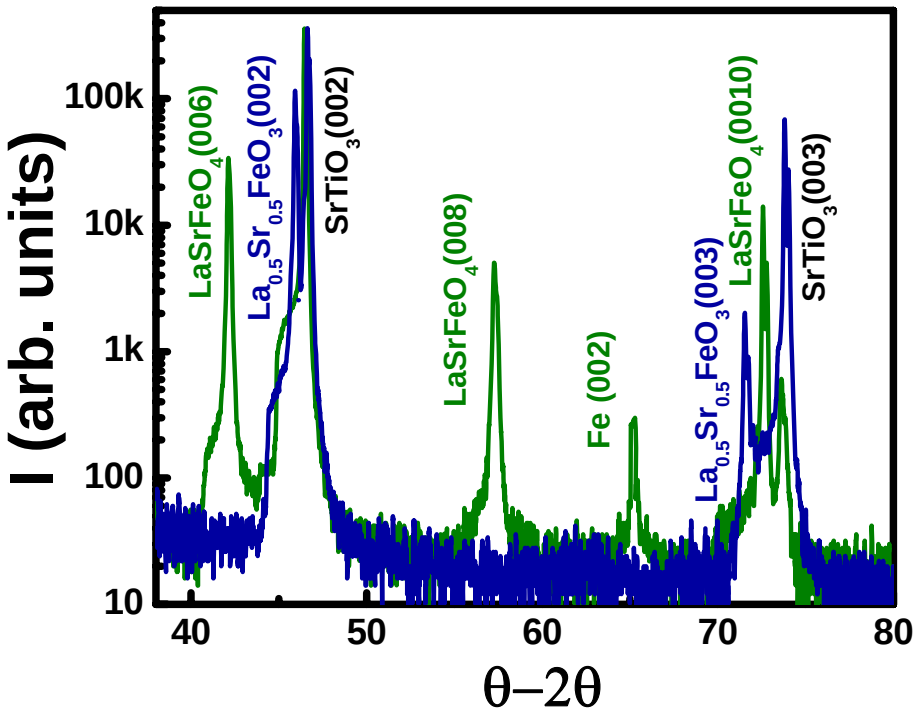

Fig.3.1 X-ray θ-2θ scan showing (00*l*) families of peaks, which can be assigned to α-Fe, $LaSrFeO_4$, and the $SrTiO_3$ substrate.

These peaks can be labeled as (00*l*) perovskite substrate $SrTiO_3$ (a = 0.3905 nm), (00*l*) $LaSrFeO_4$ ($a = b$ = 0.388 nm, and c = 1.276 nm) with K_2NiF_4 structure and (00*l*) b.c.c. α-Fe (a = 0.287 nm). This result shows that in the absence of oxygen the $La_{0.5}Sr_{0.5}FeO_3$ target phase does not grow homogeneously as a single phase film, but spontaneously decomposes into a two-phase state that consists of $LaSrFeO_4$ and α-Fe.

3.2.2 Transmission electron microscopy results

To study the structure and composition of the thin films transmission electron microscopy was performed on the sample deposited in vacuum. Fig.3.2 A shows a low magnification plan-view TEM image from a sample deposited at T = 760 ºC in vacuum atmosphere. The image clearly demonstrates that the structure is not that of single phase perovskite thin film. It is apparent that $La_{0.5}Sr_{0.5}FeO_3$ has spontaneously decomposed into a fairly uniformly distributed second phase embedded in a matrix. The corresponding electron diffraction pattern from the sample (Fig.3.2 B) displays the epitaxial relationship between the matrix and the second phase and also indicates that only two phases exist. It also reveals that the matrix phase is $LaSrFeO_4$ and therefore the second phase embedded in the matrix is α-iron.

To study the cross-sectional structure of the second phase and the matrix, a low magnification dark field TEM cross-section image was obtained along the [100] zone axis. The result is shown in Fig.3.2 C. It reveals that the iron second phase shown in Fig.3.2 A is comprised of nanowires which grow from the top of the

substrate and span through the whole thickness of the thin film. The average diameter of the nanowires is around d = 16 nm for these films grown at T = 760 °C.

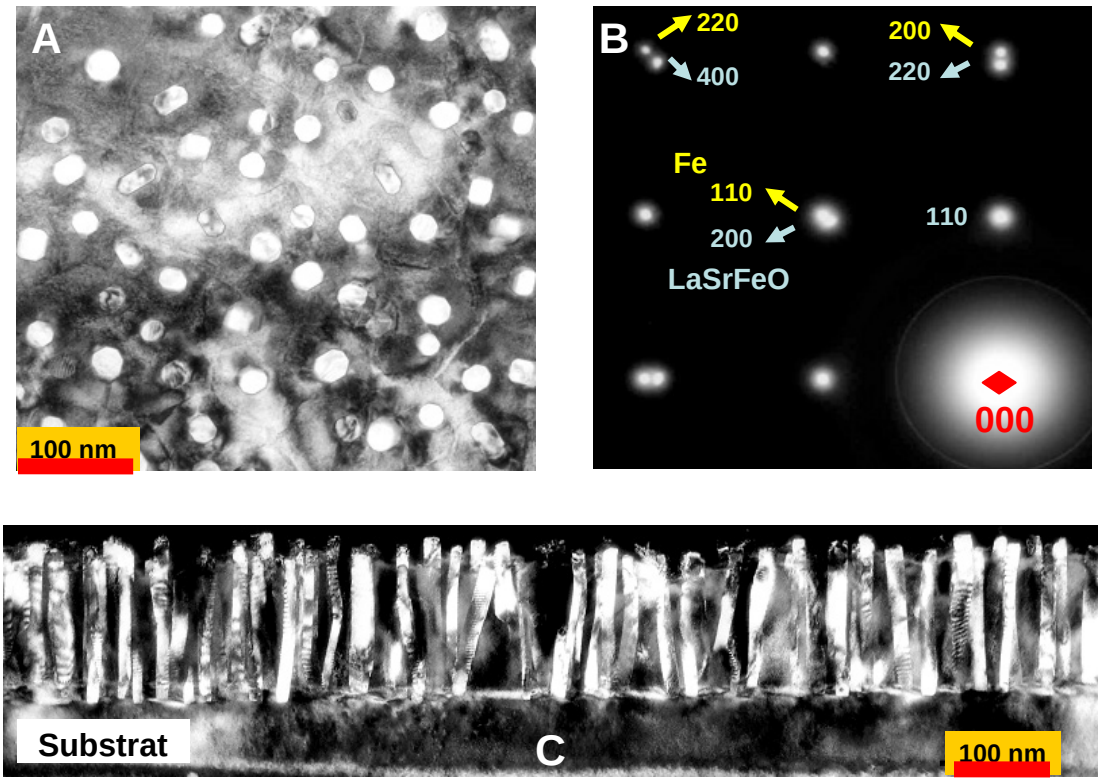

Fig.3.2 TEM results of self-assembled nanostructures. A. Plan-view TEM image from a film deposited in vacuum at T = 760 °C, showing the decomposition of the perovskite target into a second phase embedded in a matrix; B. Electron diffraction pattern illustrating the in-plane heteroepitaxy between $LaSrFeO_4$ and α-Fe; C. [001] dark field cross-section image of a film showing α-Fe nanowires embedded in $LaSrFeO_4$ matrix.

Analysis of the XRD peaks and electron diffraction patterns yields the lattice parameters of the two phases as: nanowires $a = b = c = 0.2864$ nm and matrix $a = b = 0.3873$ nm, $c = 1.2776$ nm (± 0.0005 nm for all parameters). These lattice parameters are very close to bulk values of α-Fe with a body centered cubic structure ($a = 0.287$ nm), and $LaSrFeO_4$ ($a = b = 0.388$ nm, and $c = 1.276$ nm; K_2NiF_4 structure).

Fig.3.3 A shows a (001) high resolution TEM cross-section image of a single nanowire embedded in the matrix. Fig.3.3 B is an enlargement of the region marked by the green rectangle in Fig.3.3 A. These images together with the diffraction pattern shown in the inset of Figure 3.3 B bring out the single crystal character of a typical nanowire along its entire length and the epitaxy between the matrix and nanowire both out-of-plane as well as in-plane.

The in-plane epitaxial relation of the two phases is obtained from plan-view electron diffraction (Fig.3.2 B):

$$[110]_{\alpha\text{-Fe}} \parallel [100]_{LaSrFeO_4} \text{ and } [100]_{\alpha\text{-Fe}} \parallel [110]_{LaSrFeO_4}$$

This indicates that the α-Fe is rotated 45° in-plane with respect to the $LaSrFeO_4$ matrix.

All the results suggest that the phase decomposition during deposition results in two essentially pure phases. This phase decomposition route is different from other reported epitaxial nanocomposites[33,55,54,55,56,57], in the present method a single-phase target is used and because of phase decomposition, the target phase is not one of the two phases present in the epitaxial nanocomposite.

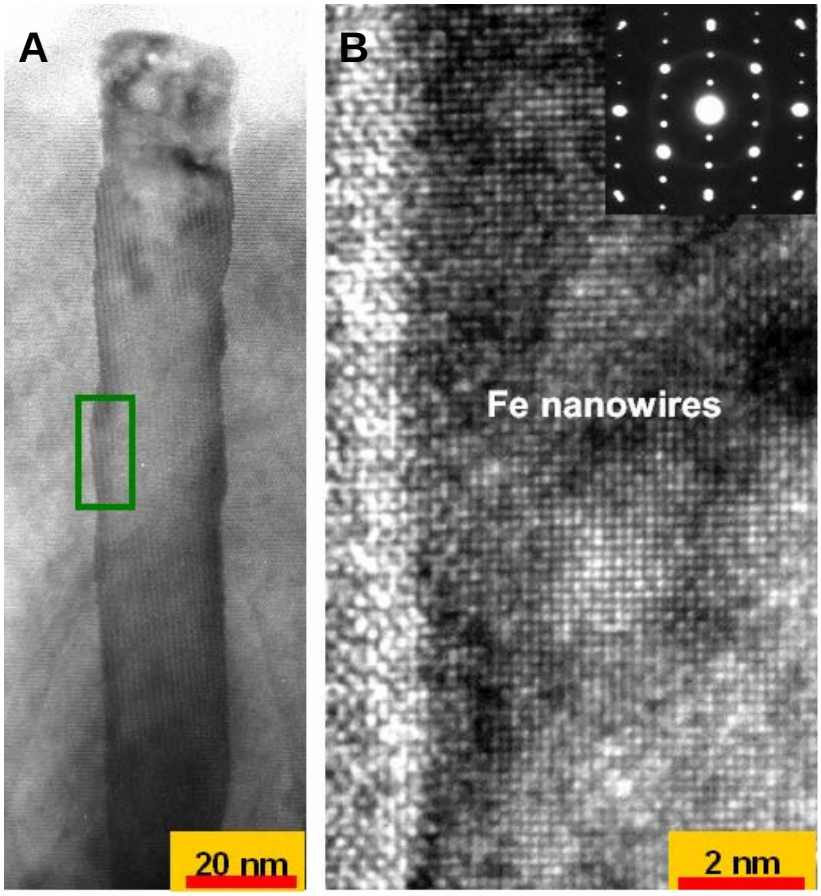

Fig.3.3 High resolution cross-section images of a single α-Fe nanowire; A. A single nanowire embedded in $LaSrFeO_4$ matrix; B. An enlargement of the region within the rectangle in A, which shows the single crystalline nature of the nanowires .The inset shows the diffraction pattern of the area in A indicating the epitaxial relationship between α-Fe nanowires with matrix.

3.2.3 Energy dispersive X-ray spectroscopy results

The lattice parameter of b.c.c iron (a = 0.2867 nm) and spinel Fe_3O_4 (a = 0.8397 nm) are such that $d_{Fe\ 110} \approx d_{Fe_3O_4\ 400}$ and $d_{Fe\ 200} \approx d_{Fe_3O_4\ 440}$. Based on XRD and electron diffraction patterns alone, it is also possible to interpret the second phase as Fe_3O_4.

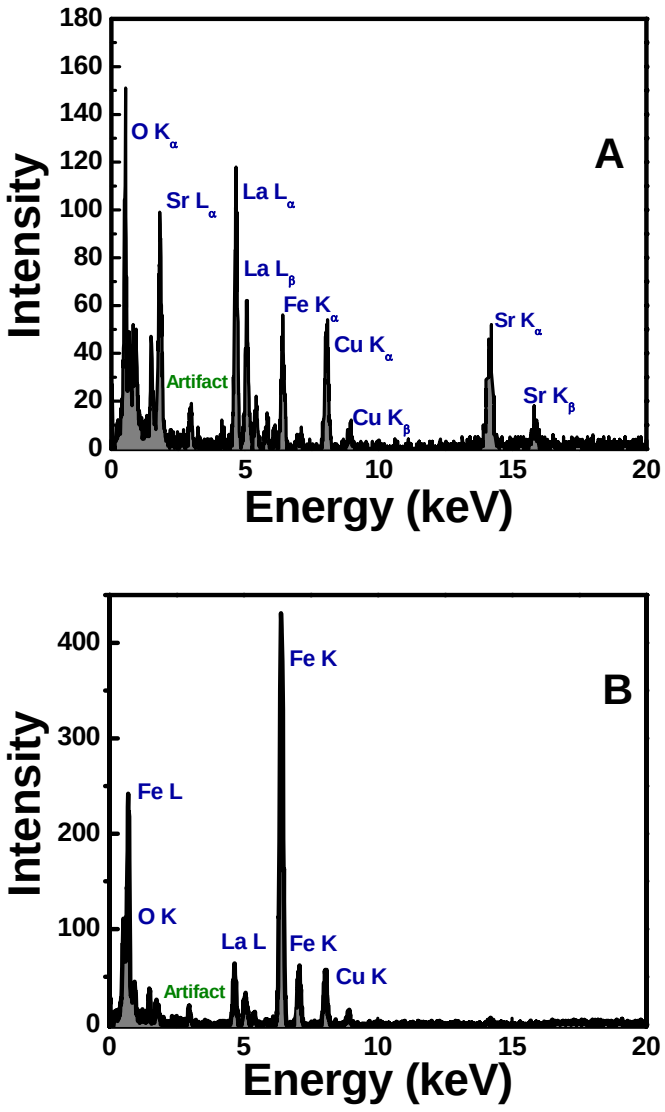

Fig.3.4 EDXS spectrum from A. $LaSrFeO_4$ matrix and B. a single iron nanopillar.

Therefore, a more detailed experiment was carried out to confirm the composition of the nanowires. Nanoprobe energy-dispersive X-ray spectroscopy (EDXS) analysis of the nanowires, shown in Fig.3.4, indicated that the main composing component of the nanowires was Fe. A small amount of oxygen was present in the spectrum. The observation of a small amount of oxygen could possibly be due to the beam spreading as a small peak was also observed for Lanthanum. The composition of the $LaSrFeO_4$ matrix is confirmed by EDXS analysis. It reveals that the Lanthanum-to-Strontium ratio in the matrix is close to 1, and overall a slight excess of Lanthanum observed.

3.2.4 Mössbauer spectroscopy results

Conversion electron Mössbauer spectroscopy (CEMS) was used to precisely identify the composition of the second phase. Fig.3.5 shows the CEMS spectrum, recorded at room temperature, for the sample grown at T = 760 °C. The spectrum can be fitted with a quadrupole split doublet (area = 47%) and a ferromagnetic sextet (area = 53%). The hyperfine parameters for the ferromagnetic sextet (Isomer Shift (IS) = 0.00 mm/s, Internal Magnetic Field = 32.9 Tesla) match perfectly with those of ferromagnetic α-Fe.

The paramagnetic doublet with quadrupole splitting of QS = 1.40 mm/s and isomer shift of IS = 0.36 mm/s is attributed to the $LaSrFeO_4$ matrix phase. A sextet in the Mössbauer spectrum is expected for the antiferromagnetic $LaSrFeO_4$; however, the observation of a doublet indicates a paramagnetic state in the matrix.

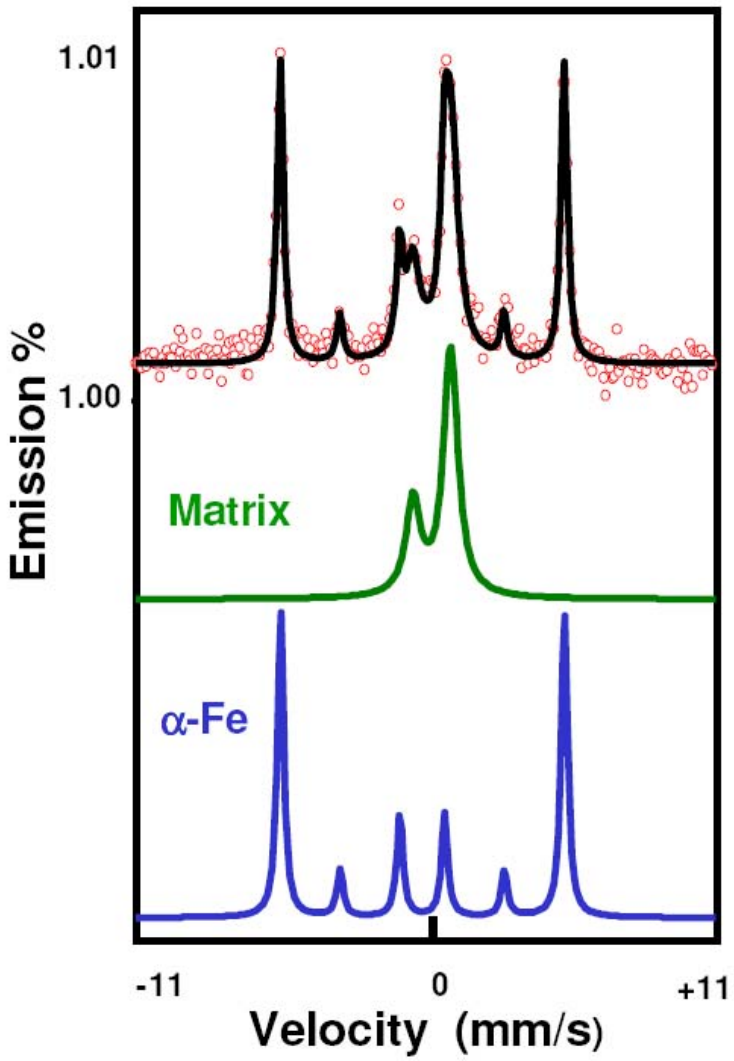

Fig.3.5 Room-temperature ^{57}Co conversion electron Mössbauer spectrum (CEMS) of the film deposited in vacuum (experimental points and the fit (black solid line)). The spectrum is composed of a superposition of two sub-spectra: the sextet of ferromagnetic α-Fe (blue) and the paramagnetic doublet of the non-stoichiometric $LaSrFeO_4$ matrix (green).

It has been shown that a slight change in La:Sr stoichiometry alters the magnetic and electronic properties of bulk $LaSrFeO_4$ [60 - 62]. In doped $La_{1-x}Sr_{1+x}FeO_4$ the Neel temperature decreases with x and therefore the oxide becomes paramagnetic at room temperature. The reason for this change in magnetic properties is believed to be due to the fact that doping disturbs the antiferromagnetic ordering of iron spins without any observable structural change. Similar behaviour is also observed in the $(La,Sr)_2CuO_4$ and $(La,Sr)_2NiO_4$ systems[63,64].

The asymmetry of the paramagnetic doublet and the degree of asymmetry relate to the specific angle between the electric field gradient (EFG) and the gamma ray beam entering the sample, and is observed in most of the crystalline specimens. The paramagnetic doublet has symmetric nature in the case of powder samples, polycrystalline or multi-oriented domain structures. The crystallinity of the matrix phase in the vacuum deposited thin films and the particular measurement geometry is the reason for the specific degree of asymmetry observed.

3.3 Properties of nanowires and the matrix

3.3.1 Properties of α-Fe

Iron with atomic number of 26 is one of the transition elements in the periodic table. Pure iron has a hardness that ranges from $H = 4 - 5$. It is soft, malleable, and ductile. Pure iron melts at about $T = 1538$ °C (2800 °F), boils at $T = 2861$ °C (5182 °F), and has a density of $\rho = 7.85$ g/cm^3. The atomic weight of iron is $W = 55.845$ g.

The metal exists in three different forms: α-iron; γ-iron; and δ-iron. The arrangement of the atoms in the crystal lattice changes in the transition from one form to another. The transition from α-iron with b.c.c. structure to γ-iron with f.c.c. structure occurs at about 910 °C (1700 °F), and the transition from γ-iron to δ-iron with b.c.c. structure happens at about 1400 °C (2600 °F).

With regards to magnetic properties, α-Fe is ferromagnetic and is easily magnetized at room temperature; it is difficult to magnetize when heated, and at its Curie temperature of $T_C \approx 770$ °C (about 1418 °F) the magnetic property disappears. The magnetization of bulk α-iron is around $M \approx 1710$ emu/cm^3. In b.c.c. α-Fe magnetocrystalline anisotropy which is the preferential alignment of atomic magnetic moments along certain, easy crystal directions, favors cube edges <100> with positive magnetic anisotropy constant (K_1). The magnetostriction constants λ_{100} and λ_{111} values for iron are 20.7×10^{-6} and -21.2×10^{-6}, respectively. The relatively small values of magnetostriction coefficients indicate that magnetization will not be largely affected by strain.

3.3.2 Properties of $LaSrFeO_4$ matrix

The structure of $LaSrFeO_4$ is known as a K_2NiF_4– type structure and can be described as a sequence of layers of tetragonally distorted NiF_6 octahedra alternating with K^+ ions located in a nine coordinated site. In other words, the K_2NiF_4 structure is a

perovskite plus half rocksalt structure combined. The separation between the layers is almost twice the intra-planar distance between the two Ni^{2+} nearest neighbours. As a result the inter-planar interactions between magnetic ions are extremely weak, so that the magnetic compounds of this type can generally be expected to have a two-dimensional behaviour[65]. The lattice structure of $LaSrFeO_4$ is shown in Fig.3.6.

The discovery of high-T_c superconductivity in hole-doped cooperate systems stimulated a renewed interest in 3d transition metal-oxides. The electronic structure and the physical properties of K_2NiFe_4–type cuperates and nickelates was intensively investigated because of the high superconducting transition temperature specifically in cuperates. The striking results in $(La, Sr)_2CuO_4$ indicated that the positive holes introduced by the substitution of La with Sr occupy newly formed in-gap states, which have mainly O 2p character. Therefore, insulating oxides of these heavy 3d transition metals are not Mott-Hubbard insulators but are charge-transfer insulators in which the energy band gap in primarily generated between occupied O 2p and unoccupied transition metal 3d levels.

In this group, $LaSrFeO_4$ is a known antiferromagnetic oxide with a Neel temperature T_N = 380 K[66]. As mentioned before, upon the hole doping in $La_{1-x}Sr_{1+x}FeO_4$ the Neel temperature decreases with x. It is believed that holes disturb and reduce the Fe^{+3}-O-Fe^{+3} superexchange interactions without causing any observable structural change in the oxide.

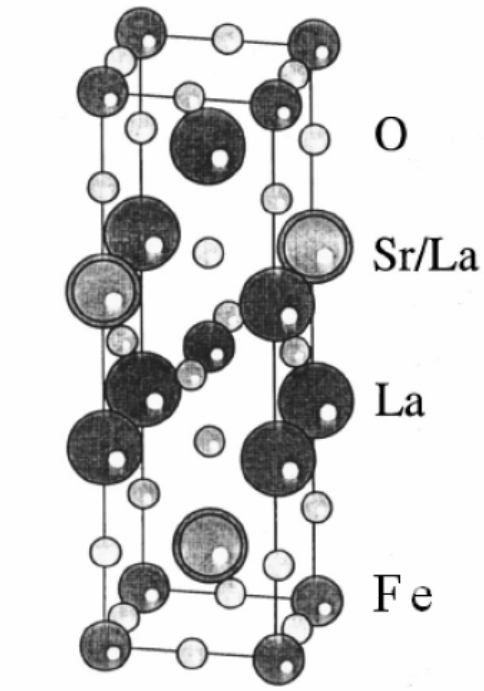

Fig.3.6 The crystal structure of $LaSrFeO_4$ matrix phase.

The important observation in $LaSrFeO_4$ oxide is the fact that it remains semiconducting even after heavy-hole doping. The changes in electronic structure of $LaSrFeO_4$ upon hole doping are quite different from those of charge-transfer insulators such as La_2CuO_4 and La_2NiO_4. As mentioned above in the case of La_2CuO_4, the gap is filled by the new in-gap states formed by the hole doping. In these oxides the in-gap state overlaps with the valence band. On the other hand, in the case of $LaSrFeO_4$, the new hole band is formed around the conduction band which is far from the original valence band. Therefore, hole-doped $LaSrFeO_4$ still shows semiconducting transport although the activation energy for electrical conduction is considerably reduced.

Two-probe resistivity measurement performed on the samples shown in Fig.3.7 reveals the semiconducting nature of the $LaSrFeO_4$ matrix.

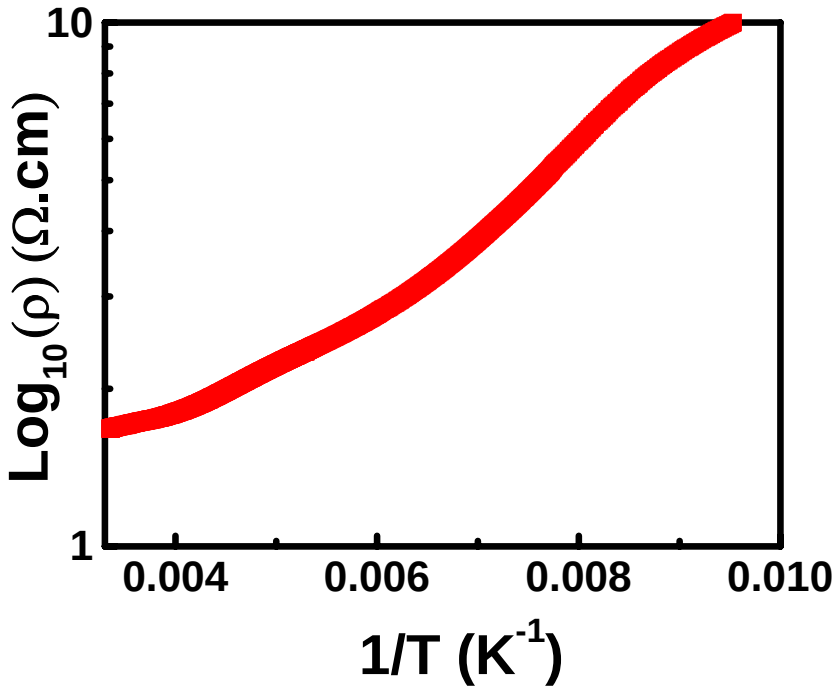

Fig.3.7 Two-probe resistivity measurements of the $LaSrFeO_4$ matrix showing the semiconducting properties of the matrix.

3.4 Calculation of α-Fe volume fraction

3.4.1 Theoretical calculation

By knowing the composition of the parent phase ($La_{0.5}Sr_{0.5}FeO_3$) and assigning the matrix and nanowire phases to $LaSrFeO_4$ and α-Fe, respectively the decomposition reaction can be expressed as:

$$2\ La_{0.5}Sr_{0.5}FeO_3 \rightarrow LaSrFeO_4 + Fe + O_2 \qquad \text{Eq.3.1}$$

Based on the crystal structure of the $LaSrFeO_4$ matrix (K_2NiF_4) with $Z = 2$, where Z is the number of molecular units per unit cell, and crystal structure of iron nanowires (b.c.c.) with $Z = 2$ and also considering their unit cell volume ($V_{u.c.} = 7.087\ cm^3$ for α-Fe and $V_{u.c.} = 58.32\ cm^3$ for $LaSrFeO_4$), the volume fraction of α-Fe to the total volume of the thin film (α-Fe and $LaSrFeO_4$ matrix) can be calculated.

Therefore, the total α-Fe volume is calculated to be around ≈ 10.95%, which is in fair agreement with the values calculated from both the Mössbauer spectroscopy areal density (described below) and the percentage observed in transmission electron microscopy images.

3.4.2 Mössbauer spectroscopy

Taking into account the density and molecular weights of iron ($\rho_{Fe} = 7.85\ g/cm^3$, $A_{Fe} = 55.845$ g) and $LaSrFeO_4$ ($\rho_{LaSrFeO4} = 5.99\ g/cm^3$), $A_{LaSrFeO4} = 349.368$ g), we can calculate the volume fraction of iron nanowires in the total volume of the thin film from the areas of the Mössbauer spectral components (53% α-Fe and 47% $LaSrFeO_4$) obtained from Fig.3.5 as shown below:

$$\frac{V_{nanowires}}{V_{matrix} + V_{nanowires}} = \frac{0.53 \times \frac{55.845(g)}{7.85(g/cm3)}}{0.47 \times \frac{349.368(g)}{5.99(g/cm3)} + 0.53 \times \frac{55.845(g)}{7.85(g/cm3)}} \cong 0.12 \qquad \text{Eq.3.2}$$

This shows that iron nanowires comprise approximately 10.95% of the whole film volume. This value is in agreement with the theoretical calculations mentioned above and the estimated volume fraction obtained from the plan-view TEM image shown in Fig.3.2 A.

3.5 Controlling the density of α-Fe nanowires

Denser assembly of the iron nanowires in the matrix is desired both because it will lead to higher storage densities in magnetic recording media applications and also because bringing the iron nanopillars closer to each other may result in elastic interaction between the pillars and force them to organize in an ordered fashion. It may be possible to increase the density of the self-assembled iron nanowires by increasing the amount of the iron in the original $La_{1-x}Sr_xFeO_{3-x}$ target. This may result in decomposition of more iron and the formation of a denser assembly of iron nanowires.

This concept can be demonstrated by using the theoretical calculations. Eq.3.1 can be rewritten as below:

$$LaSrFe_2O_6 \rightarrow LaSrFeO_4 + Fe + O_2 \qquad \text{Eq.3.2}$$

As mentioned above this leads to the formation of approximately 11% iron nanowires in the total volume of the thin film. If we increase the amount of iron to twice its original value, the theoretical calculation predicts that the amount of decomposed iron should increase to 3 times its value as shown below:

$LaSrFe_4O_6 \rightarrow LaSrFeO_4 + 3Fe + O_2$ Eq.3.3

Therfore, if the deposition is performed using the above mentioned target, the iron nanowires should occupy approximately $\approx 33\%$ of the total volume of the film.

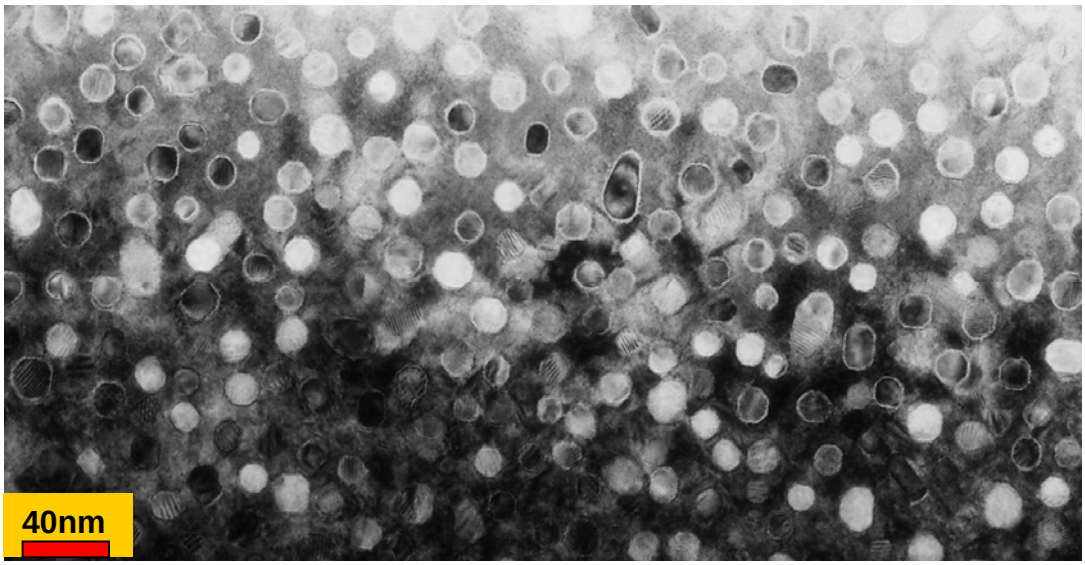

Fig.3.8 Plan-view TEM images of iron nanopillars from the sample made by using iron induced target of $La_{0.5}Sr_{0.5}Fe_2O_3$. The temperature of growth was T = 660 °C.

Targets with 2 and 3 times more iron were obtained and the experiments were performed. The best results were obtained when the target with twice amount of iron was used and the temperature of the deposition was reduced to T = 660 °C. A plan-view TEM image of this sample is shown in Fig.3.8 which indicates that the amount of the decomposed iron second phase is increased to the values predicted

theoretically. The average diameter of the nanowires (d ≈ 15-20 nm) is close to that of the samples deposited at T = 760 °C using the original $La_{0.5}Sr_{0.5}FeO_{3-X}$ target. This is expected as at higher volumes of decomposed iron where the distance between two iron nuclei is reduced. This facilitates the diffusion of iron as the distance that iron atoms need to travel is 3 times shorter and therefore results in larger diameter iron nanowires in lower temperatures. The growth mechanism will be discussed in details in the next chapter. As shown in Fig.3.8 some local degree of order is observed between the nanowires in this image but long range order is not achieved. Therefore, the amount of iron in the target may need to be increased to some higher values.

Increasing the iron value in the target to 2.2 and 2.3 times its original value did not cause any significant changes. However, obtaining good quality films was more difficult for these targets. Increasing the amount of iron in the target to 3 times the original value not only did not give rise to any improved results but also prevented the formation of iron nanowires observed in Fig.3.2 and Fig.3.8. In this case, theoretical calculations predict decomposed iron volume of approximately ≈ 44%. Reducing the growth temperature down to even T = 500 °C did not produce any columnar iron structures. Further reducing the growth temperature to below < 500 °C resulted in poor epitaxy in the deposited thin films. The magnetic properties of the films deposited from this target were very different from square-shaped loops obtained from iron nanowires (the details of the magnetic properties will be discussed in Chapter 5). In the XRD analysis there are no visible peaks which can be assigned to the $LaSrFeO_4$ matrix or iron phases. It is possible that due to the short diffusion distance, iron forms in the shape of big blocks and covers most of the substrate or due

to the fact that the target is super saturated the iron phase does not completely separate from the $LaSrFeO_4$ matrix and therefore the crystalline phases do not form. If the decomposed components are polycrystalline and epitaxy does not exist between the two phases, then columnar structures are not expected to be observed.

3.6. Growth on silicon substrate

The success of new metal-oxide nanostructures or nanocomposites for practical applications in the industry largely will depend on the feasibility of their implementation on silicon-based substrates. The lattice parameter of silicon (a = 0.543 nm) is very different from the $SrTiO_3$ (a = 0.3905 nm) used for growth of the self-assembled iron nanowires embedded in $LaSrFeO_4$ matrix. Therefore, the growth of these nanostructures on top of Si substrate will not lead to formation of columnar structures. To be able to grow these nanowires on silicon substrate, $SrTiO_3$/Si (001) substrates were prepared at Pennsylvania State University where a few monolayers of $SrTiO_3$ are grown on top of the Si (001) substrate using molecular beam epitaxy (MBE). The epitaxial growth of $SrTiO_3$ on silicon is possible by 45° in-plane rotation. The iron nanowires were then deposited on top of these substrates. The X-ray diffraction data and the plan-view TEM image shown in Fig.3.9 A,B reveal that the nanostructures have been successfully formed on these substrates. The difference in the planar structure of these nanowires (well-defined square shapes) is due to the difference in the growth temperature which will be discussed in detail in the following chapter.

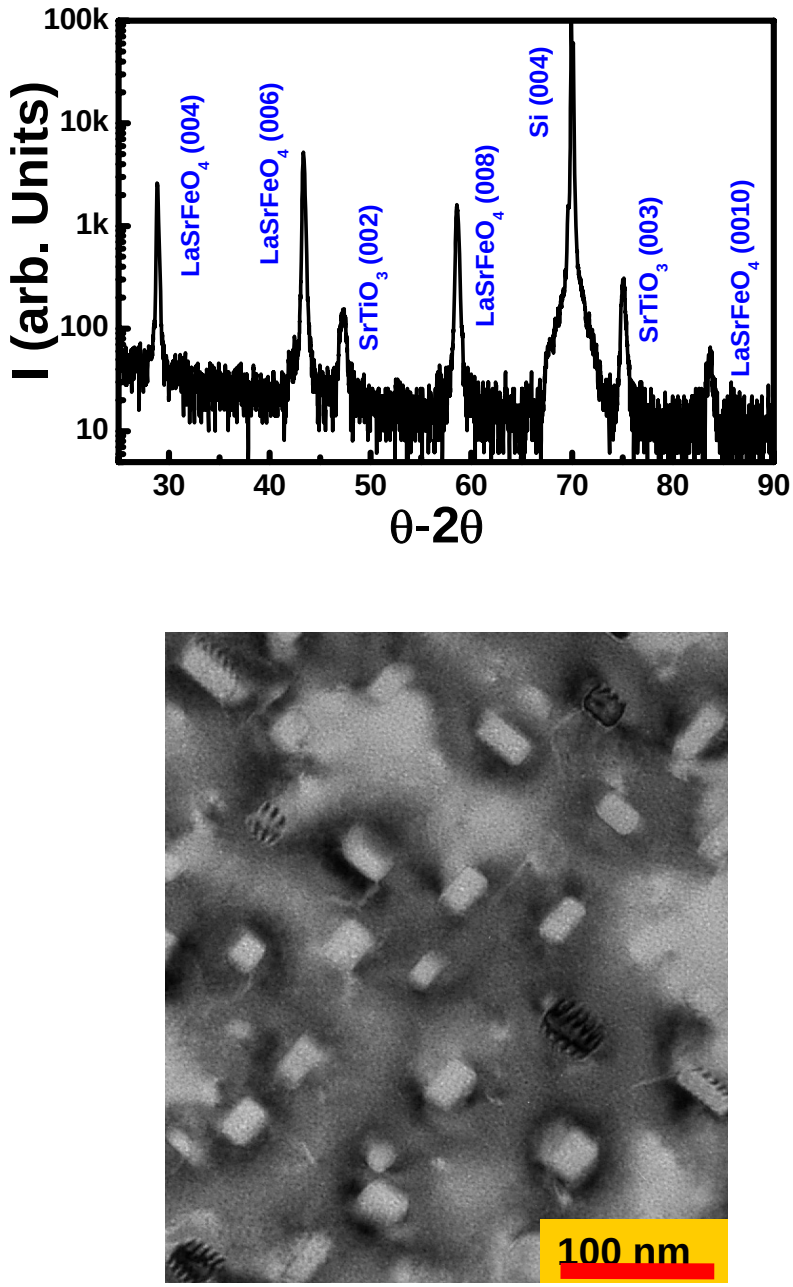

Fig.3.9 A. X-ray θ-2θ scan showing (00l) families of peaks; B. Plan-view TEM images of the nanopillars grown on top of the STO/Si (001) substrate.

3.7 Annealing self-assembled α-Fe nanowires

To study the effect of introducing oxygen to the thin films after growth the samples were annealed at oxygen in temperatures between T = 300 – 400 °C for t = 30 min. The magnetization hysteresis loops obtained from the samples after annealing showed a straight line indicating that no magnetization state existed in the samples. This indicates that some structural or compositional changes may have occurred in the samples.

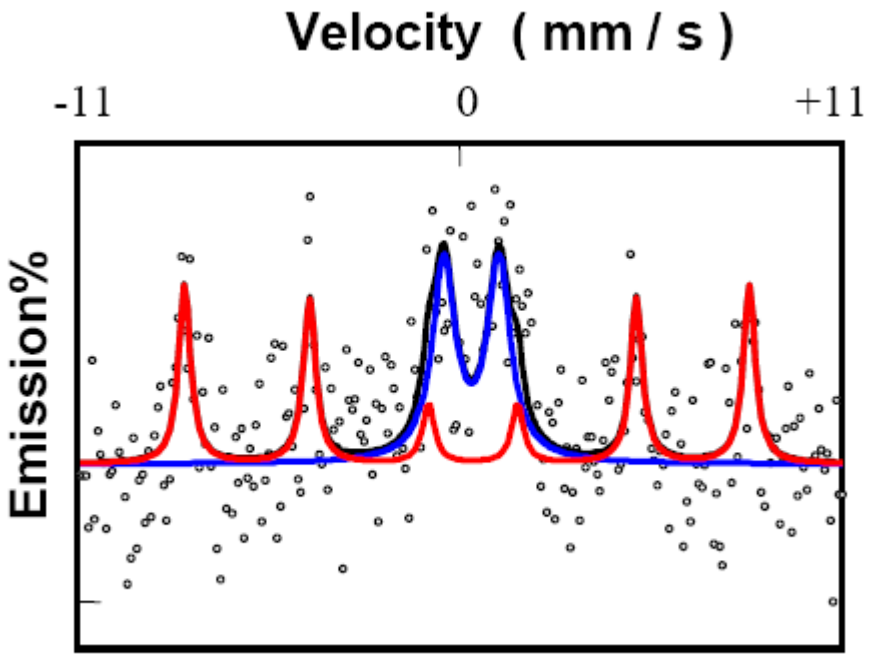

Fig.3.10 Room-temperature ^{57}Co conversion electron Mössbauer spectrum (CEMS) of the film annealed in oxygen after deposition in vacuum (experimental points (black solid line) and the fit). The spectrum is composed of a superposition of two sub-spectra: the sextet of antiferromagnetic α-Fe_2O_3 (red) and the paramagnetic doublet of the non-stoichiometric $LaSrFeO_4$ matrix (as a part of main spectrum).

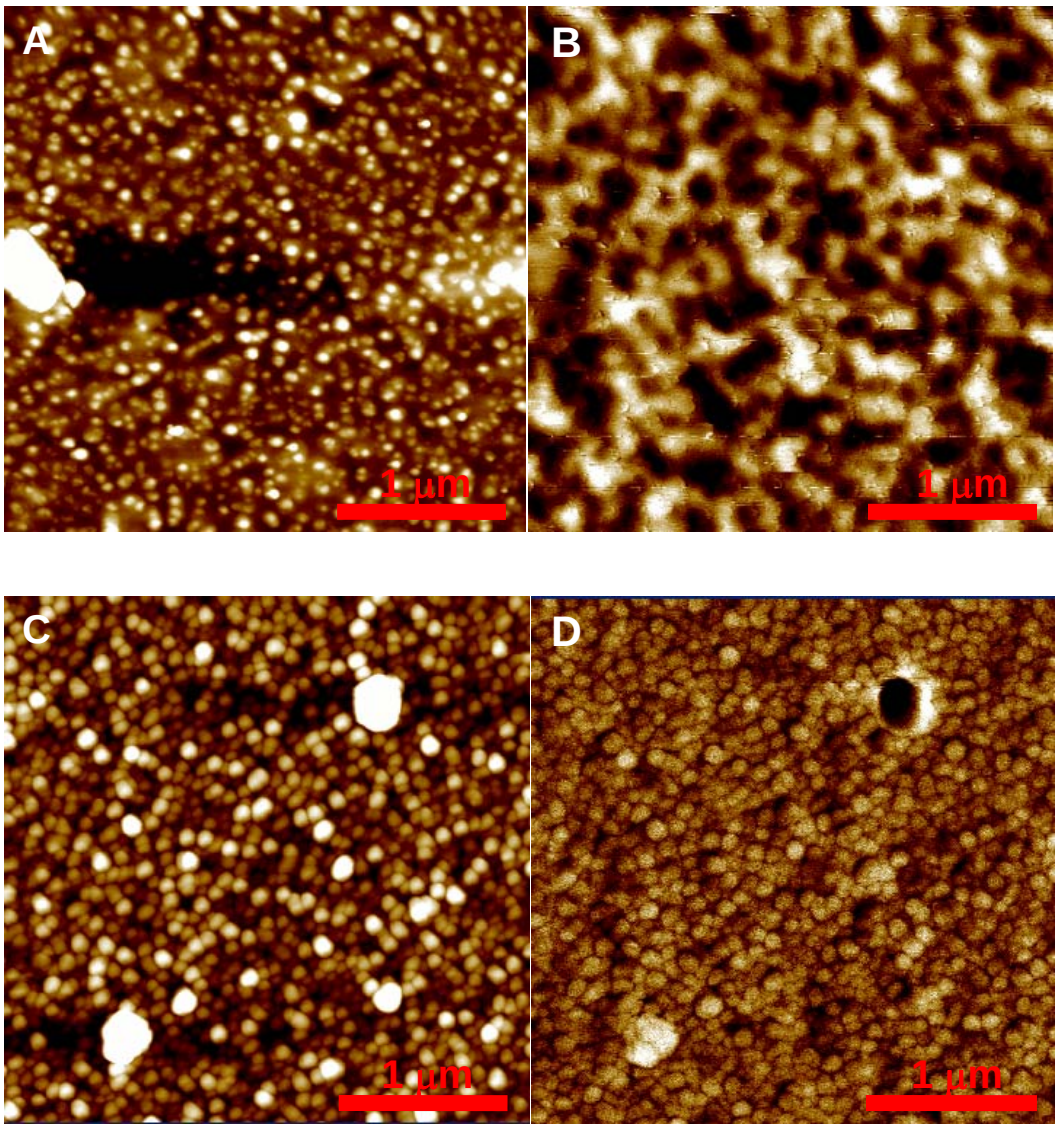

Fig.3.11 AFM (left) and MFM (right) images of the A, B. as deposited iron nanowires, and C, D. iron nanowires annealed in O_2 atmosphere.

Conversion electron Mössbauer spectroscopy was used to identify the composition of the films after annealing. The Mössbauer spectrum recorded at room temperature is shown in Fig.3.10. The result reveals that the spectrum consists of two sub spectrum.

The first one is a quadrupole split doublet of paramagnetic matrix $La_{1-x}Sr_{1+x}FeO_4$ (with quadrupole splitting of QS = 1.59 mm/s and isomer shift of IS = 0.40 mm/s) which indicates that the matrix remains structurally unchanged after annealing. However, the second sub spectrum is an antiferromagnetic sextet where its hyperfine parameters (Isomer Shift (IS) = 0.36 mm/s, Internal Magnetic Field = 50.6 Tesla) are in very good accordance with antiferromagnetic iron oxide α-Fe_2O_3 or hematite.

Hematite is an iron-oxide with lattice parameters $a = b = 0.50317$ nm and $c = 1.3737$ nm. The structure is similar to that of corundum, and consists essentially of a dense arrangement of Fe^{3+} ions in octahedral coordination with oxygen in hexagonal closest-packing. The structure can also be described as the stacking of sheets of octahedraly coordinated Fe^{3+} ions between two closed-packed layers of oxygens. Since Fe is in a trivalent state, each oxygen is bonded to only two Fe ions, and therefore, only two out of three available oxygen octahedrons are occupied. This arrangement makes the structure neutral with no charge excess or deficit.

Therefore, annealing in O_2 oxidizes the iron pillars to antiferromagnetic hematite. This explains the absence of a magnetic hysteresis loop in annealed samples. Fig.3.11 compares the topography of the films before and after annealing. Atomic force microscopy images show a difference in the surface of the films. The annealed sample has coarser topography and bigger grain sizes (Fig.3.11 C) compared to the deposited samples (Fig.3.11 A). This is expected as the there is about 30% increase in volume for α-Fe (b.c.c.) to α-Fe_2O_3 (rhombohedral) phase transformation. Magnetic force microscopy images taken from the nanowires (Fig.3.11 C,D) shows no

magnetic contrast in the oxygen annealed samples which confirms the formation of the antiferromagnetic α-Fe_2O_3.

Taking into account the density and molecular weights of α-Fe_2O_3 ($\rho_{\alpha\text{-}Fe2O3}$ = 5.28 g/cm^3, $A_{\alpha\text{-}Fe2O3}$ = 159.69 g) and $LaSrFeO_4$ ($\rho_{LaSrFeO4}$ = 5.99 g/cm^3), $A_{LaSrFeO4}$ = 349.368 g), we can calculate the volume fraction of α-Fe_2O_3 in the total volume of the thin film from the areas of the Mössbauer spectral components (52% α-Fe_2O_3 and 48% $LaSrFeO_4$) obtained from Fig.3.10 as shown below:

$$\frac{V_{nanowires}}{V_{matrix}+V_{nanowires}} = \frac{0.52\times\dfrac{159.69(g)}{5.28(g/cm3)}}{0.48\times\dfrac{349.368(g)}{5.99(g/cm3)}+0.52\times\dfrac{159.69(g)}{5.28(g/cm3)}} \cong 0.36$$

The results are in agreement with the AFM images shown in Fig.3.11 and confirm that after annealing the volume of the resulting α-Fe_2O_3 is about 3 times larger than α-Fe nanowires. Transmisson electron microscopy was performed on the annealed samples to confirm the structure and composition of the nanopillars and matrix. Fig.3.12 A shows low magnification plan-view TEM image from a sample deposited at T = 740 ºC on $SrTiO_3$/Si (001) substrate in vacuum atmosphere and subsequently annealed in O_2 environment (T = 350 °C). The image clearly demonstrates that the diameter of the nanowires has increased from d = 17 nm to around 40 nm. The electron diffraction pattern (Fig.3.12 B) shows that although $LaSrFeO_4$ matrix remains crystalline, α-Fe_2O_3 is polycrystalline. This is expected from the approximate %30 volume difference between iron and hematite. It should be noted that although the sample were grown on (001) substrate, the zone axis for electron diffraction pattern was [111]. This is due to the tilt in the sample caused by ion-milling.

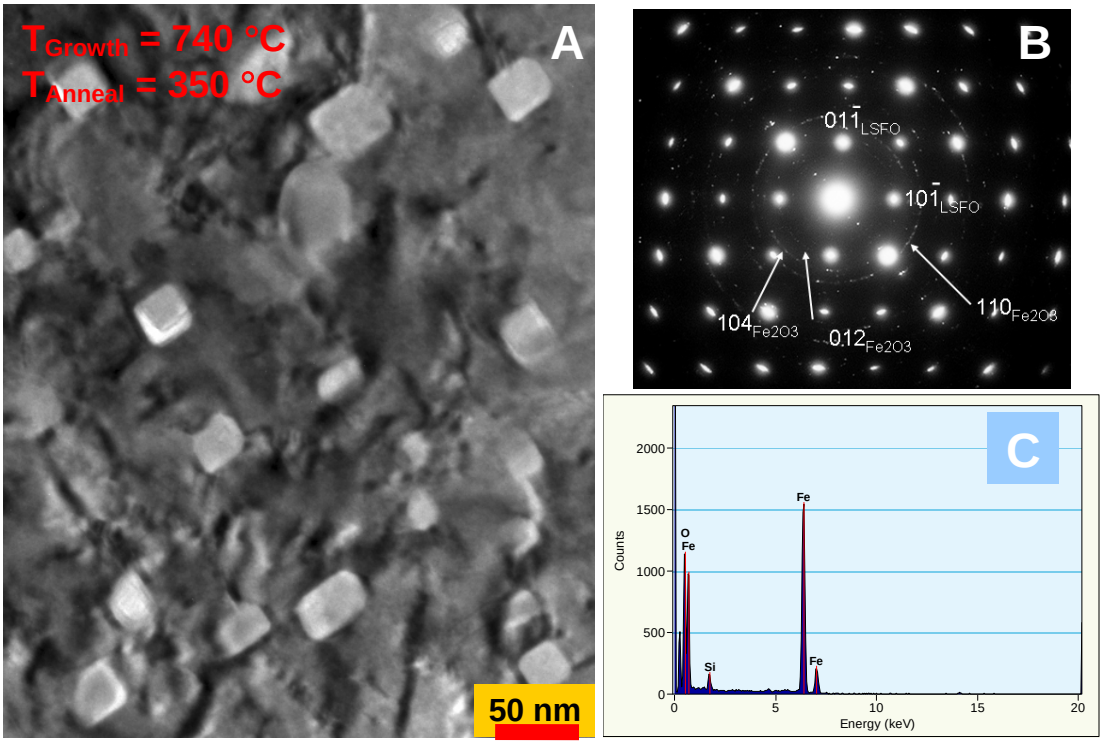

Fig.3.12. A. Plan-view TEM images of the annealed nanopillars grown on top of the STO/Si (001) substrate; B. Electron diffraction pattern illustrating the epitaxial $LaSrFeO_4$ matrix and poly crystalline α-Fe_2O_3; EDXS spectrum from a single hematite nanopillar.

Chapter 4 Shape and Size Evolution of the α-Fe Nanowires

4.1 Introduction

The previous chapter discussed how the deposition of $LaSrFeO_3$ perovskite in a vacuum atmosphere on a lattice matched substrate such as $SrTiO_3$ leads to the decomposition of the perovskite target. This results in the formation of the iron second phase in the shape of nanowires which are embedded in a $LaSrFeO_4$ oxide matrix. Experimental analysis such as TEM and Mössbauer spectroscopy revealed that the embedded iron nanowires occupy around 11% of the total volume of the thin film, which was in agreement with theoretical calculations.

This chapter focuses on the temperature dependence of the growth and show that the lateral size and spacing of the iron nanowires changes with respect to the growth temperature. By fitting the temperature dependence of the data to different theoretical models, the mechanism of the iron nucleation, diffusion and growth is studied and discussed.

In addition, it is observed that the cross-sectional shape of the nanowires also changes as the growth temperature and therefore the size of the nanowires varies. The shape evolution is studied by considering two different approaches. First it is shown that the equilibrium shape can be predicted using crystallographic group theory, and second the energies involved in the system are taken into account to theoretically calculate the stable lateral shape of the nanowires in different growth temperatures. The values obtained by these calculations are compared with the experimental data to

obtain a critical lateral size when the shape transition takes place in the iron nanowires.

4.2 Temperature dependence of the lateral size of the iron nanowires

The effect of the growth temperature on the formation of the iron nanowires was studied by systematically depositing the samples at different substrate temperatures. Plan-view TEM images of the samples deposited at various temperatures reveal an interesting feature of these nanostructures. Fig.4.1 shows the plan-view TEM images of the nanowires grown at different temperatures. As observed in these images, the lateral dimensions of the nanostructure are strongly temperature dependent. It can be seen that the lateral dimensions of the α-Fe nanowires decrease as the growth temperature is reduced. The average diameter of the epitaxial nanowires is around $d_{avg} \approx$ 45-55 nm at the highest growth temperature of $T \approx$ 840 °C. The lateral size of the nanowires decreases to $d_{avg} \approx$ 14-18 nm at $T \approx$ 740 °C and finally to $d_{avg} \approx$ 3-5 nm as the deposition temperature is reduced to $T \approx$ 560 °C.

It is interesting that the nanostructures grown at $T \approx$ 560 °C with small diameter of 3-5 nm are also single crystalline and form thin nanowires which mostly grow from the top of the substrate and expand through the whole thickness of the film. Fig.4.2 shows a cross-section high resolution TEM image of one of the 3-5 nm nanowires taken from its middle section. The image clearly demonstrates the crystallinity of the nanowires with small diameters.

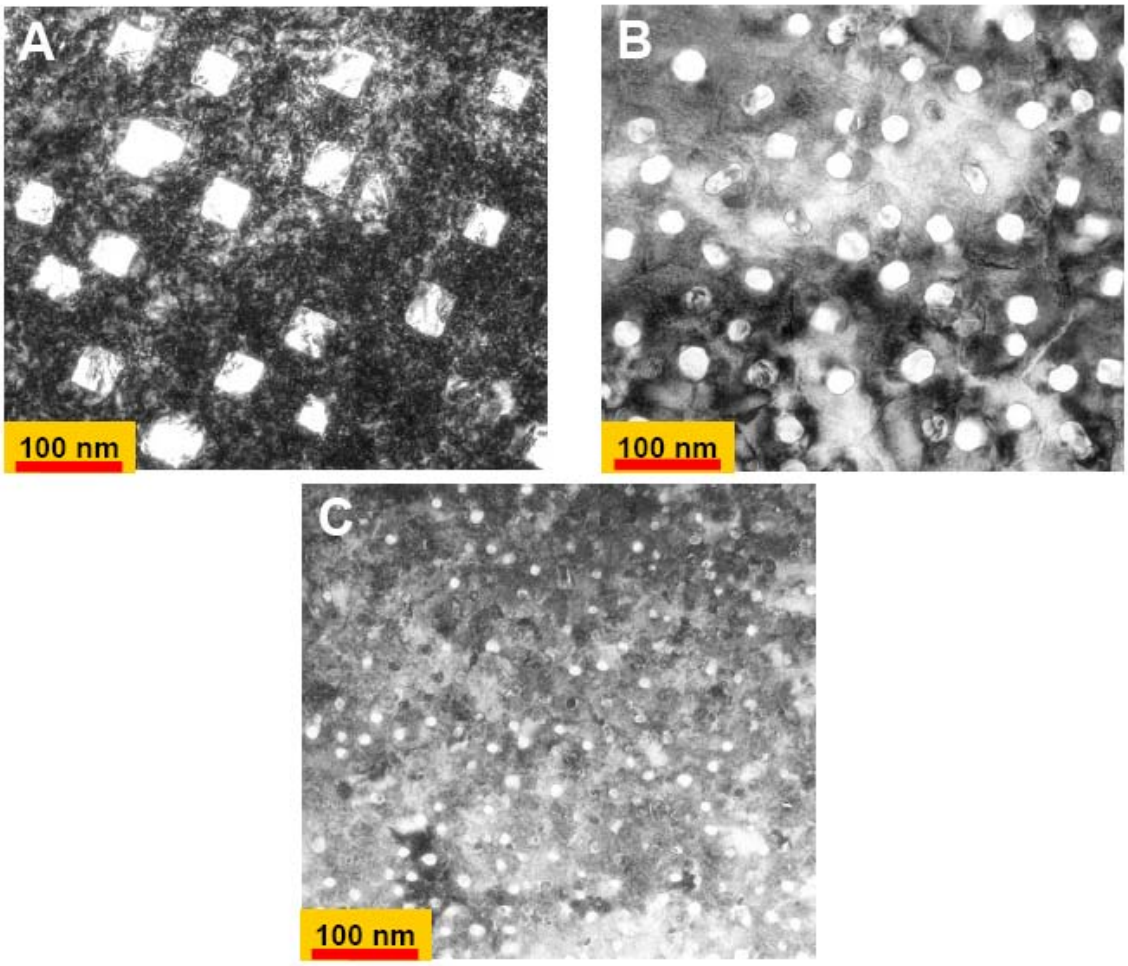

Fig.4.1 Plan view TEM images of the films grown in vacuum at various temperatures. A. T = 840 °C, B. T = 740 °C, and C. T = 560°C.

Fig.4.3 shows statistical size distributions of the nanowires grown at T = 840 °C (Fig.4.3 A), T = 740 °C (Fig. 4.3 B) and T = 560 °C (Fig.4.3 C). The size distribution fits a Gaussian distribution with mean diameters of d = 50, 16 and 4 nm for T = 840, 740 and 560 °C, respectively. It also shows that for the nanowires grown at T = 740

°C and T = 560 °C, 95% of the nanowires are within the size range of d = 15-20 nm and d = 3-6 nm, respectively. For the samples grown at T = 840 °C, the size distribution of the second phase is slightly larger and 85% of the pillars are within the size range of d = 45-55 nm.

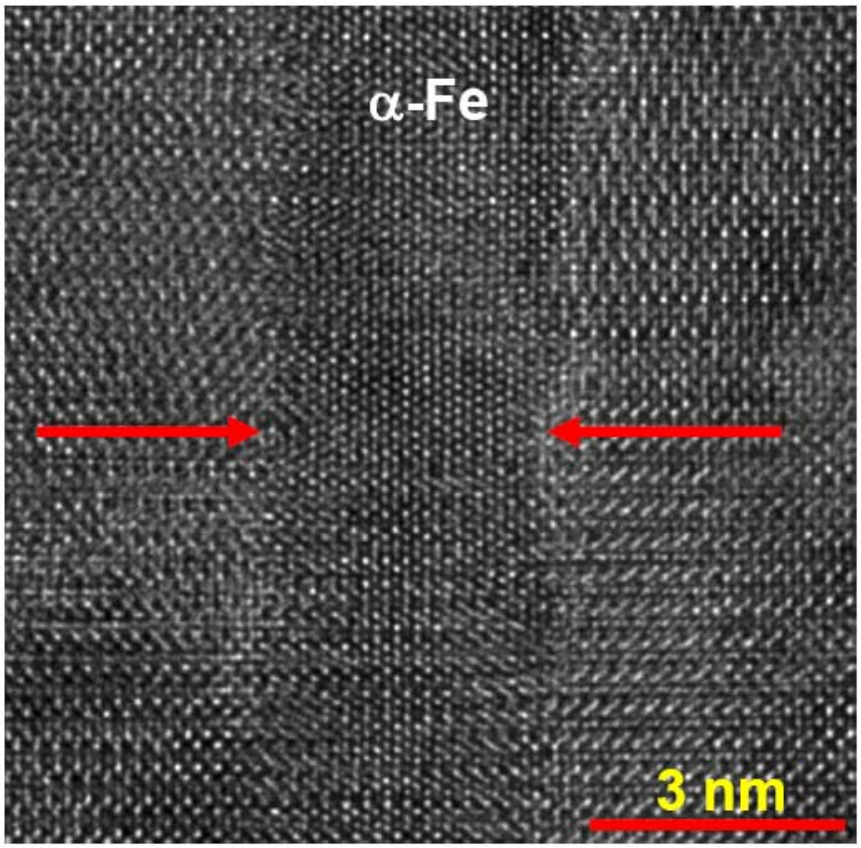

Fig.4.2 High resolution cross-section images of a single α-Fe nanowire which shows the single crystalline nature of the smallest nanowires. The growth temperature is $T \approx$ 560 °C.

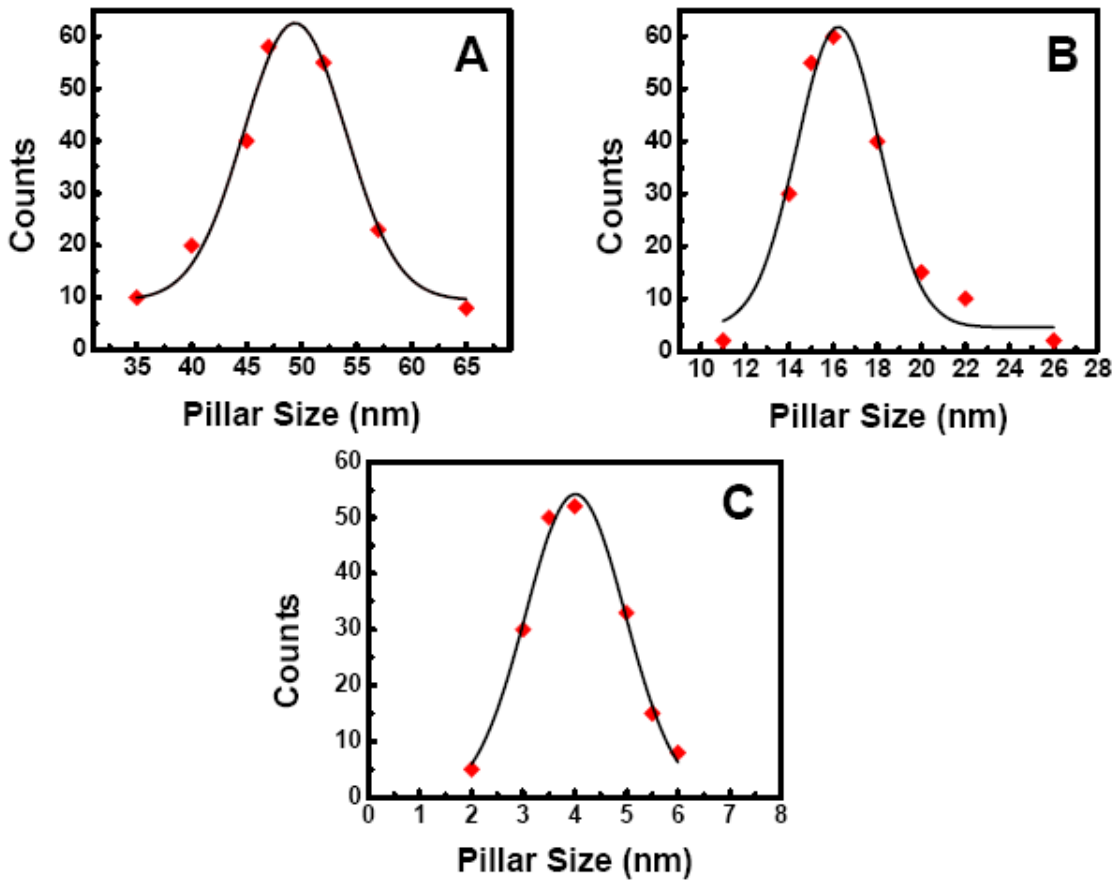

Fig.4.3 The lateral size distribution of the nanopillars deposited at A. T = 840 °C, B. T = 740 °C and, C. T = 560 °C.

In Fig.4.4 the temperature dependence of the Fe nanowires lateral dimension is plotted. As shown in this Figure, it is possible to fit the temperature dependence of the lateral dimension to an Arrhenius type behavior. In addition as mentioned before, using TEM imaging and Mössbauer spectroscopy analysis we have shown that the volume fraction of the Fe nanopillars in the total volume of the deposited thin film

can be calculated to be approximately 11%, which is independent of the deposition temperature. The Arrhenius type behavior of the size evolution of the iron nanowires in addition to the constant volume fraction suggests that the growth of the nanowires is kinetically controlled by diffusion during the deposition[67,68].

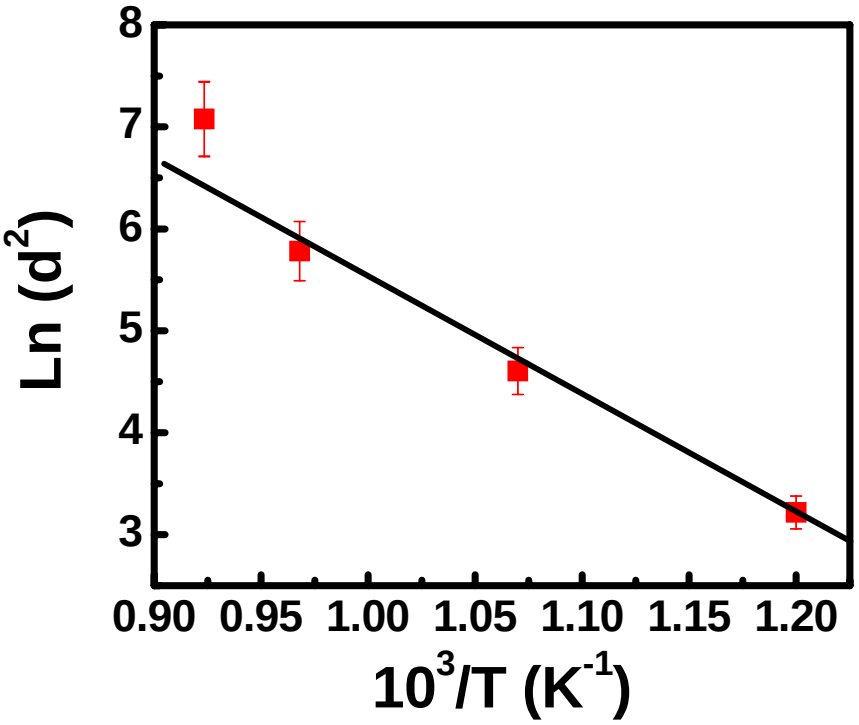

Fig.4.4 Arrhenius fit of the lateral dimension of the α-Fe nanowires as a function of growth temperature.

It is evident that at lower deposition temperatures diffusion is less important and the nucleation of the iron second phase is the dominant process. Since the mobility of the atoms and therefore their mean free path is small, the diffusion length is short at low temperatures. As a result the nucleation of many small iron second phase nucleation

sites is favored. At higher deposition temperature we have stronger diffusion according to the Arrhenius factor of the diffusion rate; the atoms become more mobile, the mean free path is larger and as a result the attachment of single iron atoms to an existing iron second phase nucleus is favored. This leads to the formation of fewer and larger embedded iron second phase nanostructures. Therefore, in the kinetically controlled growth regime the average nuclei size is proportional to the diffusion length and thus increases with temperature.

From the Arrhenius linear fit to Fig.4.4, we can calculate the activation energy of the formation of α-Fe nanostructures to be approximately $E \approx$ 1.0-1.2 eV depending on the fit. By knowing the activation energy we can use the deposition-diffusion-aggregation model[69] to calculate the diffusion length of the atoms (l) during the deposition. The diffusion length (l), which equals the average distance between nucleation sites, can be estimated with a power law dependence of the ratio between the surface diffusion constant ($D, D = D_0 e^{-E/k_B T}$) and the diffusion rate (F) which is shown in the equation below:

$$l \approx (D_0 e^{-E/k_B T} / F)^{\gamma} \qquad \text{Eq.4.1}$$

where $\gamma = 0.25$, k_B is the Boltzman constant and $D_0 = \frac{1}{4} a_0^2 v_0$ where a_0 is the lattice constant and v_0 is a single atom's hopping frequency, which is generally assumed to be $v_0 = 10^{13}$ sec^{-1} for a variety of semiconductor materials. Considering the deposition rate of F = 0.15 nm/sec and fitting different values of activation energy between 1.0 $\leq E_v \leq$ 1.2 eV to the equation, it is found that the distance between nucleation sites is around l = 46 and 16 nm for the samples deposited at T = 740 and 560 °C,

respectively. These values are very close to the average distance between the nanowires observed from TEM plan-view images. The activation energy of E_v = 1.1 eV yields a value of l = 80 nm for the samples grown at T = 840 °C, which is far below the experimentally observed average distance of around 120 nm.

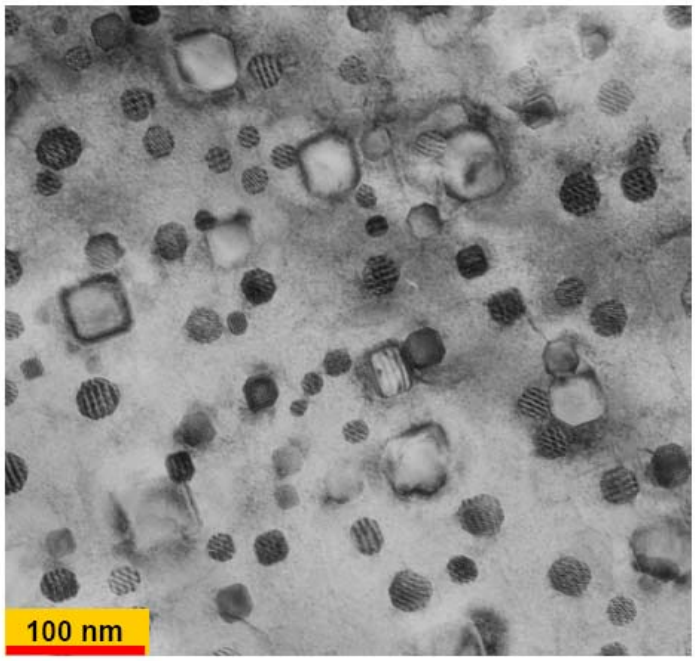

Fig.4.5 Plan-view TEM image of the sample deposited in vacuum at T = 870 °C showing wide size distribution in iron nanowires.

The broadening of the statistical lateral size distribution of the iron second phase nanowires at higher growth temperature observed in Fig.4.3, is generally observed in the kinetically controlled growth regime[69]. Below a critical transition temperature the average island size increases with the temperature and a rather narrow size distribution (broadening with increase in temperature) is observed. If the temperature

is raised above this critical temperature a transition from the kinetically to thermodynamically controlled growth mode occurs. In the thermodynamically controlled growth regime the atoms attached to a nucleation site can easily detach from larger nuclei and the nuclei lose their stability. This will lead to the nucleation and growth of smaller, more stable islands at the expense of the larger ones with less stable boundaries. Therefore a rather sharp increase in broadening of the size distribution is observed. In Fig.4.5 an example of a film grown at T = 870 °C is shown. It is observed that in this sample a broad range of size distribution exists ranging from d = 10 to 55 nm. The majority of the nanowires have smaller lateral sizes ($d_{avg} \approx$ 25 nm) compared to the ones deposited at T = 840 °C. Therefore, the transition from the kinetically to the thermodynamically growth mode occurs above T = 840 °C.

The temperature dependence of the iron nanowires diameter can be explained with a Zener type analysis. In the kinetically controlled growth mode, by reducing the temperature of deposition, the size and spacing between the iron nanowires will decrease. As mentioned above, this strong temperature dependence of the diameter of the nanowires, d, and their spacing, S, suggests a kinetically controlled diffusion growth. The kinetics of the growth can also be explained with a Zener type approach[70]. According to Zener a particular value S^* can be expected that represents a compromise between the total interface energy of the two phases in contact (one embedded in the other), which increases with 1/S, and mean diffusion path which increases with S. Since the volume of the decomposition products (iron nanowires) is constant at different temperatures of deposition, the fits conform to $d/S \approx$ constant.

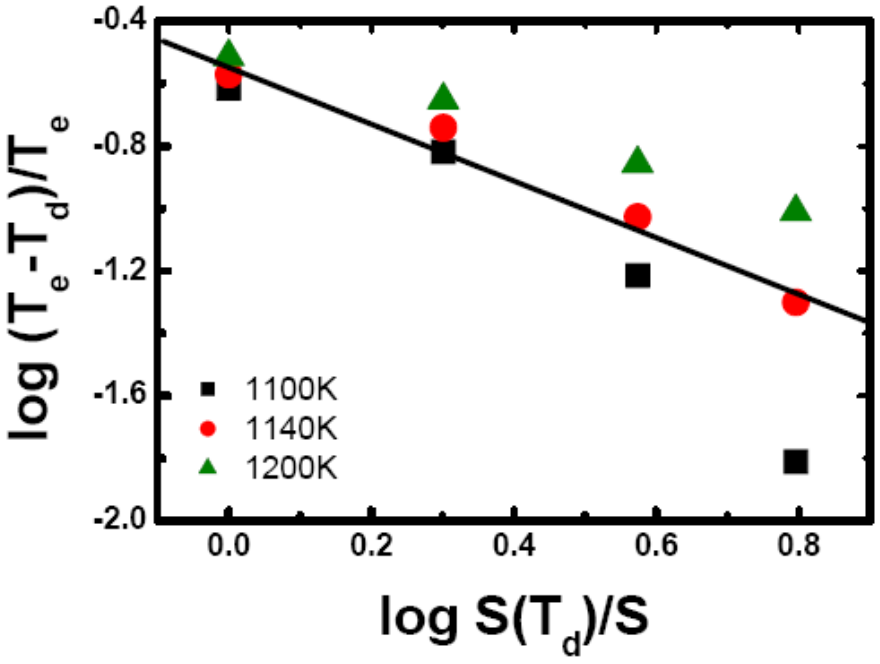

Fig.4.6 Logarithmic plot of normalized undercooling vs. nanowire spacing for three different values of T_e. The slope of the straight line equals -1.

The Arrhenius type dependences of the dimensions of the epitaxial nanocomposite imply that the decomposition takes place at the deposition temperature, T_d. The reaction occurs at a very fine scale and creates interfaces with interfacial energy of γ. It will therefore take place at a temperature that is suppressed below the thermodynamical equilibrium temperature between the two phases, T_e. The total interface energy can be approximated to be proportional to $\gamma \approx \alpha dh\gamma(L/S)^2$. Here, the quantity α is a geometrical constant, and h and L^2 represent the nanowires' height and

the area of the film, respectively. This energy should correspond to the thermal energy of k_B (T_e – T_d) where k_B is the Boltzman constant. Because the ratio d/S is constant, it follows that for a constant geometry (T_e– T_d) $\propto S^{-1}$. A logarithmic plot of $\Delta T = (T_e - T_d)$ versus S should thus be approximately linear with a slope of –1. Fig.4.6 shows this logarithmic plot for temperatures of T_e = 1100, 1140, and 1200 K. The plot indicates that for $T_e \approx 1140$ K the slope equals the expected value of -1. This is very close to the temperature where the transition between the kinetic and the thermodynamic growth mode occurs.

The ratio of d/S is constant for a specific composition of the original target material, $La_{0.5}Sr_{0.5}FeO_3$. However, this ratio can be controlled through the amount of Fe available for the phase decomposition reaction in the original target as mentioned in Chapter 3. It was shown in Fig.3.7 that by using an iron rich target, where the iron amount was twice its original value, the amount of iron nanowires was increased from 11% to 33%.

4.3 Lateral shape changes of the iron nanowires

The previous section discussed the temperature dependence of the diameter of the nanowires and their spacing and showed that their growth is kinetically controlled by diffusion during growth. Simultaneously, the in-plane shape of the nanowires changes as the temperature of deposition and therefore the size of the nanowires increases.

Fig.4.7 shows plan-view high resolution transmission electron microscopy (HRTEM) results obtained from nanowires grown at three different temperatures.

This shows the changing cross-sectional shape of the iron nanowires and reveals low-index faceted interfaces. The nanowires grown at temperature around T = 560 °C have circular shape with average diameter of about d = 4 nm, see Fig.4.7 A. The shape evolves to an octahedral form with only [110] and [100] facets observed as the temperature of deposition increases. An example is shown in Fig.4.7 B for the film grown at T = 740 °C, where the average lateral size of the octahedron shaped nanowires is around d = 16 nm. Finally, nanowires with almost square shaped cross-sections and mean diameter of d = 50 nm are formed when the growth temperature is further raised to T = 840 °C, as shown in Fig.4.7 C. The equilibrium shapes are all symmetric with [110] facets dominating in square-shaped iron nanopillars.

In this section, first the symmetrical shapes of the iron nanowires is discussed and it is shown that symmetrical interfaces can be predicted and explained by crystallographic symmetry and group theory. Then, the temperature dependence of nanowires' shapes are studied and fitted to the theoretical calculation obtained from the literature. It is shown that the observed shape evolution and stable shapes at different lateral sizes are the result of competition and equilibrium between both the surface energy and elastic strain energy effects.

4.3.1 Crystallographic symmetry and group theory

Group theory can be considered the study of symmetry. The rules that govern symmetry are found in the mathematics of group theory which addresses the ways in which a certain collection of mathematical objects are related to each other.

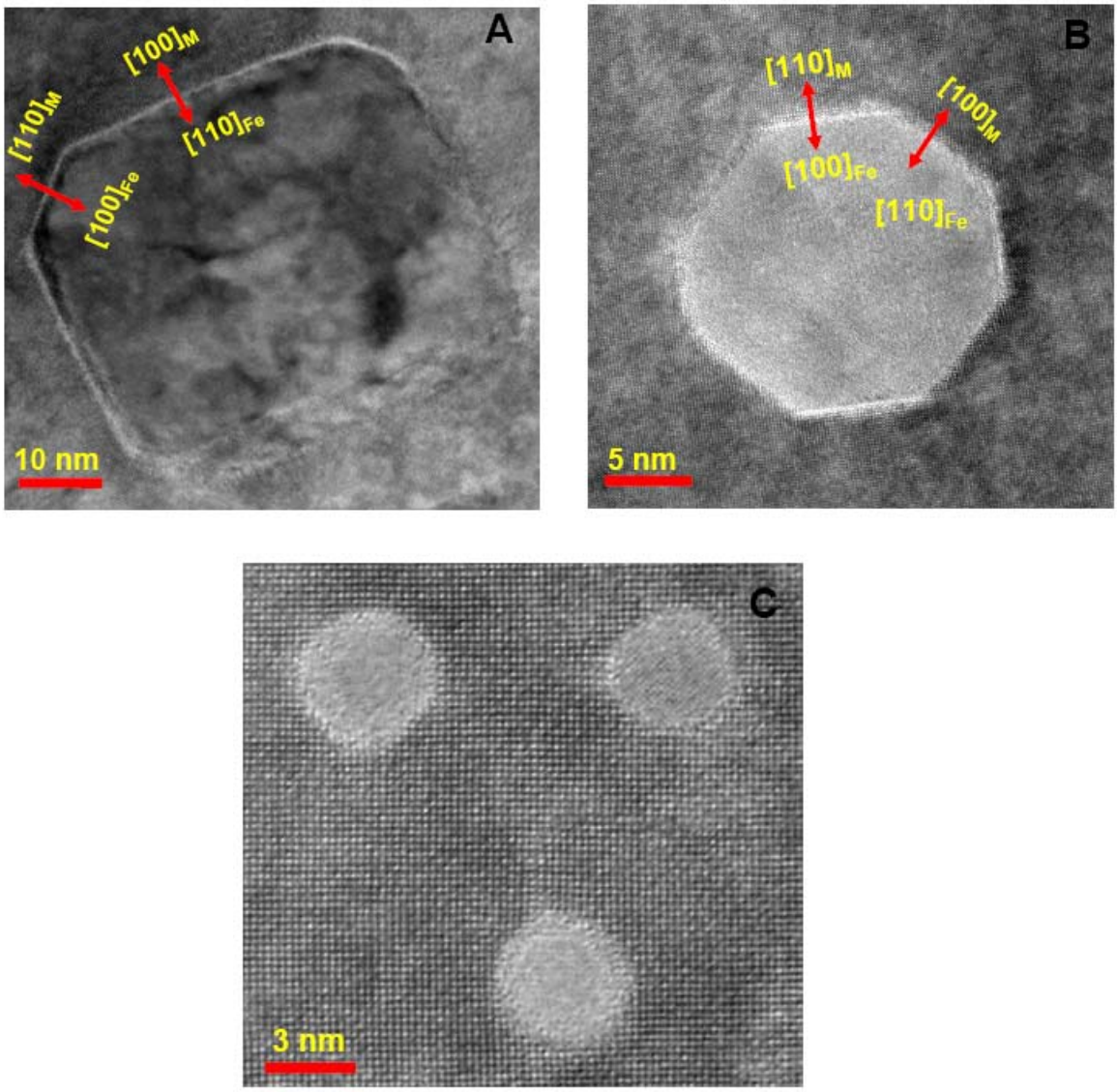

Fig.4.7 High resolution plan-view TEM images of α-Fe nanowires showing the shape and lateral size (d) dependence of the nanowires on deposition temperature. A. Square-shaped 40-50 nm nanowires are obtained at T = 840 °C; B. octagonal cross section with d = 15-20 nm form at T = 740 °C and C. circular nanowires form at T = 560 °C (d = 3-5 nm).

In general there are five operations with respect to a group: the identity operation, rotation about an axis, reflection through a plane, inversion through a center, and rotation about an axis followed by reflection through a plane perpendicular to that axis. Each of these symmetry operations is associated with a symmetry element which is either a point, a line, or a plane about which the operation is performed such that the orientation and position of the object before and after the operation are indistinguishable.

Crystal System	Number of Point Groups	Herman-Mauguin Point Group	Schoenflies Point Group
Triclinic	2	1, $\bar{1}$	C_1, C_i
Monoclinic	3	2, m, 2/m	C_2, C_s, C_{2h}
Orthorhombic	3	222, mm2, mmm	D_2, C_{2v}, D_{2h}
Trigonal	5	3, $\bar{3}$, 32, 3m, $\bar{3}$m	C_3, S_6, D_3, C_{3v}, D_{3d}
Hexagonal	7	6, $\bar{6}$, 6/m, 622, 6mm, $\bar{6}$2m, 6/mmm	C_6, C_{3h}, C_{4h}, D_6, C_{6v}, D_{3h}, D_{6h}
Tetragonal	7	4, $\bar{4}$, 4/m, 422, 4mm, $\bar{4}$2m, 4/mmm	C_4, S_4, C_{4h}, D_4, C_{4v}, D_{2d}, D_{4h}
Cubic	5	23, m$\bar{3}$, 432, $\bar{4}$32, m$\bar{3}$m	T, T_h, O, T_d, O_h

Table 4.1 The 32 crystallographic point group.

Symmetry plays an important role in crystallography. The ways in which atoms are arranged within a unit cell and the way unit cells repeat within a crystal are governed

by symmetry rules. A crystallographic point group is a set of symmetry and a symmetry group. It can be shown that only 32 unique crystallographic point groups exist as shown in Table 4.1.

Crystallographic symmetry is an important factor in determining the morphology of crystals grown from or embedded in a solid crystalline matrix. The morphologies and symmetry properties of crystals embedded in a crystalline matrix can be explained by the group theory developed by Cahn and Kalonji[71]. It is well known that a crystal grown in an isotropic fluid must take forms compatible with its point symmetry. In solid-solid phase transformations, the matrix from which the new surface grows is anisotropic. Therefore, the symmetry arguments should take this into account and be extended to these systems.

4.3.1.1 Symmetry of heterophase interfaces

In general there are two types of interfaces: homophase and heterophase. Heterophase interfaces occur when two crystals belonging to two different phases adjoin. We can consider these two crystals to belong to two different crystallographic groups A and B and meet in a planar interface. Therefore, the interface should also belong to a symmetry group H, which is a subgroup of both the A and B groups and the symmetry properties of the interface should consist of those symmetry elements that are common to both crystals. Accordingly, the intersection has to be one of the 32 crystallographic point groups which is a subgroup of both crystal A and crystal B's point groups.

To find H, it is necessary to specify the orientation relationship between phase A and B. Cahn and Kalonji[71] have determined the interface group H by simply continuing one or both lattices past the interface to determine if any symmetry elements superimpose. Once the symmetry elements are found, the symmetry group H is known. This point group determines the possible forms that crystal B will take in the crystal A matrix with respect to a given orientation relationship. Cahn et al.[71] point out that symmetry is also useful in determining what relative orientation relationship will yield extrema in properties such as equilibrium energy of an inclusion of certain volume (determined by the interfacial and elastic energies). The result of their study is summarized bellow:

(a) If the point group H is either 1 or 1^{-}, no symmetry dictated extremum with respect to any rotation exist.

(b) If the point group H is either 2, m, 2/m, 4, -4, 4/m, 3, -3, 6, -6, or 6/m no symmetry dictated extremum with respect to any symmetry axis (e.g. *z*) exist. But symmetry extremum with respect to *x* and *y* axes will exist.

(c) If the point group H is either one of the 222, 2mm, 422, 2mm, -42m, 4/mmm, 32, 3m, -3m, 622, 6mm, 62m, 6/mmm, 23, m3, 432, -43m, or m3m then symmetry dictated extremum with respect to an arbitrary rotation exists.

It is important to note that the existence of symmetry dictated extermum does not determine whether the extremum is energetically minimum, maximum, or saddle. Therefore, if symmetrical shapes are observed experimentally, the extremum is also

energy minimum and is repeatable. Other observed orientations are accidental and will vary if the experimental conditions are changed.

4.3.1.2 Symmetry of α-Fe nanostructures embedded in $LaSrFeO_4$ matrix

The group theory can be applied in the case of α-Fe nanostructures embedded in $LaSrFeO_4$ matrix. The symmetry point groups for α-Fe nanowires with b.c.c. structure and $LaSrFeO_4$ matrix with tetragonal K_2NiF_4 structure are m3m and 4/mmm, respectively. Therefore, with respect to group theory a heterophase interface between α-Fe and $LaSrFeO_4$ phases should belong to the point group that contains all the point symmetry elements of both the matrix and the second phase. Because the 4/mmm crystallographic group is itself a subgroup of the m3m group, the interface between α-Fe nanostructures and $LaSrFeO_4$ matrix therefore belongs to the 4/mmm symmetry group (Fig.4.8). According to the analysis mentioned above if the interface point group belongs to the 4/mmm group the symmetry dictated extremum with respect to any symmetry axis (e.g. [001]) exist. Therefore, symmetrical shapes are expected (if energetically favorable) and the Baker-Nutting orientations $[001]_{Matrix} \parallel [001]_{\alpha\text{-}Fe}$ and $[110]_{Matrix} \parallel [100]_{\alpha\text{-}Fe}$ hold true. In our experiments with α-Fe nanowires embedded in $LaSrFeO_4$, where the symmetrical square-shaped second phase is observed, this extremum is also an energy minimum which therefore results in the formation of highly symmetrical shapes embedded in the matrix.

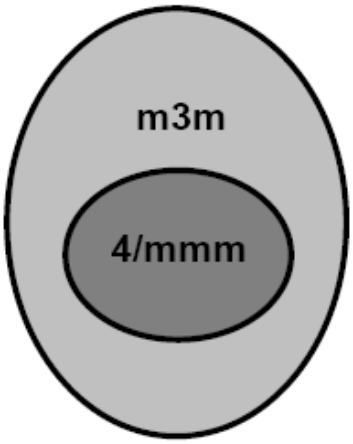

Fig.4.8 Relationship between the crystallographic symmetry group of the matrix belonging to 4/mmm and the iron nanowires belonging to m3m groups. The 4/mmm is a subgroup of the m3m crystallographic group.

4.3.2 Shape evolution of coherent precipitates in elastic media

4.3.2.1 Theoretical calculations

The shape evolution of a coherent second phase embedded in an anisotropic matrix has been theoretically studied by many groups. When the precipitates are densely distributed they interact and align with one another to create stable patterns that coarsen very slowly. When they are widely separated they evolve from spheres to cubes and plates as they grow.

Both the elastic and interfacial energies of a precipitate embedded in a solid matrix depend on the precipitate shape. The energetically favorable shape of a coherent particle is determined by minimizing the sum of the surface and elastic

strain energies and varies with particle size. Depending on the precipitate size, three scenarios are possible where the shape of the second phase is determined by 1) minimization of surface energy alone, 2) minimization of elastic energy alone or 3) a balance between the surface and elastic energies.

The morphology that minimizes the surface energy may be different from that which minimizes the elastic strain energy. Since the ratio of elastic to surface energy is proportional to precipitate size, the second phase possessing minimum energy should tend toward the shape corresponding to the minimum surface energy shape (circle) when the particle is small and the minimum elastic energy (faceted shapes) when the particle is large. As a result, the evolution of the energetically favorable small circular precipitate, which corresponds to minimum surface energy, to more faceted shapes with facets along the elastically soft direction should occur as the size of the precipitate increases in a solid matrix.

Johnson and Cahn have theoretically studied the shape change transitions of elastically misfit precipitate[72]. They show that elastically homogeneous isotropic materials do not exhibit a morphology transition. Precipitates that are relatively harder than the matrix also maintain the same morphology for all precipitate volumes. Softer precipitates display shape changes with increasing volume as elastic energy contributions become more important.

McCormack et al. have studied the morphological evolution of coherent inclusions in elastic media in two dimensions and have calculated the equilibrium size at which a circular inclusion transforms into a square morphology[73]. The result of

their two dimensional study can be equivalent to an infinitely long cylinder with the misfit acting only on the plane perpendicular to the long axis of cylinder.

As mentioned above a complete theory of coarsening for coherent precipitates must consider both the elastic interactions that determine the relative elastic energy of a precipitate configuration and the interfacial energies.

$$E = E_{Interface} + E_{Elastic} \qquad \text{Eq.4.4}$$

The elastic interaction that determines the precipitate shape and alignment is due to the lattice mismatch between the precipitate and the matrix and is strongly affected by elastic anisotropy. Therefore, the elastic energy contribution to the free energy can be explained by a configurational energy that depends on its spatial configuration. If the configuration of the second phase is described by the function θ(r), then the elastic energy is written as:

$$E_{Elastic} = 4E^* A_p I_p[\theta(r)] \qquad \text{Eq.4.5}$$

In this equation E^* is a material constant and is a measure of elastic interaction energy defined as:

$$E^* = -\frac{\beta^2 \Delta\varepsilon^2}{2c_{11}(2c_{11} - \Delta)} \qquad \text{Eq.4.6}$$

where c_{ii} is the elastic constant, $\Delta = c_{11} - c_{12} - 2c_{44}$ is the elastic anisotropy constant, and $\beta = c_{11} + 2c_{12}$ is the bulk modulus for a cubic precipitate. A_p is the cross sectional area of the precipitate second phase in the plane and I_P is a dimensionless function

whose value depends only on the configuration of the second phase in the plane and is defined as:

$$I_p[\theta(r)] = \frac{1}{A_p}\int_k \gamma'(n)|\theta(k)|2\frac{d^2k}{(2\pi)^2} \qquad \text{Eq.4.7}$$

where $\theta(k)$ is the Fourier transform of the shape function $\theta(r)$. It is important to note that if $\Delta < 0$ (negative elastic anisotropy), E^* is positive and therefore minimizing I_P will also minimize the energy.

The configurational surface energy second phase per unit length perpendicular to the plane can be written as:

$$E_{surface} = \sigma\sqrt{A_p}L_p \qquad \text{Eq.4.8}$$

where σ is the isotropic surface tension and L_p is the dimensionless line length of the embedded second phase which only depends on the shape of the precipitate and is independent of its size.

By adding Eq.4.5 and Eq.4.8, the total configurational energy can be written as:

$$\Delta e = \frac{E_{elastic} + E_{surface}}{4E^*A_p} = I_p + \frac{r_0}{D}L_p \qquad \text{Eq.4.9}$$

where

$$r_0 = \frac{\sigma}{4E^*} \qquad \text{Eq.4.10}$$

r_0 is the effective length that measures the relative contribution of the surface and elastic effects and $D = \sqrt{A_p}$ is the length that measures the size of the second phase.

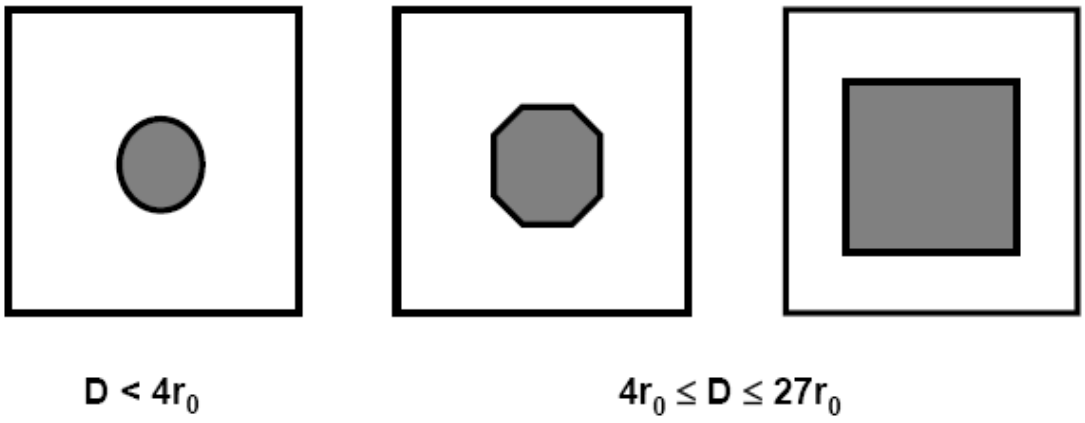

Fig.4.9 The two-dimensional shape transition in a coherent precipitate embedded in an elastic matrix. The circle transforms to a more faceted morphology when the lateral diameter $D > 4r_0$.

The finite element simulation method performed by McCormack et al. shows that the circular shape is stable when the cross-sectional length (D) of the second phase is $D < 4r_0$. Beyond this diameter the circular shape is unstable and the minimum energy path converts it into a more faceted octahedron shape. This reflects the slight anisotropy in the surface tension which creates a preference for specific facets. As shown in Fig.4.9, the octahedrons are unstable with respect to evolution into a square shape. The square shape is achieved by moving material from other facets to the most elastically soft facet by shrinking the latter. The transition from octahedron to square shape happens when $4r_0 < D < 27r_0$.

4.3.2.2 Shape evolution of α-Fe nanostructures embedded in $LaSrFeO_4$ matrix

As shown in Fig.4.7 the in-plane shape of the nanowires also changes as the lateral size of the nanowires increases. The circular shaped nanowires with average diameter of about d = 4nm evolve to octahedral shaped nanowires with only [110] and [100] facets and eventually to nanowires with almost square shaped cross sections consisting mainly of [110] facets. More detailed HRTEM images of the single nanowires and their faceting are shown in Fig.4.10.

It is interesting to estimate the diameter at which the shape evolution of the embedded α-Fe second phase takes place. We have applied the results of the above mentioned theoretical studies by McCormack et al. to the iron nanowires formed by phase decomposition assuming that the principle strain parallel to the long axis of the nanowires is much smaller than that of perpendicular to the long axis (infinitely long cylinder). Considering the values available in the literature for α-Fe (b.c.c.) with elastic anisotropy constants of c_{11} = 222.7, c_{12} = 128.7 and c_{44} = 131.3 GPa[74] we obtain:

$$\Delta = c_{11} - c_{12} - 2c_{44} = -168.6$$

Therefore the negative elastic anisotropy condition ($\Delta < 0$) is satisfied. Knowing the elastic anisotropy constants and calculating the in-plane strain which is equal to the lattice mismatch between α-Fe and $LaSrFeO_4$, ε_{xy} = 0.046, we can obtain E^* from Eq.4.6 as the following:

$$E^* = -\frac{\beta^2 \Delta \varepsilon^2}{2c_{11}(2c_{11} - \Delta)} = \frac{(222.7 + 257.4)^2 \times 168.6 \times 0.046^2}{445.7(445.7 + 168.6)} \cong 0.3 \text{ GPa}$$

The surface energy of b.c.c. α-Fe is equal to σ_s = 2.41 (J/m2)[75] . With respect to these values and the approximation taken into account, from Eq.4.10 the minimization of free energy in self-assembled α-Fe nanowires results in an effective length of:

$$r_0 = \frac{\sigma}{4E^*} = \frac{2.41}{1.2\times10^{-9}} \cong 2 \text{ nm}$$

According to finite element simulation results obtained by McCormack et al.[12], the circular shape is stable when the cross-sectional length (D) of the second phase is $D < 4r_0$. Beyond this diameter the circular nanowires evolve into a more faceted octahedron shape and finally to square shape with elastically soft facets dominating when $4r_0 < D < 27r_0$. In this study, the circular shape is observed when the diameter of the nanowires is between 3 and 6 nm. Theoretically, the circular shape of iron nanowires should evolve to octahedral or square cross-sections approximately when D > 8 nm. This is confirmed in the films grown at T = 740 °C. Here, an octahedral shape α-Fe second phase with an average diameter around d = 16 nm and facets of [110] and [100] is observed. The smallest diameter observed in the films grown at this temperature which shows the same faceting behavior is around 11 nm. Thus the transition from circular to octahedral shapes occurs in the region $6 < d < 11$ nm which is in good agreement with the theoretical value (D = 8 nm) estimated from the McCormack et al. model.

The observation of octahedral shaped nanowires with [110] and [100] facets is due to the anisotropic nature of the surface tension. As the temperature of the deposition and therefore the lateral size of the nanowires increases, square-shaped nanowires are expected to appear with [110] facets, which tends to be the elastically soft direction in b.c.c. structures. In the present case, even at higher growth

temperatures where nanowires of average diameter d = 50 nm are formed, there are some small [100] facets at the corners of the square as shown in Fig.4.10 C.

This is due to the fact that in α-Fe with b.c.c. structure the order of the surface free energy is $\sigma_{110} \leq \sigma_{100} < \sigma_{111}$, and the surface energies of the [100] and [110] facets are very close to each other.[76,77] In some cases the surface energy of the [100] facet is shown to be even slightly higher than [110] facet. The close values of the surface energies for the [100] and [110] facets is attributed to the magnetic energy contribution to the surface energy[78]. In magnetic 3d metals such as Fe, the magnetic energy lowers the surface energy of the more open surface. It is observed that due to lower coordination numbers and thereby increased localization effects, surface magnetic moments are systematically larger at the open surfaces than that of closed packed ones. With respect to this, the anisotropy in the surface energy observed in paramagnetic surfaces, where the most densely packed facets exhibit lowest surface energy, may be reversed if magnetic effects are sufficiently large.

In the present experiments, [110] facets always dominate in square shaped iron nanowires but in most samples there are [100] facets present at the corners of the squares. Therefore, the surface energy of the [110] facet seems to be slightly lower than that of the [100] facet. As was observed in Fig. 4.5, increasing the temperature to above T > 840 °C lead to the transition from a kinetically to a thermodynamically controlled growth mode. Therefore a nucleation site can easily detach from larger nuclei, causing the nuclei to lose stability resulting in smaller lateral size of iron nanowires above this critical temperature.

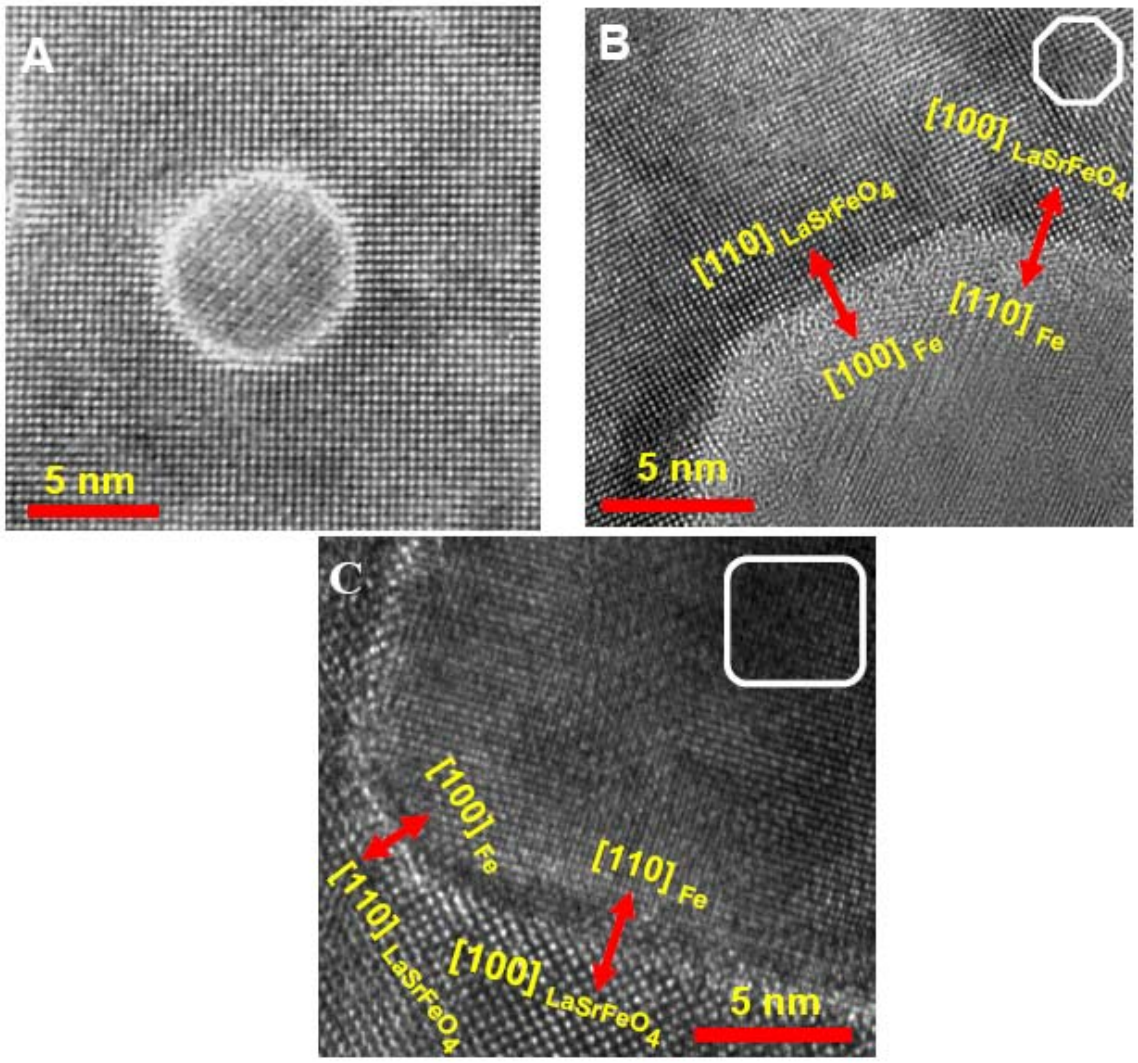

Fig.4.10 Plan view high resolution TEM detail images of A. circular nanowires grown at T = 560 °C, B. a section of the nanowires grown at T = 740 °C showing the interface between a single α-Fe nanowire and $LaSrFeO_4$ matrix, and C. a section of almost square nanowires grown at T = 840 °C showing [110] facets of Fe pillars dominating with small [100] facets observed in the corners.

Chapter 5 Magnetic Properties of Self-Assembled α-Fe Nanowires

5.1 Introduction

In the previous chapters, we introduced the possibility for a new and time effective method to fabricate iron nanowires by means of self-assembly through spontaneous phase decomposition. It was shown that nanowires with various diameters can be simply obtained by changing the growth temperature (substrate temperature). The length of the nanowires can also be changed by varying the deposition time and thus changing the thickness of the film.

Magnetic nanowires may be the basic structural units of future patterned media or microwave devices. The explanation and prediction of hysteresis loops is of great importance in fundamental and applied magnetism. Hence, this chapter focuses on measuring and understanding the magnetic properties of these single crystalline nanowires. The magnetic properties of the self-assembled nanopillars are compared to the iron nanowires electrodeposited into the alumina template and the similarity and the differences are discussed. In Table 5.1 some of the observed properties for electrodeposited iron nanowires are listed. It is shown that almost square-shaped hysteresis loops are obtained for optimum aspect ratios, when the direction of the magnetic field is parallel to the long axis of the nanowire. The essential role of shape anisotropy, as opposed to magnetocrystalline anisotropy in analyzing the magnetic properties, is discussed.

It is also demonstrated that by changing the diameter and the length of the nanowires (by the above mentioned methods) and therefore modifying their aspect ratio, we can easily alter and tailor their magnetic behavior for various applications. Magnetic force microscopy (MFM) along with atomic force microscopy (AFM) are used to compare the magnetic phases, the domain structure and the topography of the samples containing nanowires with various diameters.

Additionally, in accordance with the proposed nanosize microwave oscillator based on spin torque and phase locking, primary results of ferromagnetic resonance (FMR) measurements on iron nanowires are discussed.

	Fe Nanowires	Unit
M_s	1707	emu cm^{-3}
$\delta_0 = \delta_W/\pi$	13	nm
d_{coh}	11	nm
$2\pi Ms$	10730	Oe
H_A	10000	Oe
$H_C(RT)$	3000	Oe
M_r/M_s	0.93	----

Table 5.1 The properties of the electrodeposited Fe nanowires at room temperature.

5.2 Theoretical framework for nanomagnets

The local magnetism *M* of a magnetic body is determined by the magnetic free energy *F(M)*. The magnetization is obtained by drawing the minima of *F* as a function of the external magnetic field (*H*). The corresponding magnetization state in a free-energy minimum is the origin of the magnetic hysteresis. By switching off an adequately large magnetic field, the magnetization approaches a remanence $M_r > 0$ and reducing the volume-averaged magnetization to $M = 0$ will require a reverse field known as the coercivity H_C. The magnetic free energy consists of four main terms:

$$F = F_{ex} + F_K + F_{ms} + F_H \qquad \text{Eq.5.1}$$

The F_{ex} contribution to the free energy is:

$$F_{ex} = \int A[(\nabla m_x)^2 + (\nabla m_y)^2 + (\nabla m_z)^2]dV \qquad \text{Eq.5.2}$$

where *A* denotes the exchange stiffness and $m = M/M_s$ is the reduced magnetization. The contribution of F_K, uniaxial anisotropy, to Eq.5.1 is defined as:

$$F_K = K_u V \sin^2\theta \qquad \text{Eq.5.3}$$

where K_u is the first anisotropy constant and θ is the angle between *M* and the easy axis of the magnetization. The magnetostatic self-interaction energy for an ellipsoidal magnetic body magnetized along a principle axis can be determined as:

$$F_{ms} = \frac{1}{2} N M_s^2 \qquad \text{Eq.5.4}$$

where *N* is the demagnetizing factor. When the principle axis of an ellipsoid is parallel to the easy axis Eq.5.4 can be written as a uniaxial anisotropy and is then called shape anisotropy. The last term in Eq.5.1, described by the *Zeeman* term, is

related to magnetostatic interaction of the magnet with the external magnetic field as below:

$$F_H = -HM_sV\cos\varphi \qquad \text{Eq.5.5}$$

The equations above are based on the Stoner-Wohlfarth (SW) model which is the simplest model for nanomagnets[79]. Accordingly, when the field is applied along the easy axis of a coherent magnet, the hysteresis loop is rectangular and H_C is equal to the anisotropy field as follows:

$$H_A = \frac{2K_u}{M_s} \qquad \text{Eq.5.6}$$

Applying the field perpendicular to the easy axis will result in a straight line which reaches the saturation magnetization M_s at a magnetic field equal to H_A. When the field direction is between these two cases the $H_C < H_A$. If a magnet is considered an assembly of randomly oriented SW pieces then by averaging over all directions in the space, the hysteresis loop with $M_r = 0.5M_s$ and $H_C = 0.48H_A$ is obtained.

In the real case, the magnetic nanomaterial is more complicated than an assembly of SW pieces. The interaction between a few magnetic particles may lead to complex cooperative interparticle effects. In addition, if the nanomagnet is large enough, the magnetization configuration can become incoherent. Therefore, Eq.5.1 can greatly overestimate the coercivity of the real magnets. Magnetic domains separated by domain walls with thickness of δ_w are an example of incoherent magnetization state. Therefore, δ_w is the width of the transition between the uniformly magnetized states of two domains. The formation of the domains requires some

domain wall energy and therefore, equilibrium domains are formed when the diameter of the nanomagnets exceeds the critical size D_c. δ_w and D_c are given by:

$$\delta_w = \pi\sqrt{\frac{A}{K_u}} \qquad \text{Eq.5.7}$$

and

$$D_c = \frac{18\sqrt{AK_u}}{\pi M_s^2} \qquad \text{Eq.5.8}$$

As a result, the domain wall thickness is determined by the counterbalance between the exchange energy (which tends to increase it) and the anisotropy energy (which tends to diminish it). For iron the domain wall thickness is around δ_w (Fe) = 40 nm. When magnetic nanoparticles are coupled together by exchange to form a magnetic cluster, the domain walls sometimes also include the boundaries between these clusters and are called interaction domains. The formation of equilibrium domains should be differentiated from the incoherent magnetization state occurring during magnetization reversal. The magnetization reversal starts with a nucleation instability of the remanent state. In small nanoparticles and thin nanowires the reversal is uniform but in macroscopic ellipsoids it is incoherent[80]. In a perfect wire, the transition from coherent to incoherent nucleation occurs at a coherent diameter of d_{coh} = 7.31l_{ex} where the exchange length, l_{ex}, is defined as below:

$$l_{ex} = \sqrt{A \big/ 4\pi M_s^2} \qquad \text{Eq.5.9}$$

For Fe, Co and Ni, the coherence diameter are about d_{coh} = 11, 15 and 25 nm, respectively.

The interaction mentioned above is closely related to the demagnetizing field. The demagnetizing field $H_d = -NM$ is often interpreted as an internal-field correction derived from Maxwell's equations. For ideal infinite films, $N = 0$ and $H_d = 0$ when the magnetization is parallel to the film plane, but $N = 4\pi$ and $H_d = -4\pi M$ for perpendicular (out-of-plane) magnetization.

The hysteresis of a magnet is also strongly affected by imperfections. The imperfections may reduce the free-energy barriers associated with the beginning of magnetic reversal (nucleation). Alternatively, defects may inhibit the motion of domains and create domain pinning. Therefore, a widely used expression for the coercivity, H_C, is[81]:

$$H_C = \alpha \frac{2K_u}{M_s} - N_{eff} M_s \qquad \text{Eq.5.10}$$

Here, α is a parameter that depends on grain orientation and reversal mechanism and N_{eff} is the effective demagnetization factor. This will lead to H_C values of around 20-30% of H_A, which is generally observed experimentally.

The discussion above is based on the minimization of the free energy and ignores the destabilizing effect caused by the thermal fluctuations. By combining Eq.5.1 to Eq.5.5 for aligned and non–interacting SW magnetic bodies the free energy barrier can be defined as:

$$F_B(H) = K_u V (1 - \frac{H}{H_A})^m \qquad \text{Eq.5.11}$$

where K_u includes the body's shape anisotropy. Eq.5.11 shows that the free energy barrier decreases with the nanomagnet's size. When $K_u V$ is comparable to $K_B T$ the magnetism decays very rapidly. This is known as superparamagnetism. Defining

superparamagnetism as the time necessary to jump over a free energy barrier of τ = 100 sec leads to the stability condition of $\frac{K_u V}{K_B T} \geq 25$ where $\frac{K_u V}{K_B T} \geq \xi$ is referred to as the stability parameter. For a magnetic body to be stable for 10 years, the stability parameter should be $\xi \geq 40$.

5.3 Magnetic properties of self-assembled nanowires

The magnetization loops for the iron nanowires were measured using Superconducting Quantum Interface Device (SQUID) magnetometry. Fig.5.1 compares the room temperature magnetization data of the films grown in vacuum with those grown in 200 mTorr of oxygen at T = 760 ºC. While no net magnetic moment exists in the film grown in oxygen (as expected for the antiferromagnetic $La_{0.5}Sr_{0.5}FeO_3$ perovskite phase), a very strong magnetic moment is observed for self-assembled iron nanowires (the film grown in vacuum). The magnetization value normalized to the average α-Fe volume fraction of 10.95% obtained from Mössbauer spectra is about 1600 emu/cm^3, which is fairly close to the magnetization of bulk iron (1700 emu/cm^3). The 6% difference could possibly be attributed to surface spins and/or the error in the estimation of volume fraction used for normalization.

For the self-assembled nanowires the hysteresis loops are measured with magnetic field applied parallel to the film plane along the [100] direction (in-plane) and perpendicular to the film plane along the [001] direction (out-of-plane). The films contain iron nanowires of 20 nm diameter and 200 nm length. As shown in Fig.5.1 a

remanence of M_r = 0.95 M_s and coercivity of H_C = 3400 Oe is observed for out-of-plane hysteresis loop. In contrast the loop along [100] is almost a straight line. These magnetic measurements reveal a strong out-of-plane magnetic anisotropy, with the easy axis along the long axis of the nanowires. The anisotropy field of $H_A \approx$ 10000 Oe is obtained from the magnetization measurements along the easy (out-of-plane) and the hard (in-plane) axes, as illustrated in Fig.5.1. As observed here the coercivity is close to 30% of the anisotropy field as was predicted by Eq.5.10.

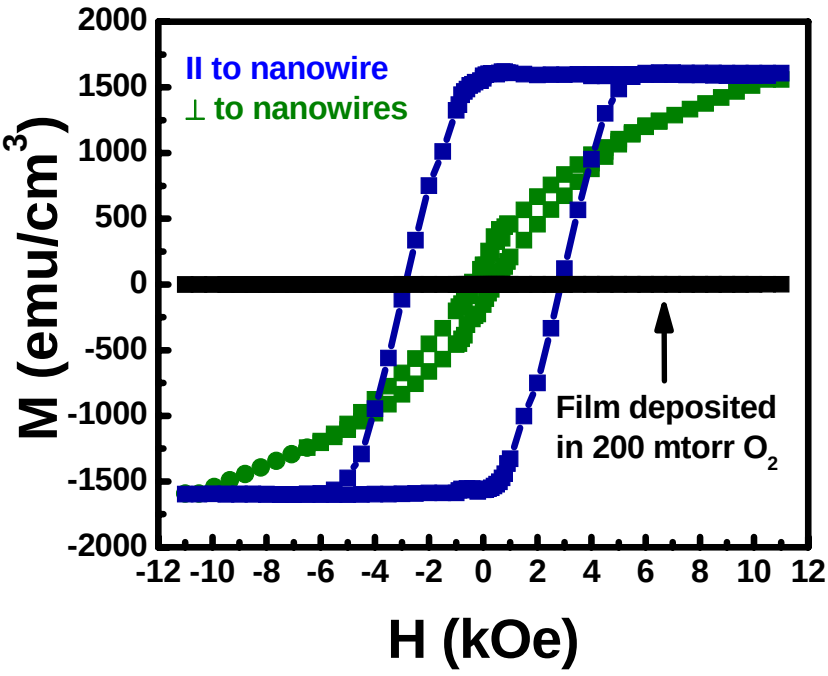

Fig.5.1. Room temperature magnetic properties of α-Fe nanowires. Comparison of the magnetization of an antiferromagnetic $La_{0.5}Sr_{0.5}FeO_{3-x}$ epitaxial film grown in 200 mTorr O_2 (black) and of a film grown in vacuum at T = 760 ºC. Out-of-plane [001] (blue) and in-plane [100] (green) magnetic hysteresis loops correspond to α-Fe nanowires and indicates strong anisotropy.

There are three factors contributing to the magnetic anisotropy: 1) magnetocrystalline anisotropy which is the dependence of the magnetic properties on the crystallographic direction; 2) shape anisotropy which is a measure of the difference in the energies associated with the magnetization in the shortest and longest dimensions; and 3) stress induced anisotropy which is due to the rotational changes in the magnetization due to the changes in dimensions. The magnetoelastic effects induced by strain depend on the magnetostriction coefficient $\lambda = \Delta l/l$.

For the cubic self-assembled iron nanowires, no magnetocrystalline anisotropy is expected between the two experimentally measured crystallographic directions of [001] (out-of-plane) and [100] (in-plane). The magnetostriction coefficient λ_{100} value for b.c.c. iron is 20.7×10^{-6}. The stress in Fe nanowires is given by $\sigma_{001} = Y\ \varepsilon_{001}$ in which Y is the Young modulus ($Y_{Fe} \approx 10^{11}$ Pa) and ε_{001} is experimentally obtained along the [001] direction. The magnetoelastic energy associated with this stress is:

$$e = -3\lambda_{001}\sigma_{001}/2 \qquad \text{Eq.5.11}$$

which by taking into account the above mentioned values will result in $e = 14.28\times10^4$ erg/cm^3. The anisotropy field is given by

$$H_{Stress} = 2e/M_s \qquad \text{Eq.5.12}$$

This will result in an anisotropy field contribution of $H_{stress} = 167$ Oe. Therefore, the magnetoelastic effect on anisotropy is almost negligible in self-assembled iron nanowires.

The shape anisotropy for the nanowires can be calculated by estimating a thin cylinder with an observed aspect ratio of $l/d \cong 10$ where the anisotropy factor N_z = 0.0172 [82]. The associated anisotropy energy for the above mentioned cylinder is:

$$E_{Shape} = 2\pi(N_x - N_z)M_s^2 \qquad \text{Eq.5.13}$$

where $N_x = (1 - N_z)/2$. The measured saturation magnetization of M_s = 1600 emu/cm^3 yields an anisotropy field of H_{shape} = 9535 Oe, which is in good agreement with the experimental value obtained. Therefore, these results indicate that the anisotropy observed in the in-plane and out-of-plane hysteresis loops due to the cylindrical shape of the nanowires.

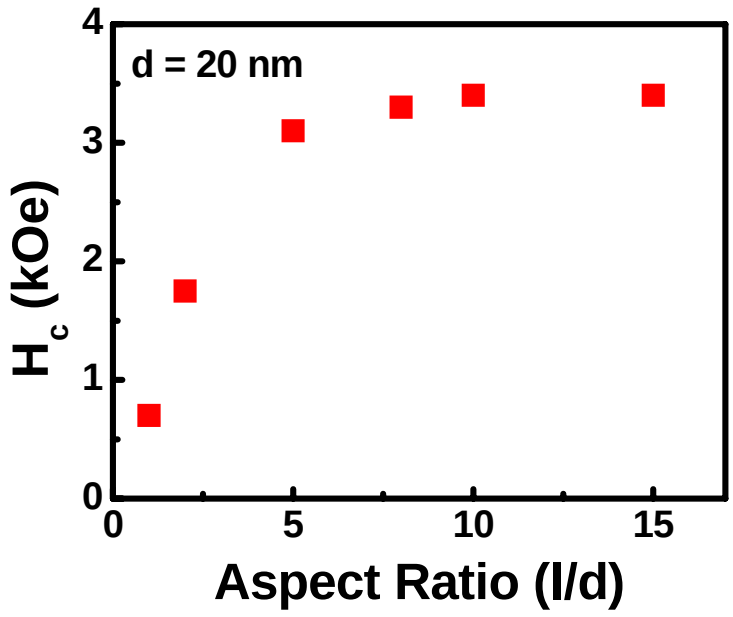

Fig.5.2 Coercivity vs. aspect ratio (r) for the α-Fe nanowires with lateral dimension of $d \cong 20$ nm.

Fig.5.2 shows the dependence of the room temperature coercivity (obtained from out-of-plane hysteresis loops) on the aspect ratio. The average diameter of the nanowires was kept constant at d = 20 nm and the length of the wires was changed so that different aspect ratios were obtained. A gradual increase of the coercivity is observed with increasing aspect ratio, but there is little change when $l/d > 10$. This is consistent with the result observed for iron nanowires, which were electrodeposited in porous alumite films[83].

As mentioned before the SW model fails to explain hysteresis and coercivity of the nanowires. This failure is due to the fact that in this model the magnetic reversal is delocalized, meaning it extends throughout the wire. Although localized reversal is inhomogeneous and therefore unfavorable from an interatomic exchange point of view, near defects and imperfections inside the wire may be favorable as it locally reduces anisotropy. The reason for the localization in single crystalline wire can be due to small magnetization perturbances associated with wire thickness fluctuation, crystalline defects and impurities and geometrical features at wire ends. The electron-localization analogy says that a random weak inhomogenity leads to a localization of the nucleation mode in one dimension. In other words, due to magnetic impurities or defects a small part of the wire is slightly softer than the remaining parts. The localization length is strongly dependent on the structure of the nanowires.

It is shown that localization reduces coercivity and the experimentally obtained coercivities are smaller than the predicted $H_C = 2K_1 / \mu_0 M_s$. The magnetization reversal in real magnets is usually associated with nonlinear dependence of E on H. The corresponding finite-temperature coercivity is:

$$H_C = H_0\left(1-\sqrt{K_B T \ln(\Gamma_0 t)/V_0 K}\right) \qquad \text{Eq.5.14}$$

where the factor $K_B T \ln(\Gamma_0 t)$ is of the order of $25K_B T$. Therefore the coercivity is inversely dependant on the square root of the nanowire length, and the slope of coercivity versus nanowire length will decrease as the length of the nanowires increases. With the increase in the length of the nanowires $H_C \approx H_0$ and therefore the difference between experimental data and SW theory diminishes.

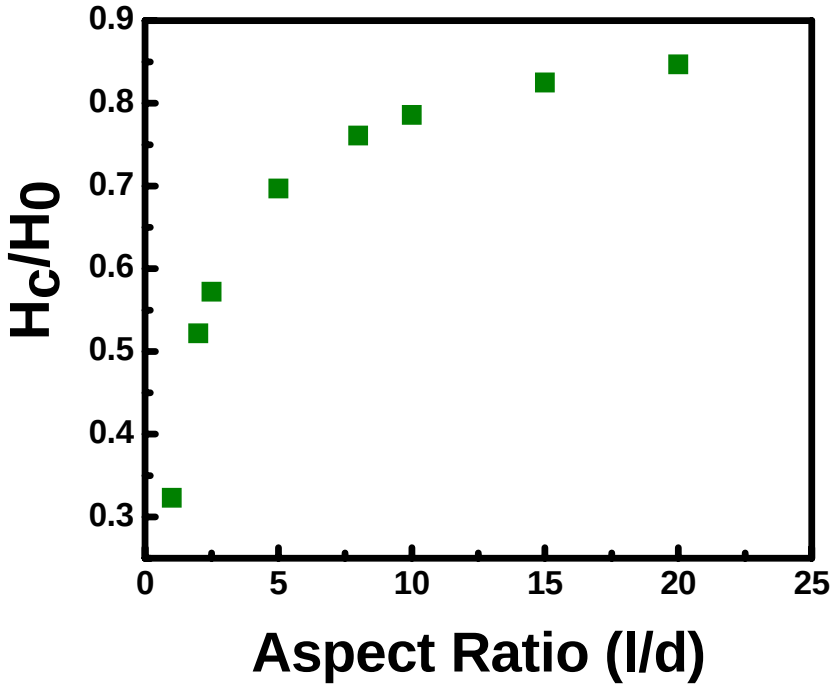

Fig.5.3 Theoretical calculation for H_c/H_0 vs. aspect ratio (r) for the α-Fe nanowires with lateral dimension of $d \cong 20$ nm and lengths $l = 20$ to 400 nm.

Applying Eq.5.14 to iron nanowires with diameter of d = 20 nm, anisotropy constant of $K \approx 3.6\times10^5$ erg/cm^3, where $K_B = 1.3807 \times10^{-16}$ erg/K^{-1} and T = 300 K, we obtain:

$$H_C \approx H_0(1-5\sqrt{0.366/l}) \qquad \text{Eq.5.15}$$

where l is the length of the nanowires in nm. Fig.5.3 shows the plot of H_c/H_0 versus aspect ratio (r) for the α-Fe nanowires with lateral dimension of $d \cong 20$ nm and lengths l = 20 to 400 nm. The plot illustrates that the theoretical calculations are consistent with the experimental data obtained (Fig.5.2) below a knee length (l_{knee}). Beyond l_{knee} while the experimental data almost saturates or changes very little, the theoretical plot (Fig.5.3) increases with a small slope. This slight difference between the experimental and theoretical coercivity of the nanowires can be due to the fact that very long nanowires have finite-size behavior of the bulk and thin film magnets[84]. Therefore, these longer nanowires are more likely to contain pronounced inhomogenities which will reduce the coercivity as discussed before.

Fig.5.4 shows the variation of the coercivity with the diameter which is obtained by growing samples at different temperatures. The length of the nanowires was kept constant at l = 200 nm. As shown in this plot, for the nanowires with a fixed length, the coercivity increases and reaches a maximum and then drops gradually as the diameter of the nanowires increases.

To investigate this observation in more detail, hysteresis loops of iron nanopillars with average diameters of d = 50, 16 and 4 nm are obtained at three different temperatures of T = 5, 100 and 300 K. The hysteresis loops at these temperatures are shown in Fig.5.5, Fig.5.6 and Fig.5.7 for the samples with average diameter of d = 50, 16 and 4 nm, respectively. The data shows that the magnetic

moment decreases as the diameter of the nanowires reduces. This reduction in saturation magnetization might be partly due to the slight variation in the thickness of

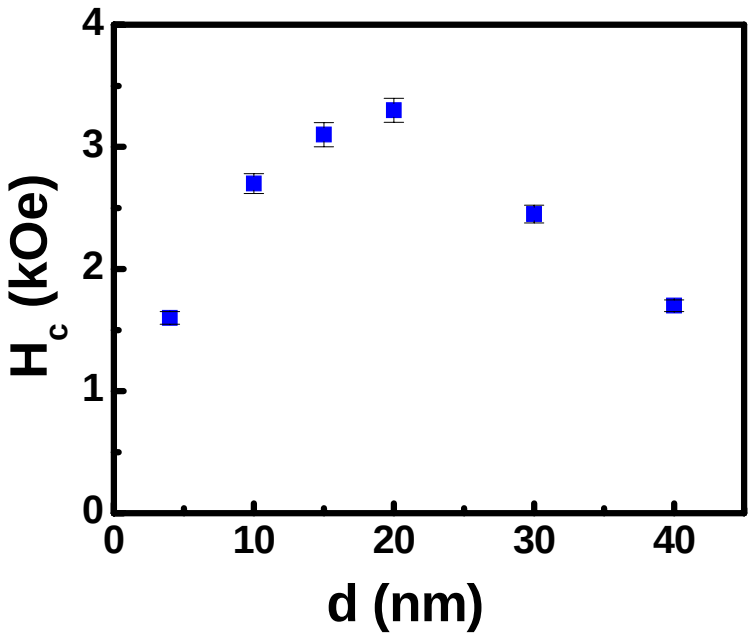

Fig 5.4 The coercivity vs. diameter for the samples grown in different temperatures. The length of the all nanowires is around l = 200 nm.

the different samples, which is unavoidable in the PLD system as the laser energy to some extent varies on a day to day basis. Although the variation in the thickness should be taken into account, most probable reason for this reduction in magnetic moment is the fact that the magnetic properties of iron nanowires with larger diameters are closer to that of the bulk α-Fe. In addition, from these Figures it is clear that the difference between the hysteresis loops obtained at different temperatures

becomes more evident as the diameter of the nanowires reduces, which provides more proof of the fact that iron nanowires with larger diameters have bulk like properties. For better analysis the in-plane and out-of-plane coercivity and remanent magnetization results obtained from these hysteresis loops are summarized in Table 5.2. From this data it is clear that the in-plane coercivity and remanence remain mainly constant for the hysteresis loops measured at all three temperatures, while the out-of- plane coercvity and remanence increase when the hysteresis loops are obtained at lower temperatures. This enhancement in out-of-plane coercivity and remanence is more pronounced as the nanowire diameter becomes smaller. While the remanent magnetization increases only from M_r = 65.4 % (T = 300 K) to M_r = 67.2 % (T = 5 K) and from M_r = 90.6% (T = 300 K) to M_r = 91.4 % (T = 5 K) for the samples with iron lateral diameter of d = 50 and 16 nm, respectively, it rises from M_r = 32.9 % (T = 300 K) to M_r = 53 % (T = 5 K) for the nanowires with diameter of d = 4 nm.

In Fig.5.8 the changes in coercivity as a function of wire diameter measured at three different temperatures, are plotted. The result clearly shows that the change in the coercivity for the samples deposited at T = 560 °C with average diameter of d = 4 nm is more obvious compared to the samples with average diameter of d = 50 nm where the coercivity increases only approximately 140 Oe for the hysteresis loop measured at T = 5 K.

Therefore, all the results indicate that when the nanowires are long enough (above l_{knee} in Fig.5.2), for a fixed length, as the diameter of the nanowires increases, a pronounced maximum in the coercivity and squareness of the relevant hysteresis

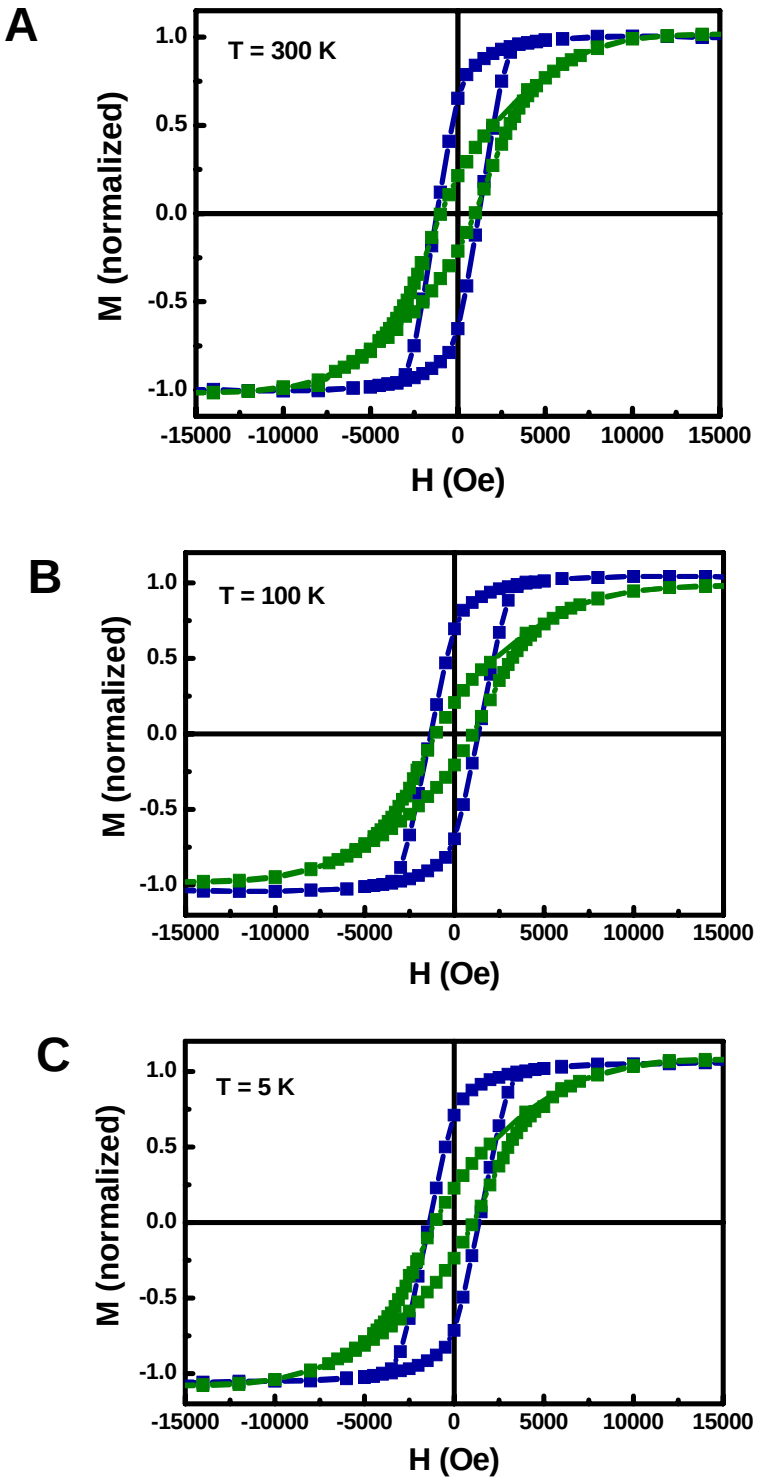

Fig.5.5 Hysteresis loops for the iron nanowires with diameter of d = 50 nm (deposited at T = 840 °C) measured at temperatures of A. T = 300 K, B. T = 100 K, and C. T = 5 K.

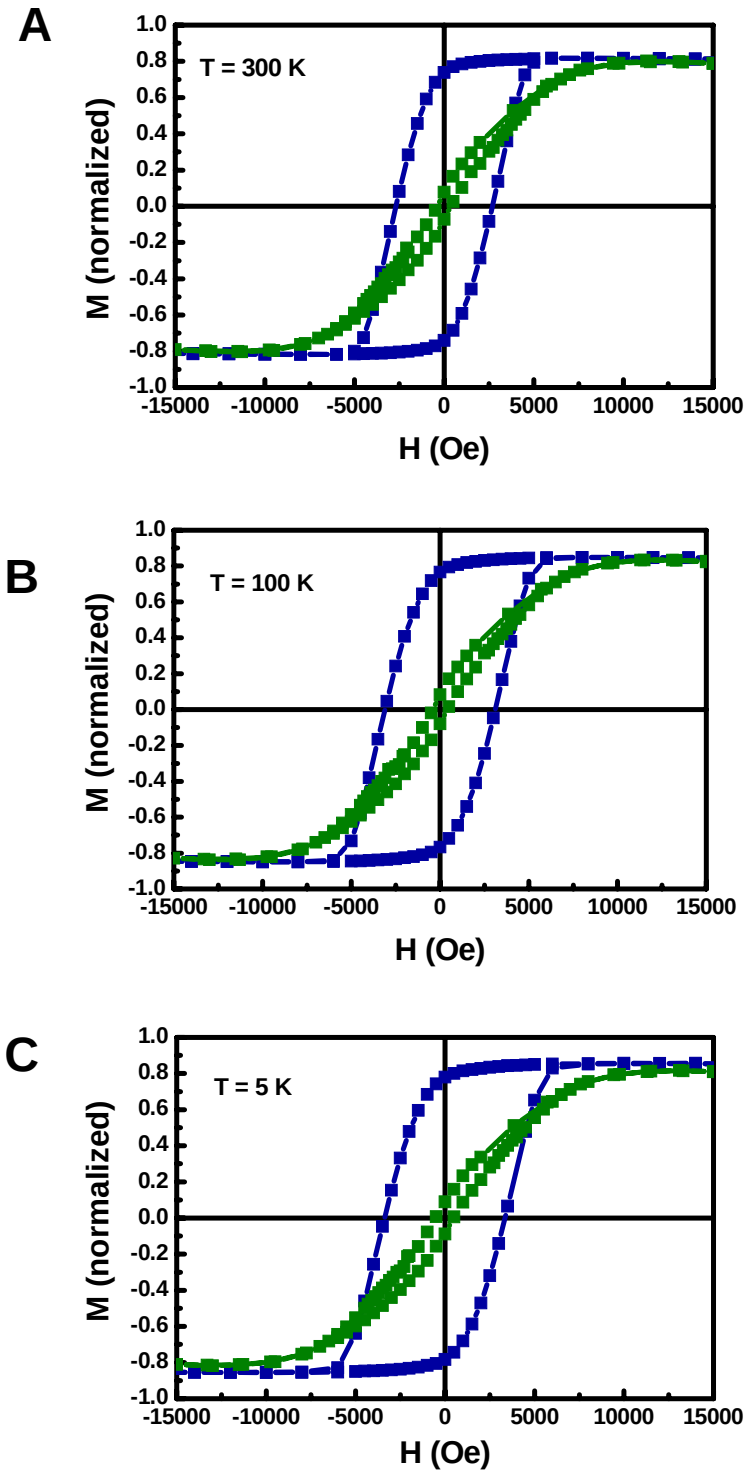

Fig.5.6 Hysteresis loops for the iron nanowires with diameter of d = 16 nm (deposited at T = 740 °C) measured at temperatures of A. T = 300 K, B. T = 100 K, and C. T = 5 K.

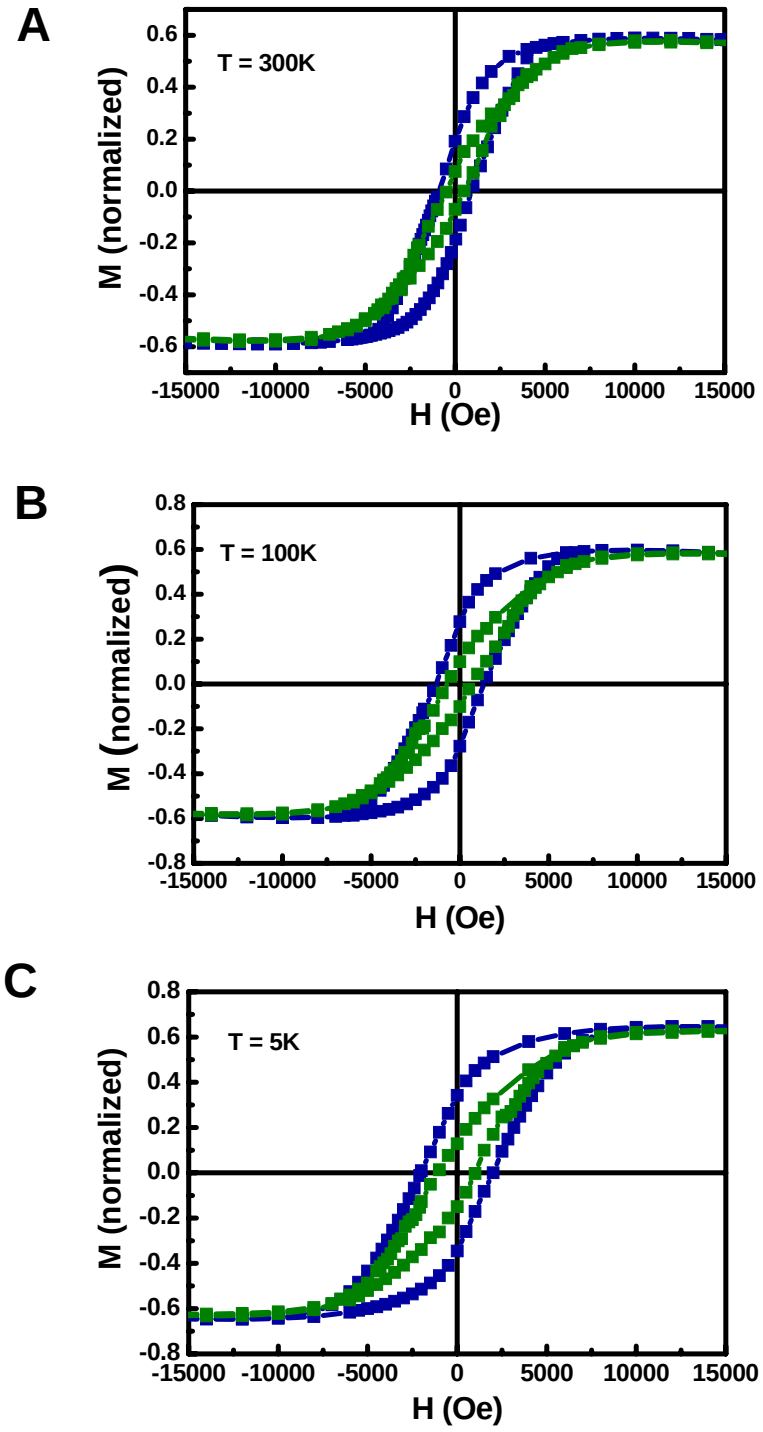

Fig.5.7 Hysteresis loops for the iron nanowires with diameter of d = 4 nm (deposited at T = 560 °C) measured at temperatures of A. T = 300 K, B. T = 100 K, and C. T = 5 K.

A	d_{avg} = 50 nm			
	Out-of-Plane		In-Plane	
T (K)	H_C (Oe)	M_r/M_s	H_C (Oe)	M_r/M_s
300	1240	0.654	1000	0.21
100	1320	0.667	1000	0.214
5	1380	0.672	1000	0.213

B	d_{avg} = 16 nm			
	Out-of-Plane		In-Plane	
T (K)	H_C (Oe)	M_r/M_s	H_C (Oe)	M_r/M_s
300	2700	0.906	500	0.10
100	3100	0.909	500	0.10
5	3350	0.914	500	0.10

C	d_{avg} = 4 nm			
	Out-of-Plane		In-Plane	
T (K)	H_C (Oe)	M_r/M_s	H_C (Oe)	M_r/M_s
300	1000	0.329	500	0.17
100	1320	0.47	500	0.17
5	2000	0.53	500	0.20

Table 5.2 In-plane and out-of-plane coercivity and remanence measured at T = 300, 100 and 5 K for the samples with diameter of A. d = 50 nm, B. d = 16 nm, and C. d = 4 nm.

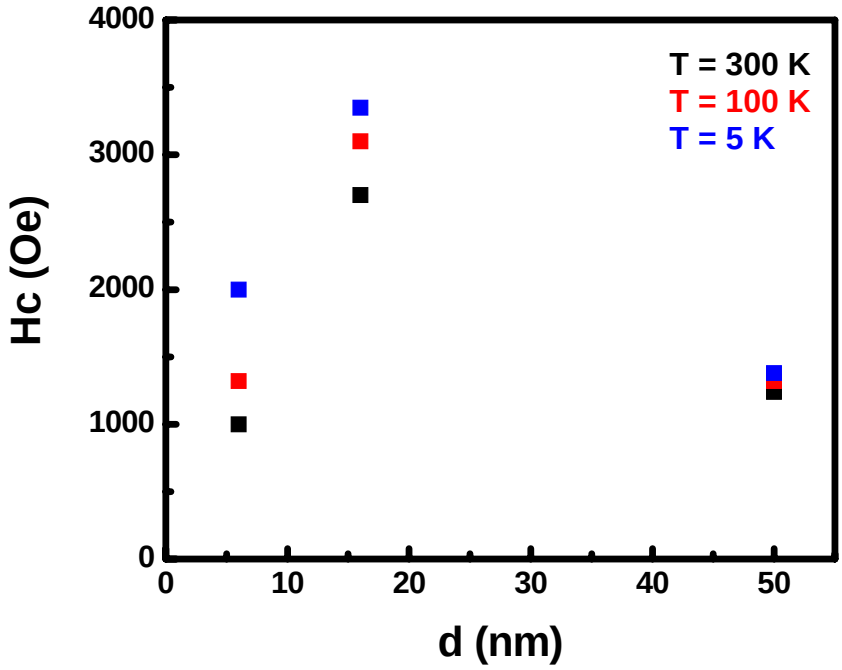

Fig.5.8 Comparison of the coercivities obtained from the hysteresis loops measured at different temperatures of T = 300, 100 and 5 K.

loop exists. For the nanowires with larger diameters the coercivity and remanent magnetization decrease as the aspect ratio (l/d) reduces and the shape of the nanopillars can no longer be considered and modeled as an infinitely long cylinder. For the samples with small diameters, although the aspect ratio increases, the superparamagnetic effects begin to dominate. This is evident in the data obtained from Fig.5.7 and Fig.5.8 in which a pronounced enhancement in the coercivity and squareness of the out-of-plane hysteresis loop of the nanowires with small diameter takes place when the measurements are performed at low temperatures (e.g. T = 100 and 5 K).

5.4 Magnetic force microscopy of iron nanowires

Now that the magnetic behavior of the nanowires and the dependence of the coercivity and remanent magnetization on the diameter, length and therefore, the aspect ratio of the nanowires are discussed, magnetic force microscopy (MFM) is used to simultaneously look at the magnetic phase and topography of the nanowires. Fig. 5.9 shows the MFM images of the nanowires grown at T = 760 °C.

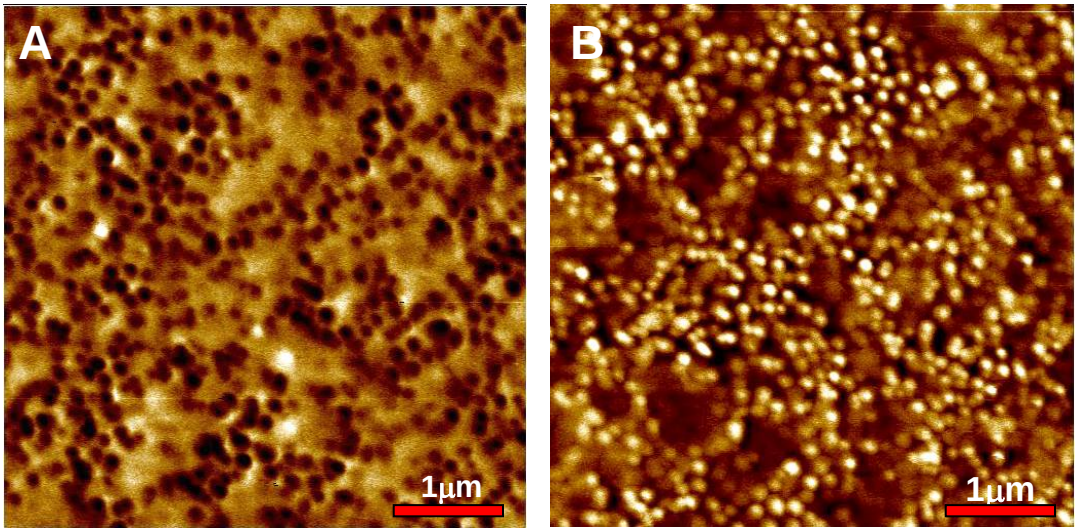

Fig.5.9 MFM images taken from the samples grown at T = 760 °C with a thickness of around l = 200 nm. The samples were magnetically poled at H = 2 T along (A) $[00\bar{1}]$ and (B) [001] direction.

Before imaging, a magnetic field of H = 2 Tesla is applied and the samples are magnetized out-of-plane such that the direction of the field is pointing either toward

the substrate, in the [$00\bar{1}$] direction (Fig.5.9 A) or out of the substrate, in the [001] direction (Fig.5.9 B). The images were taken from a 5 μm × 5 μm area. In these images the dark-colored areas correspond to the attraction between the nanopillars and the tip, whereas white-colored areas correspond to the repulsion between them. Switching of the magnetization was clearly observed in the MFM images. Since the sample was measured in the remanent state, the magnetization was relaxed in some pillars after removal of the magnetic field or during the measurement. Thus, some of the nanowires are in the opposite magnetization state (white contrast in MFM image in Fig.5.9 A and black contrast in MFM image in Fig.5.9 B).

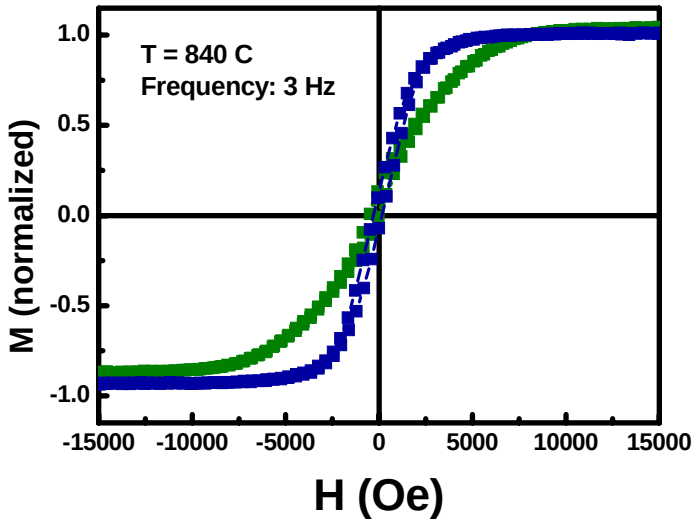

Fig.5.10 Hysteresis loop of the nanowires grown at T = 840 °C with growth rate of 3 Hz.

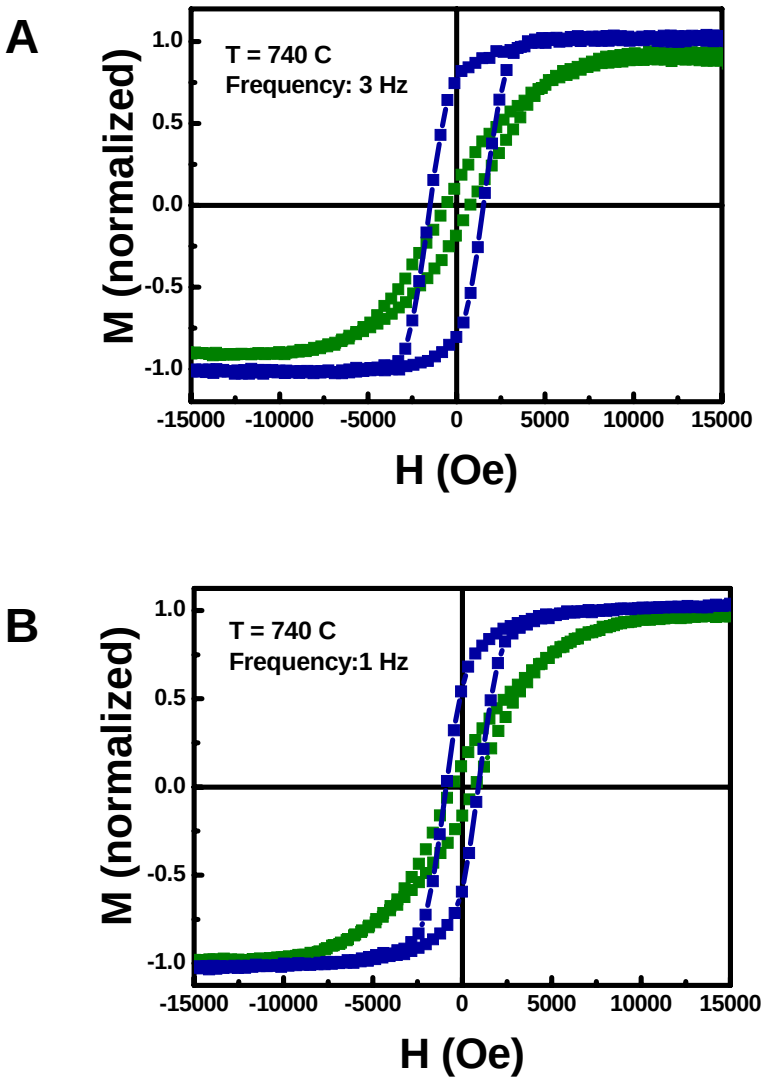

Fig.5.11 Hysteresis loop of the nanowires grown at T = 740 °C with growth rate of A. 3 Hz, and B. 1 Hz.

MFM images along with the measured hysteresis loops provide us with a powerful tool in understanding and studying the effect of changing the growth parameters on these nanowires. Combining the data obtained from hysteresis loops and MFM

images, valuable information about the nanowires' lateral size and therefore kinetics and thermodynamics of the growth can be obtained without the need to perform TEM analysis. The effect of the change in the growth temperature (and therefore the lateral dimensions of the nanowires) in the hysteresis loop were discussed above. Below, the effect of the growth rate on the structure and magnetic properties of the iron nanowires is analyzed using MFM images and hysteresis loops.

The hysteresis loop of the self-assembled iron nanowires deposited at T = 840 °C with growth rate of 3 Hz is shown in Fig.5.10. In comparison with Fig.5.5 A, the out-of-plane coercivity and remanence have dropped from H_C = 1240 Oe and M_r = 65.4 % to H_C = 200 Oe and M_r = 10 %, respectively.

The same experiments were performed on the samples grown at T = 740 °C and T = 560 °C, where as mentioned before, the average diameter of the nanowires is d_{avg} = 16 and 4 nm (at the growth rate of 8 Hz), respectively. The growth rate of 3 and 1 Hz was chosen and the results were compared with samples grown at the frequency of 8 Hz in Fig.5.6 and Fig.5.7. For the samples grown at T = 840 °C, the growth at frequency of 1 Hz was avoided to protect the heater from possible damage resulting from staying at high temperatures for a long period of time.

Fig.5.11 and Fig.5.12 show the hysteresis loops of the nanowires deposited at T = 740 and T = 560 °C, respectively. As observed in Fig.5.11, for the samples grown at T = 740 °C the out-of-plane coercivity and remanent magnetization drops systematically as the growth rate decreases from 8 to 1 Hz. Table 5.3 compares the out-of-plane coercivity and remanent magnetization values for the samples grown at T = 740 °C. In contrast, as shown in Fig.5.12, the out-of-plane coercivity and

remanent magnetization and therefore, the squareness of the hysteresis loop of the self-assembled iron nanowires, increases as the growth rate decreases for the samples grown at T = 560 °C. In Table 5.4, the out-of-plane coercivity and remanent magnetization of these nanowires are summarized.

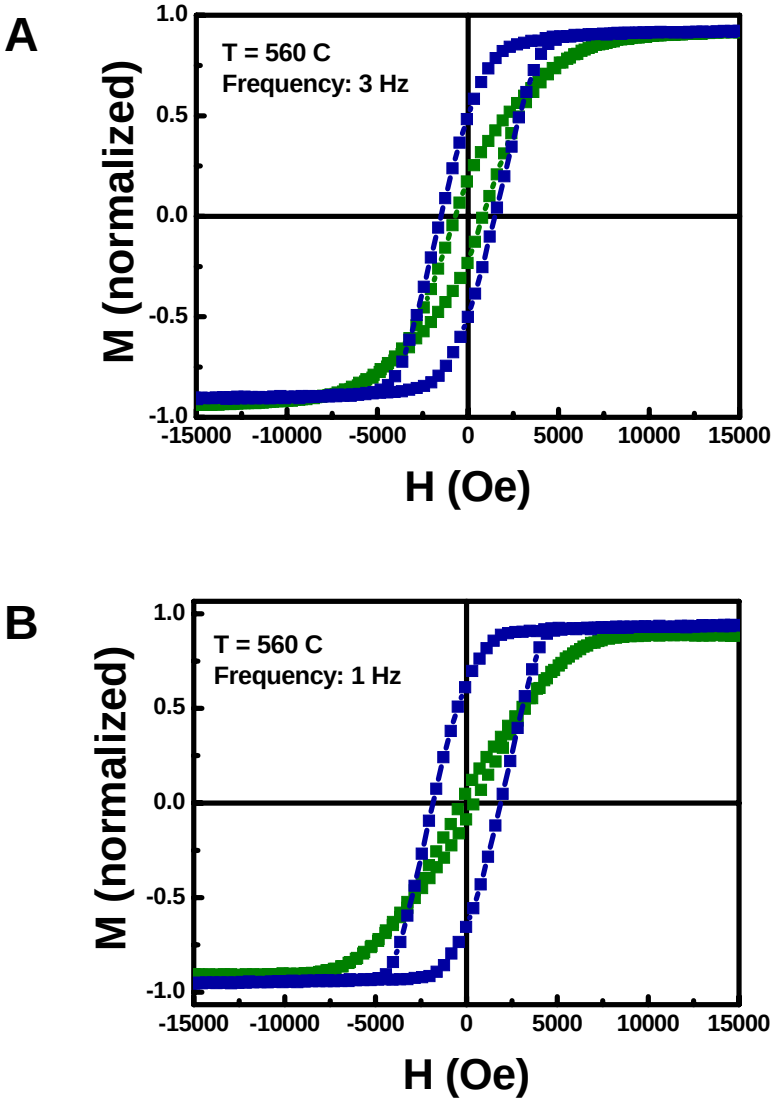

Fig.5.12 Hysteresis loop of the nanowires grown at T = 560 °C with growth rate of A. 3 Hz, and B. 1 Hz.

T_{growth} = 740 °C		
Growth Rate (Hz)	H_C (Oe)	M_r / M_s
8	2700	0.906
3	1500	0.75
1	950	0.57

Table 5.3 Comparison of the out-of-plane coercivity and remanent magnetization of the samples grown at T = 740 °C with different growth rates.

T_{growth} = 560 °C		
Growth Rate (Hz)	H_C (Oe)	M_r / M_s
8	1000	0.329
3	1620	0.50
1	1850	0.68

Table 5.4 Comparison of the out-of-plane coercivity and remanent magnetization of the samples grown at T = 560 °C with different growth rates.

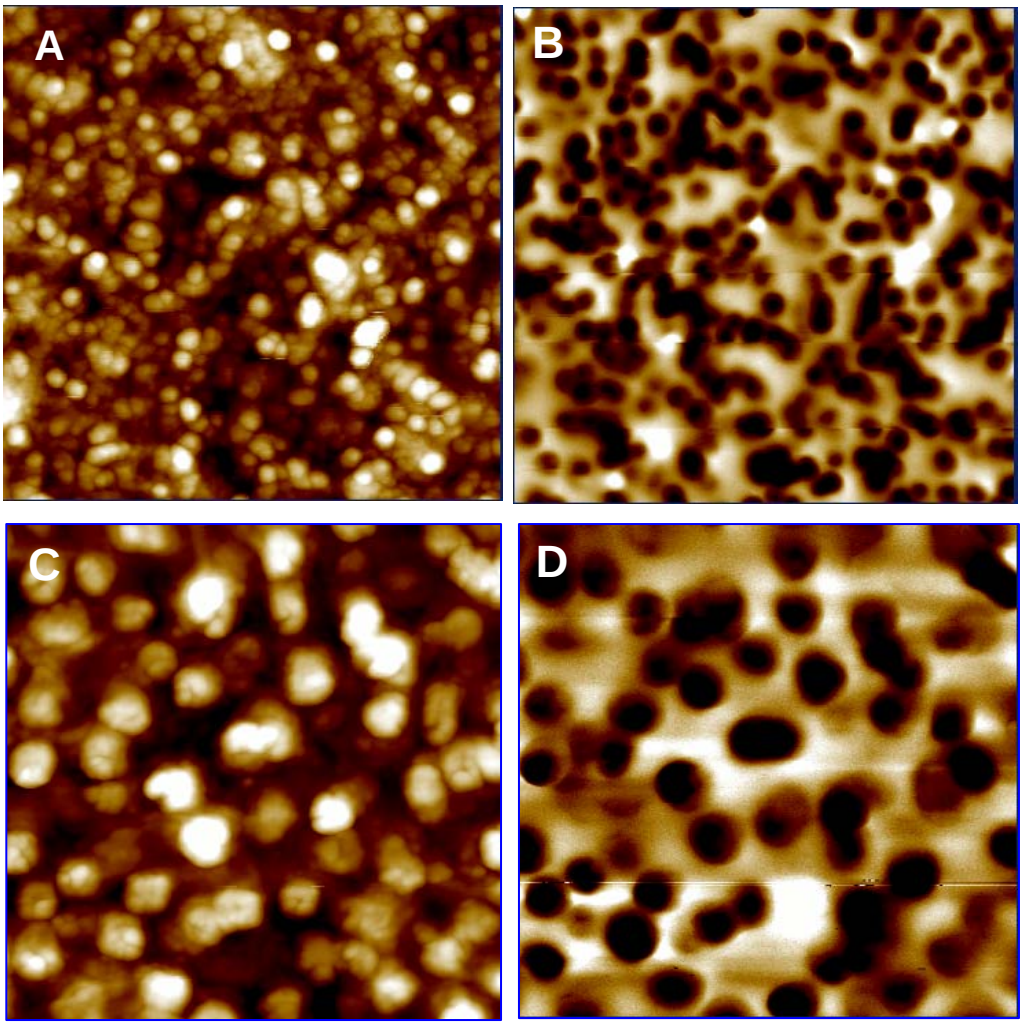

Fig.5.13 3 μm × 3 μm AFM and MFM images of the nanowires deposited at T = 840 °C. The growth rate was 8 Hz (A, B) and 3 Hz (C, D).

These results suggest that the lateral size of the nanowires increases as the growth rate is reduced. To verify this assumption, MFM imaging was performed on the samples grown at T = 840 and T = 740 °C after magnetizing the samples at H = 2 T and the magnetic phase images of the nanowires deposited at different rates were compared.

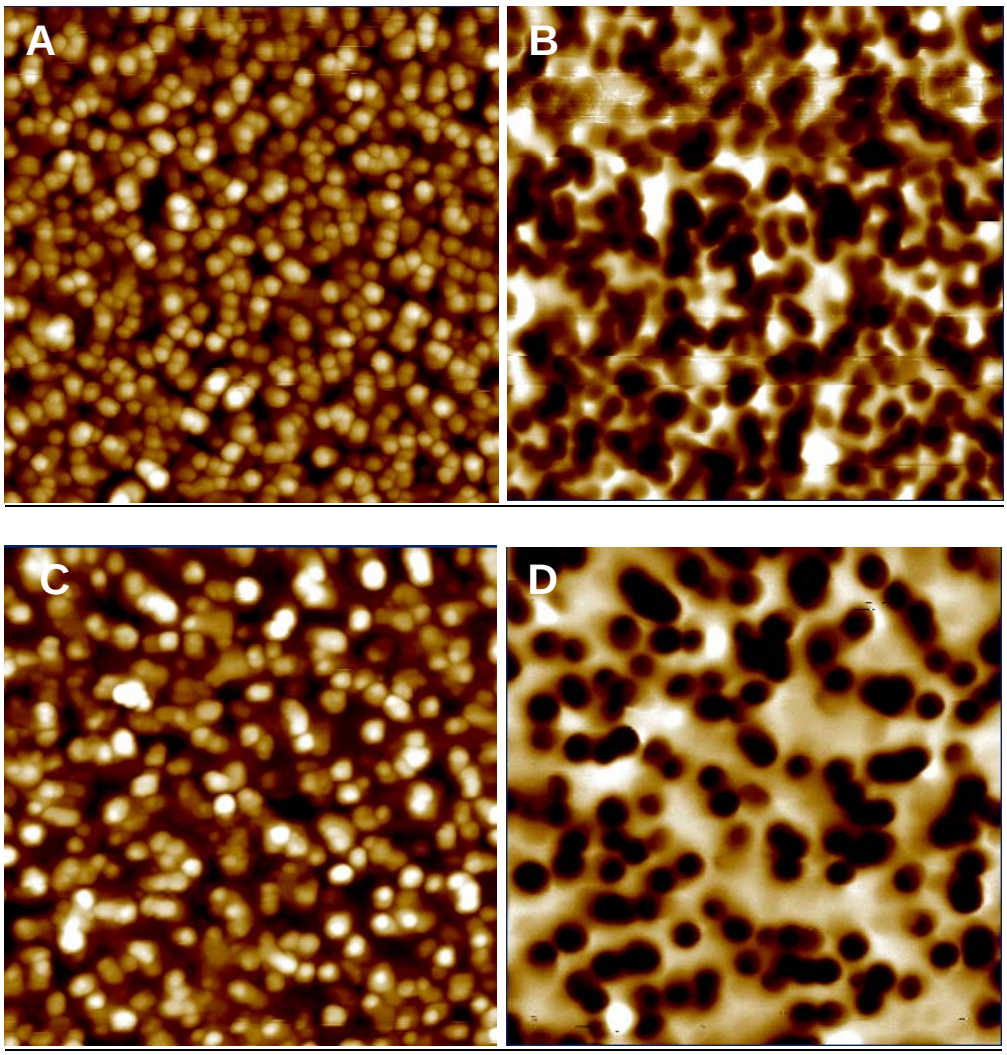

Fig.5.14 3 μm × 3 μm AFM and MFM images of the nanowires deposited at T = 740 °C. The growth rate was, 3 Hz (A, B) and 1 Hz (C, D).

Fig.5.13 compares the topography and magnetic phase images of the iron nanowires grown at T = 840 °C at the growth rates of 8 Hz (Fig.5.5) and 3 Hz (Fig.5.10) in a 3 μm × 3 μm area. The images clearly show that the size of the nanowires have

increased two to three times, which explains the drop in the coercivity and remanent magnetization in the hysteresis loop of Fig.5.10. The same result is observed for the samples grown at T = 740 °C (Fig.5.14) where the lateral size of the nanowires is increasing systematically with the reduction in growth rate. The similarity between MFM images in Fig.5.13 B (840 °C and 8 Hz) to Fig.5.14 B (740 °C and 3 Hz) suggests that the two samples should have diameters very close to each other. This is also evident when comparing the coercivity and remanence values of the above mentioned samples (H_C = 1240 Oe, M_r = 0.65 for Fig.5.13 B and H_C = 1500 Oe, M_r = 0.75 for Fig.5.14 B). Therefore, the MFM results veryifies that the lateral size of the nanowires and the growth rate are inversely proportional.

In this respect, analyzing hysteresis loops and MFM results together can provide valuable information about the kinetics of the growth without a specific need to perform time consuming TEM analysis. The results show the magnetic properties of the nanowires can be controlled with growth rate as well as growth temperature in the kinetically controlled growth mode.

Chapter 6 Growth of Carbon Nanotubes on α-Fe Nanowires

6.1 Definition and properties of carbon nanotubes

Carbon nanotubes are fullerene-related structures which consist of graphene cylinders closed at either end with caps containing pentagonal rings. A single-walled CNT (SWCNT) is a rolled tubular shell of graphene sheet which is made up of benzene-type hexagonal rings of carbon atoms as shown in Fig.6.1. Depending on how the two-dimensional graphene sheet is rolled, three types of SWCNTs are possible, namely armchair, zigzag and chiral nanotubes. The different types are most easily explained in terms of the unit cell of a carbon nanotube, i.e., the smallest group of atoms that defines its structure. As shown in Fig.6.1 a chiral vector is defined on the hexagonal lattice as $C = na_1 + ma_2$, where a_1 and a_2 are the unit vectors of the hexagonal lattice and are both integers. Different types of carbon nanotubes have different values of *n* and *m*. Zigzag nanotubes correspond to $n = 0$ or $m = 0$ and have a chiral angle of 0°, in armchair nanotubes $n = m$ and the chiral angle is 30°, while chiral nanotubes have general *n* and *m* values and a chiral angle of between 0° and 30°.

Depending on their chirality, nanotubes can either be metallic or semiconducting, which is very useful in device fabrication. All armchair SWCNTs are metals; those with $n - m = 3k$ where *k* is a nonzero integer are semiconductors with a small band gap; and all others are semiconductors with a band gap that depends on the inverse diameter of the carbon nanotube[85]. Single-walled CNTs also

show excellent mechanical properties such as high Young modulus of around 1 TPa and yield strength as large as 120 GPa.[86]

A multi-walled carbon nanotube (MWCNT) is a stack of graphene sheets rolled into concentric cylinders as shown in Fig.6.2 A[87,88]. The graphite basal plane or in other words the walls of each layer, of the MWCNT are parallel to the central axis ($\alpha = 0$). The electronic properties of perfect MWCNTs are rather similar to those of perfect SWCNTs, because coupling between the neighboring cylinders is weak in MWCNTs. Multi-walled carbon nanofibers (MWCNF) form when the graphite basal planes are not parallel to the central axis ($\alpha \neq 0$) as shown in Fig.6.2 B. In general MWCNFs consist of stacked curved graphite layers that form cones or cups. However, one cannot expect the same electrical, mechanical and chemical properties for nanofibers with nonzero α. In this case the graphene layers are relatively short and poorly connected, covering only part of the nanofiber. Similar to graphite, the charge transport along the nanofiber with $\alpha > 0$ is determined by both in-plane and interplane components which differ considerably. The same holds true with mechanical properties, as the van der Waals bonding is significantly different from the in-plane covalent bonding of MWCNTs ($\alpha = 0$). In addition, the comparison of the chemical properties shows that nanofibers contain exposed edges with unsatisfied valances that are quite different from the defect-free structures of nanotubes that do not contain any exposed edges or unsaturated bonds of graphene planes. Therefore, nanotubes are far less reactive than nanofibers.

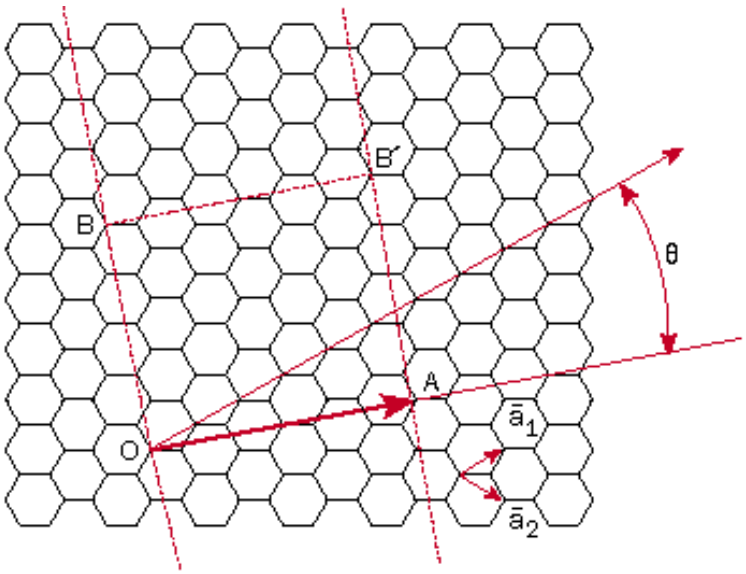

Fig.6.1 Schematic drawing of graphene sheets rolling for carbon nanotube formation.

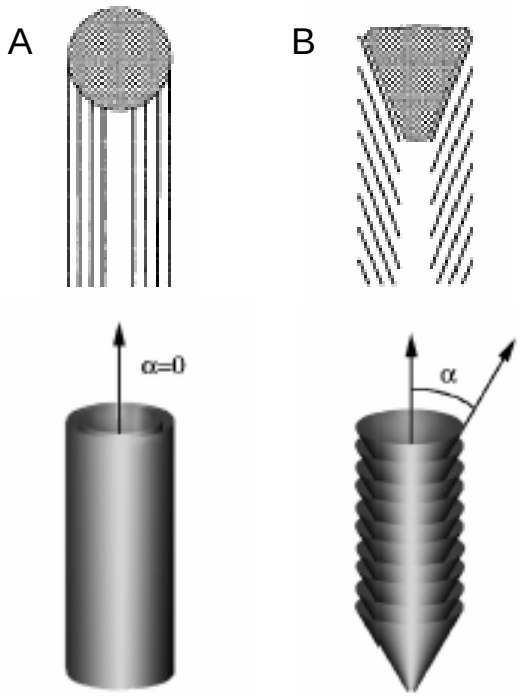

Fig.6.2 Comparison of A. multiwalled CNT, with B. multiwalled CNF[87].

6.2 Synthesis of carbon nanotubes

6.2.1 Methods

Initially, the laser ablation and arc discharge methods were developed for growth of single-walled and multi-walled CNTs and are still being used by researchers. While arc discharge and laser ablation are very efficient methods for producing high-quality CNTs in large quantities they do not offer control over the spatial arrangement. In recent years catalytic chemical vapor deposition (C-CVD) has been widely used for CNT growth and has proven to be a suitable method when controlled growth is desired. Catalytic plasma enhanced CVD (C-PECVD) has also been investigated for its ability to produce vertically-aligned nanotubes. In addition, C-PECVD allows deterministic synthesis in which the location, size, shape and structure of each individual nanofiber are controlled during the synthesis. The material obtained by this method is phase pure and no purification is needed[87]. The CNT growth method used in this dissertation is C-PECVD.

6.2.2 Catalyst

The growth of carbon nanotubes is catalytically controlled and therefore, the choice of the catalyst plays an important role in determining the outcome. The catalyst is responsible for different steps in the CNT growth mechanism which is explained in detail later in this chapter. The choice of catalyst is important as the catalyst is responsible in breaking carbon bonds and adsorbing it at its surface, then diffusing carbon through or around an interface where the carbon reforms in graphite planes.

Therefore, the properties of the catalyst play an important factor as they determine the rate of these steps as well as the degree of crystallinity and geometric structure of the resulting carbon nanotubes or nanofibers.

A variety of metals and their alloys are used as catalysts in producing CNTs. The most commonly used and studied are transition metal catalysts such as Fe, Ni, and Co which are known to be very active in their ability to break and reform carbon-carbon bonds.

There are numerous ways to prepare catalysts including physical vapor deposition (PVD), electroplating and solution-based catalyst preparation methods which are more common in thermal CVD. In a solution-based catalyst a typical preparation includes several steps such as dissolution, stirring, precipitation, refluxing, separation, cooling, gel formation, reduction, drying, annealing, calcinations, etc. The overall process is time consuming and cumbersome. Another problem is the difficulty of having nanoparticles to form within the small patterns. In the non-solution-based methods a thin film is deposited by one of the above mentioned methods and then it is either patterned to specific size with conventional lithography methods or it is sintered into islands or discrete nanoparticles. The size of the catalytic particle mainly depends on the thickness of the film. Wetting properties of the catalyst and substrate as well as the method of the catalyst preparation are also important deterministic factors in the final size of the nanoparticles. If periodic arrays of CNFs are desired, the amount of material for each catalyst dot is crucial in determining if single or multiple fibers will form. The same holds true for the diameter and thickness of the lithographically defined catalyst dot.

6.2.3 Hydrogen

Hydrogen partial pressure is known to have a significant effect on the rate at which carbon grows. It has been thought to be a catalyst for carbon producing reactions. Hydrogen might be present as H_2 gas or it might come from the hydrocarbons such as methane (CH_4) and acetylene (C_2H_2), or etchant such as ammonia (NH_3) used in the reaction. Nolan et al.[89] proposed a now well-known theory on the effect of the hydrogen. They pointed out that the forms of carbon found when no hydrogen is present are all "closed", which means there are no open-edged graphite planes. Nanofibers have open-edged graphite planes. Truncated graphite planes would have a high surface energy with a series of unsatisfied valences. Therefore, the surface of a nanofiber would be energetically difficult to form. If something is present to cap the surface bonding sites, formation of the open edges becomes energetically feasible. Thus according to Nolan et al., regardless of where hydrogen comes from or what intermediate steps are involved, the end result of hydrogen presence would be to form graphite plane edges. Based on this theory when hydrogen is not present the edges do not form and therefore, only closed forms of carbon such as shells and nanotubes are expected to form as they are energetically favorable.

6.3 Growth mechanism of carbon nanotube

The catalytic nature of the carbon filament growth was found when the metal particles associated with them were observed. Since then the growth mechanism of the CNFs has been widely studied by many different groups. Based on the careful

electron microscopy observation by Baker et al.[90] a growth mechanism was proposed which includes the following steps: (1) adsorption and decomposition of the reactant hydrocarbons on the surface of the catalyst particle, (2) solution and diffusion of carbon species into the catalyst and (3) precipitation of carbon on the other side of the catalyst particle to form the nanofiber structure. The kinetics of these three steps determine the growth rate.

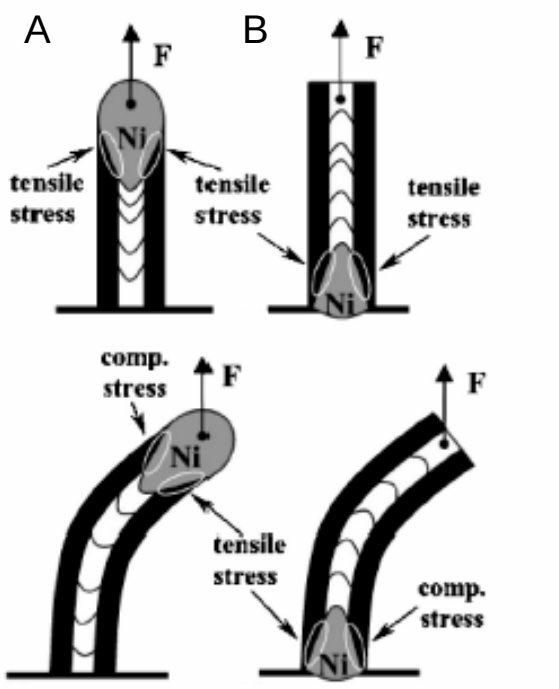

Fig.6.3 Two different CNT growth modes[91], A. tip-type and B. base-type. CNT alignment mechanism based on stress-dependent growth rate and stress distribution caused by interaction of nanofibers with electric field is depicted.

In general two different growth modes have been observed: (a) tip-type and (b) base-type as shown in Fig.6.3[91]. In tip-type mode the catalyst is detached from the substrate and remains on the tip of the growing carbon nanofiber, whereas in base-type growth the catalyst particles remain on the substrate. The determining factor in the growth mode is believed to depend on the interaction of the catalyst with its support, which is related to the wetting properties and contact angle of the catalyst and the substrate. Therefore, the choice of the catalyst and substrate plays an important role in determining the growth mode. In the case where the particle attachment to the substrate is weak (large wetting angle), carbon precipitation occurs at the bottom surface of the catalyst particle and the carbon fiber lifts the particle as it grows. The kinetics of growth also have a strong influence on determining the growth mode. It has been shown that using the same catalyst and substrate (e.g. Ni on a thin Ti layer) will result in tip-type mode with the PECVD growth method and base-type mode with the CVD growth method[92].

6.4 Catalytic plasma enhanced chemical vapor deposition

Plasma Enhanced Chemical Vapor Deposition (PECVD) has attracted considerable interest due to its ability to produce vertically-aligned carbon nanofibers (VACNF). In contrast to the T-CVD growth method which uses thermal energy to activate the gas, in PECVD the molecules are activated by electron impact. The gas activation takes place in nonequilibrium plasma (glow discharge). The main purpose of using plasma enhancement is to reduce the activation energy required for the deposition

process. In addition, the most important benefit of the PECVD growth method is the alignment of nanofibers due to interaction with the electric field.

6.4.1 PECVD experimental system

A PECVD consists of a vacuum chamber, vacuum pumps, a pressure control system, a gas flow control system, mass flow controllers, power supplies for plasma excitation and a showerhead for uniform gas mixing and distribution over the substrate. Several plasma sources have been used for CNT and CNF growth. These sources include direct current (dc PECVD), hot filament dc (HF-dc PECVD), radio frequency (rf PECVD), inductively coupled plasma (ICP PECVD), and microwave (M-PECVD).

A dc plasma reactor consists of a pair of electrodes in a grounded vacuum chamber with one electrode grounded and the second connected to the power supply. The negative dc bias applied to the cathode leads to a breakdown of the feed gas. A wafer with a catalyst layer can be placed either on the anode or cathode for CNT deposition. The electrode holding the wafer may need an independent heating source to raise the temperature of the wafer to the desired growth temperature. A resistive heater or a tungsten wire suspended in plasma (hot filament) can be used as the heating source. A schematic of the PECVD system is shown in Fig.6.4 [87].

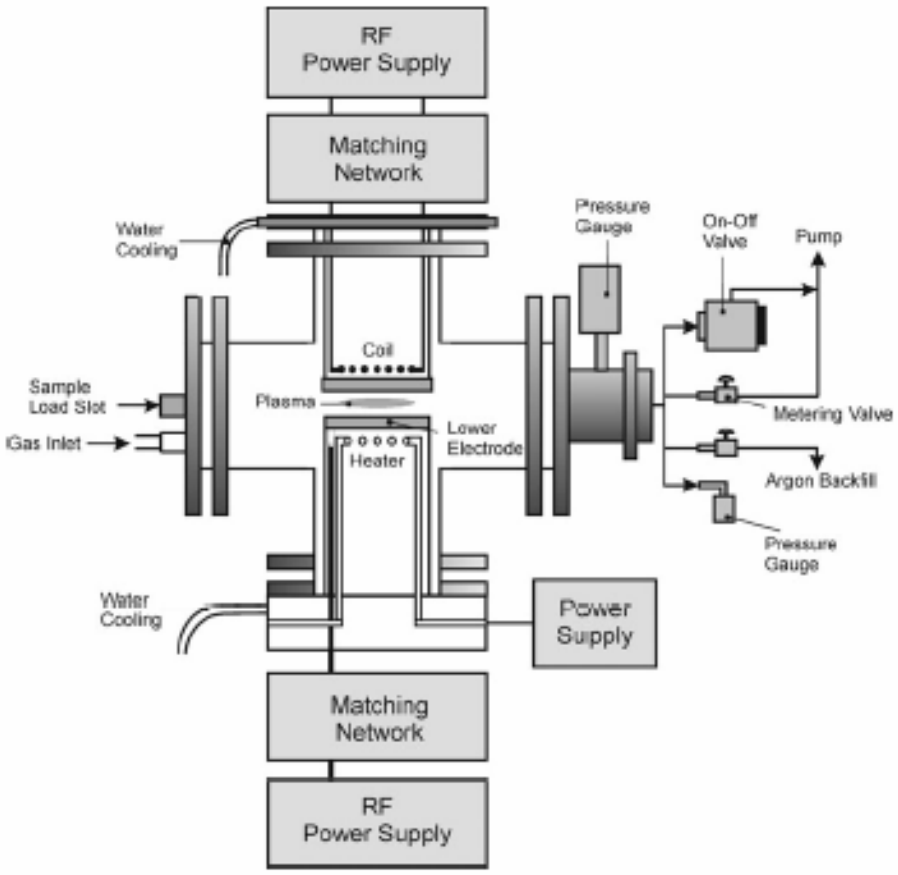

Fig.6.4 Schematic of PECVD system[87].

In the case of direct current PECVD growth, the substrate is placed on a heater which also serves as a cathode, so it is necessary that the substrate be electronically conductive. Transition metals are necessary for CNT growth by PECVD. Otherwise, amorphous carbon or diamond will result depending on plasma and surface condition. In the growth process following the catalyst preparation, the sample containing the catalyst is mounted on the cathode heater and the vacuum chamber is then evacuated to an acceptable base pressure (1×10^{-5} Torr). After reaching the desired base pressure,

the wafer is heated to the desired temperature and ammonia (NH_3) is introduced into the chamber, and then the sample is pretreated with NH_3 plasma. After the pretreatment step, a typical hydrocarbon source such as methane, ethylene or acetylene is introduced to the chamber while maintaining NH_3 plasma. This will result in immediate growth of vertically aligned carbon nanofibers (VACNF). Since the plasma can dissociate the hydrocarbon creating a lot of reactive radicals, the use of pure hydrocarbon feedstock may lead to substantial amorphous carbon deposition. Therefore the ammonia, argon or hydrogen is usually used to dilute the hydrocarbon. The tip diameter of the VACNF is approximately equal to that of the nanoparticles.

It is important to note that plasma is in general used for both deposition of thin conformal films and for etching, depending on the choice of conditions. Counter-intuitively, in order to "deposit" carbon nanostructures the PECVD reactor must be operated in the etching, rather than in the deposition regime to avoid thin film formation. Therefore, a balance between etching and deposition should be considered to prevent carbon films and at the same time avoid damage to the sidewalls of growing nanofibers.

6.4.2 CNT growth mechanism in PECVD

The majority of studies and work on the growth and application of vertically aligned carbon nanofibers have focused on the simplest of the PECVD, namely dc and HF-dc, systems. The growth mechanism is similar to that of thermal CVD with the addition of a few steps and is listed as the following: (A) arrival of excited species to the

surface, (B) catalytic dissociation, (C) departure of undissociated molecules, (G) dissolution of carbon species on the catalyst surface, (D) formation of a carbon layer on the surface of the catalyst, (H) diffusion of the carbon species into or around the catalyst, and (I) incorporation of the carbon atoms into a growing graphene layer. A schematic of the process is shown in Fig.6.5[93]. In a PECVD system a few processes are added to this general mechanism due to the presence of an electric field and partial ionization of the gas. These include (F) sputtering due to ion bombardment, (E) chemical etching, and mechanical force due to the interaction of a conducting cylinder with a high electric field.

This system will result in the growth of vertically aligned MWCNTs and MWCNFs. The vertical alignment in the PECVD method is due to the coupling of (a) the mechanical force resulting from interaction of the conducting cylinder with an electric field and (b) the rates of carbon incorporation into graphene layers around the catalyst, via stress distribution. In contrast, the marginal alignment observed in the thermal CVD method is due to a crowding effect which results in a forest-like growth where nanotubes support each other by van der Waals attraction.

Due to the production of various hydrocarbon radicals such as CH_x, C_2H_y, and C_3H_z and also a number of stable species such as C_2H_2, C_2H_4, and C_3H_8 in PECVD, it is difficult to produce SWCNTs using a PECVD system. It has been suggested that SWCNT growth requires (a) temperatures of 900 °C in order to have enough kinetic energy for the carbon layer to bend and form small caps and (b) low carbon supply on the catalyst surface. This is the reason that SWCNT growth is carried out in thermal CVD systems at temperatures of 900-1000 °C and the carbon source is mainly CO or

CH_4. The lowest number of walls seen to date using the PECVD method is reported to be two[92] and only one group has been able to produce SWCNTs, using rf PECVD on zeolite substrate[94].

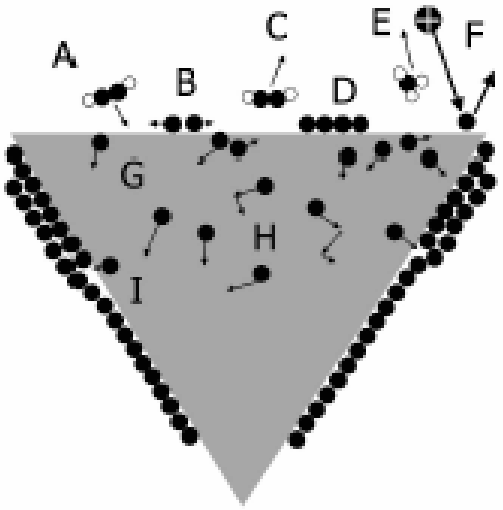

Fig.6.5 The carbon nanotube growth process in a PECVD system[93].

In the C-PECVD process the changes in growth parameters can cause drastic structural and morphological changes in the form of the deposited carbon, ranging from amorphous carbon films to nanofibers and nanotubes. These parameters include: (a) total pressure, (b) total gas flow, (c) carbon source to etchant gas flow ratio (e.g. CH_4/NH_3), (d) substrate temperature and (e) plasma power (current and voltage). Fig.6.6 shows the different deposited carbon structures which are obtained by changing the temperature (T) with respect to the carbon source to etchant gas ratio

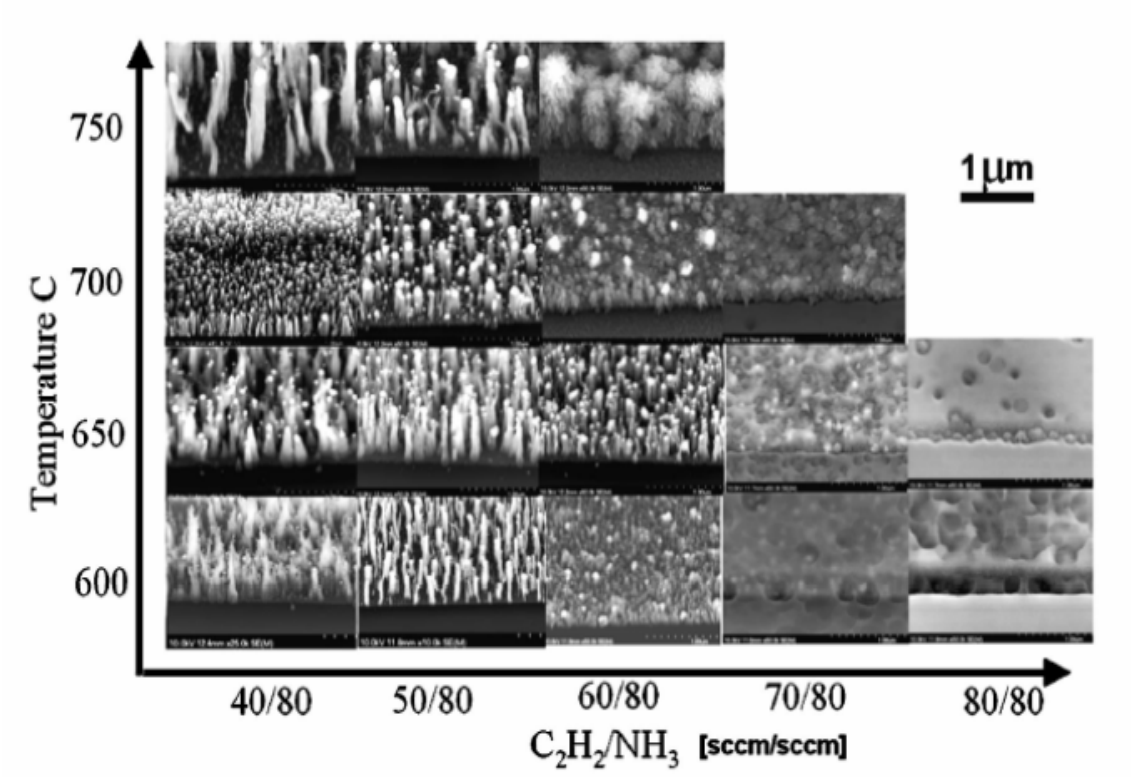

Fig.6.6 ESEM images of VACNFs showing the phase diagram of the VACNF in a T-R slice of the multidimensional parameter space[87].

(R). As can be seen in this figure for a specific temperature there is a particular range of C_2H_2/NH_3 for which the growth of high-quality VACNFs can occur. For a given temperature, at small values of C_2H_2/NH_3 the fibers are chemically etched during the growth, producing heavily damaged fibers; for large values of C_2H_2/NH_3 a graphite type carbon film is formed which prevents nanofiber growth. In addition, at higher plasma powers growth of high quality CNFs occurs at higher values of C_2H_2/NH_3.

6.5 Vertically aligned CNTs and CNFs

A variety of methods for production of vertically aligned (perpendicular to substrate) CNTs using thermal CVD have been demonstrated. The most frequently referred to in the literature are nanotubes or nanofibers grown in a very dense arrangement. As mentioned earlier in this arrangement vertical alignment is achieved due to the crowding effect. When densely packed the CNTs attract the outermost nanotubes of their neighbors via van der Waals forces and produce oriented growth.

Using a self-assembled alumina nanoporous template is another method to grow vertically aligned CNFs. The catalyst is electrodeposited into the pores of the template and nanotubes are synthesized by the CVD process. The template then can be etched away and an array of aligned CNFs remains.

As mentioned above, in the PECVD process, an electric field is responsible for the vertical alignment of CNFs. As in thermal CVD both tip-type growth and base-type growth modes are observed in CNFs grown by PECVD. A direct correlation between the alignment of CNFs and the growth mode (base or tip) has been observed in this process [93]. As shown in Fig.6.3, in the tip-type growth mode the catalyst undergoes a process which eventually results in its detachment from the substrate; the catalyst then follows the path of the electric field present in the plasma sheath. This type of growth leads to vertical alignment regardless of the density of the CNFs present. In contrast, in base-type growth mode the alignment of CNFs tends to be in random orientations unless the density of the fibers is high enough for a crowding effect. In their review of the PECVD process Meyyappan et al.[87] have shown that the large bias at the substrate helps the growth of vertically aligned

MWCNFs with the catalyst particle on the top. In contrast, when the bias is low or with a microwave reactor with no dc substrate bias, the results are mostly MWCNTs with the catalyst at the base.

Melenchko et al. have described the alignment as the result of a feedback mechanism associated with nonuniform stress at the interface of the catalyst and CNF which is caused by electrostatic forces[93]. For a perpendicular CNF there is a uniform tensile stress across the entire catalyst-CNF interface which is in the direction of the applied electrostatic force as shown in Fig.6.3. This is regardless of whether the catalyst is formed on the top or the base. When carbon precipitates across the interface the fiber continues to grow perpendicular to the substrate. But if there is a spatial fluctuation in the carbon precipitation at the interface, CNF growth will diverge from its perpendicular path as shown in Fig.6.3. This would lead to nonuniform stresses at the catalyst-CNF interface. When the catalyst particle is at the top, the electrostatic force causes a compressive force at the interface where the growth rate is greater and a tensile stress on the other side where the growth rate is lower. These opposing stresses favor subsequent carbon deposition at the interface with the tensile stress. The net result is a stable, negative feedback that equalizes the growth rate everywhere and the vertical alignment is maintained. In the case of base-type growth, the stress in the interface with highest growth rate is tensile; this further increases the growth rate at the same location and causes more bending of the nanotube. This is essentially an unstable positive feedback system.

Another type of vertically aligned carbon nanostructure formed by the PECVD process is the conical structure. Carbon nanocones (CNCs) provide

substantially higher mechanical and thermal stability compared to the narrow cylinder structure of CNFs and CNTs. By adjusting the growth parameters such as the ratio of acetylene (C_2H_2) to ammonia[95] or by changing the bias[96] in the PECVD system, vertically aligned CNCs rather than CNFs can be formed. The important aspect of the CNCs is that the tip diameter of the cone does not change during the growth and is determined by the catalyst particle. In contrast, the base diameter as well as height of CNCs increases with growth time. Therefore, by adjusting the growth condition both lateral and longitudinal growth can be obtained. Consequently, very tall cones with sharp tips and large and robust bases can be formed. Fig.6.7 shows an example of CNC growth[91]. Merkoluv et al. explain the conical growth due to increase in acetylene level as the following: in a PECVD system, in addition to thermal decomposition of acetylene, various species formed in the glow discharge such as C neutrals, S ions and also reactive etchant species (H^+, N^+, etc.) formed from plasma decomposition of ammonia and acetylene are also present. The neutrals move in random directions, whereas the electric field line dictates the travel direction of ions. If the amount of acetylene increases then in addition to the vertical growth, carbon begins to precipitate at the walls of the initially cylindrical VACNF. In this case the carbon deposition rate is higher than the etching rate. The net result is growth in two directions: (a) vertically (catalytic growth via carbon diffusion through the particle) and (b) laterally (by precipitation of C from the discharge at the outer walls of the VACNF) as shown in Fig.6.7 B.

Carbon nanocones are important in applications where both high aspect ratio and mechanical stability are required. The tips can be tailored to suit specific applications.

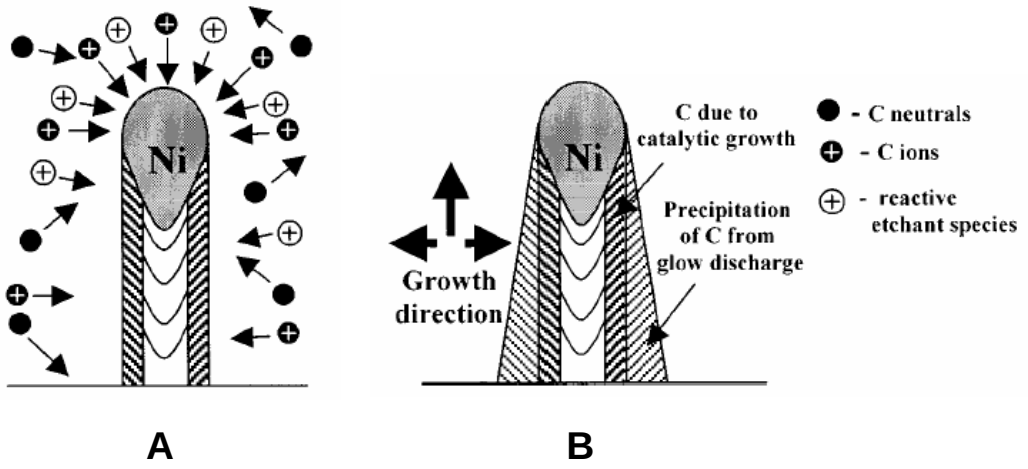

Fig.6.7 Schematic of the growth of A. a vertically aligned carbon nanostructure using PECVD and B. a carbon nanocone formed due to additional precipitation of C at the outer walls during PECVD[91].

6.6 Applications of carbon nanotubes

The interesting combination of the electronic, mechanical and chemical properties of carbon nanotubes has led to a wide range of investigations on their potential applications in the last decade. The possible applications of CNTs include field emitters, sensors, electrodes, conductive and high strength composites, energy storage and conversion devices, storage of hydrogen, lithium and other metals, and nanosized semiconductor devices, probes and interconnects.

The focus of industrial and academic research has mainly been on using SWCNTs and MWCNTs as a field emission electron source for panel displays, lamps, x-ray, and microwave generators[85]. Field emission involves the extraction of electrons from a solid by tunneling through the surface potential barrier, typically equal to the work function of the material. A potential applied between a carbon nanotube coated surface and an anode produces high local fields. The local fields cause electrons to tunnel from nanotube tips into the vacuum. Electric fields direct the field-emitted electrons toward the anode, where a phosphor produces light from the flat panel display application.

Vertically aligned CNFs are good candidates for field emission displays. The advantage of CNT field emitters over conventional tungsten and molybdenum tip arrays are that CNTs provide stable emission, long lifetimes and low emission potentials. They are relatively easy to fabricate and do not deteriorate in moderate vacuum (10^{-8} Torr) compared to tungsten and molybdenum which need vacuum levels of less than 10^{-8} Torr and are more difficult to fabricate. Current densities as high as 4 A/cm^2 have been obtained which are substantially higher than the 10 mA/cm^2 needed for flat panel field emission displays.

6.7 Carbon nanotubes grown on self-assembled iron nanowires

6.7.1 Experimental procedure

The experiments were carried out using a dc-PECVD with an infrared heating lamp built at SungKyunKwan University in Suwon, Korea. The schematic of the system is

shown in Fig.6.8. The gases used as the carbon source and the etchant were C_2H_2 and NH_3, respectively. Phase decomposed α-Fe nanowires embedded in the $LaSrFeO_4$ matrix were used as the catalyst for CNT growth. Different diameters of iron nanowires (d_{avg} = 8, 17, 45 nm) and also various thicknesses of the thin film (l = 40, 90, 330 nm) were chosen for CNT growth by dc-PECVD. Prior to CNT growth the samples were etched with 10^{-5} molar H_2SO_4 for 5 seconds and then rinsed with deionized water so that the laser particles and the tip of the iron nanowires were etched away. Therefore, in the resulting structure iron nanowires are slightly etched below the surface of the matrix.

After etching, the samples were transferred into the vacuum chamber of the dc-PECVD system and a mechanical pump reduced the chamber pressure to around $P = 5\times10^{-2}$ Torr. The argon gas was introduced to the chamber (P = 8 Torr) and the power for the infrared heater was turned on, heating the substrate to T = 650 °C. The heating rate is high and it takes around 3 minutes to reach the desired temperature of T = 650 °C. Subsequently, C_2H_2 and NH_3 gases were introduced into the chamber and the total pressure in the chamber was kept at P = 3.25 Torr. The ratio of NH_3 to C_2H_2 and the total gas flow rate were 4 and 150 sccm, respectively. When the pressure was stabilized, the power for the dc power supply was turned on. The bias voltage for plasma generation was kept at around V = 620 V and the current was I = 0.12 mA. No pre-treatment (surface etching) with NH_3 plasma was performed prior to CNT growth. The growth time was varied between 2, 6, and 12 minutes to study the effect of the growth time on the CNT morphology. After the growth the plasma power and infrared heater were turned off and the samples were cooled down in vacuum (P =

0.018 Torr) to around T = 80 °C before being removed from the chamber. The total time for cooling was around t = 20 min.

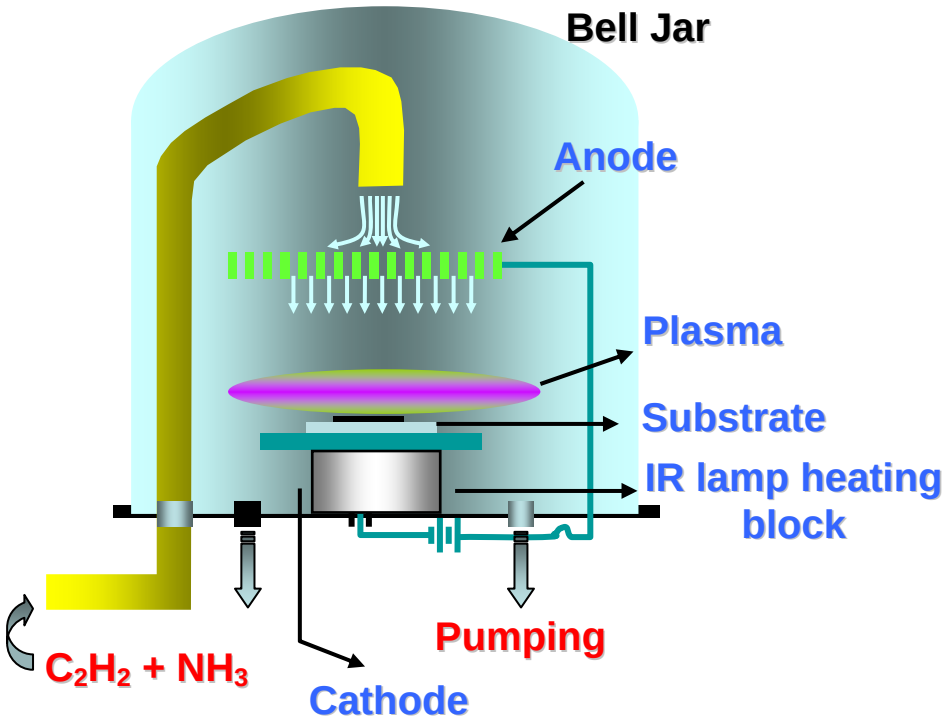

Fig.6.8 Schematic of the dc-PECVD system used in this research.

The morphology of the obtained carbon nanotubes was observed by environmental scanning electron microscopy (ESEM, Philips XL30 ESEM-FEG). High resolution TEM (JEOL-JEM-2100F) operating at 200 kV was used to study the microstructure of the CNTs. The binding state of the carbon nanotubes was examined using Raman Spectroscopy (Renishaw Invia Basic) equipped with argon ion laser with an excitation wavelength of λ = 514.5 nm and powered to 5 mW. Electron field emission

was measured as a function of applied voltage using a stainless steel anode and a glass spacer. The spacing between the anode and the tip of the CNTs was approximately 0.2 mm. The measurements were performed in a vacuum chamber with a pressure of better than $P \leq 5 \times 10^{-6}$ Torr.

6.7.2 Characteristics of the CNTs

The carbon nanotubes were grown on phase decomposed $LaSrFeO_3$ thin film samples consisting of self-assembled α-Fe nanowires embedded in $LaSrFeO_4$. As mentioned above, the samples were first etched with 10^{-5} molar H_2SO_4 for 5 seconds to prefentially etch the tip of the iron nanowires as shown schematically in Fig.6.9. The purpose of etching is so that one nanowire will serve as one nucleation site for the growth of CNTs.

Fig.6.10 shows the ESEM images of the surface of the thin films containing iron nanowire before and after etching. The diameter of the α-Fe nanowires in these films is around d = 17 nm. As is shown in these images, after etching, black spots appear on the surface which indicates that the tip of the iron nanowire has been etched. The etching time was varied between t = 0.5 sec to t = 2 minutes to determine the optimum etching time. For the etching time bellow t = 3 sec no significant changes were observed in the surface morphology. Etching times between $5 < t < 10$ sec show similar morphologies but the surface for t = 10 sec was not very smooth. Increasing the etching time to above 10 sec causes the film to be etched away from a different location. An example is shown in Fig.6.11 for the film etched for t = 30 sec.

For etching longer than t = 2 min the film dissolved completely and only the substrate remained.

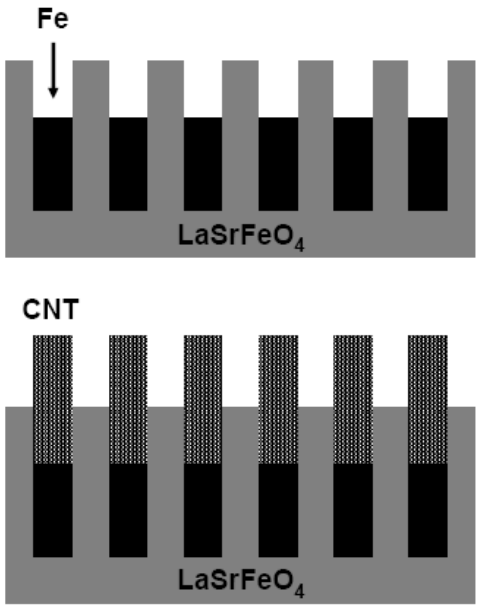

Fig.6.9 Schematic of CNTs grown on top of the etched α-Fe nanowires.

The CNTs were grown on top of the etched samples. The growth time was varied between t = 2, 6 and 12 min. Fig.6.12 shows the ESEM images of the CNTs grown on the samples with initial α-Fe nanowires of diameter and lengths of d_{avg} = 17 and l = 90 nm. The growth occurs in tip-top mode and Raman spectroscopy obtained from the sample (shown in Fig.6.13) reveals the multi-walled characteristic of the CNTs. Table 6.1 summarizes the effect of increasing growth time for the CNTs grown on iron nanowires with average diameter of d = 17 nm .

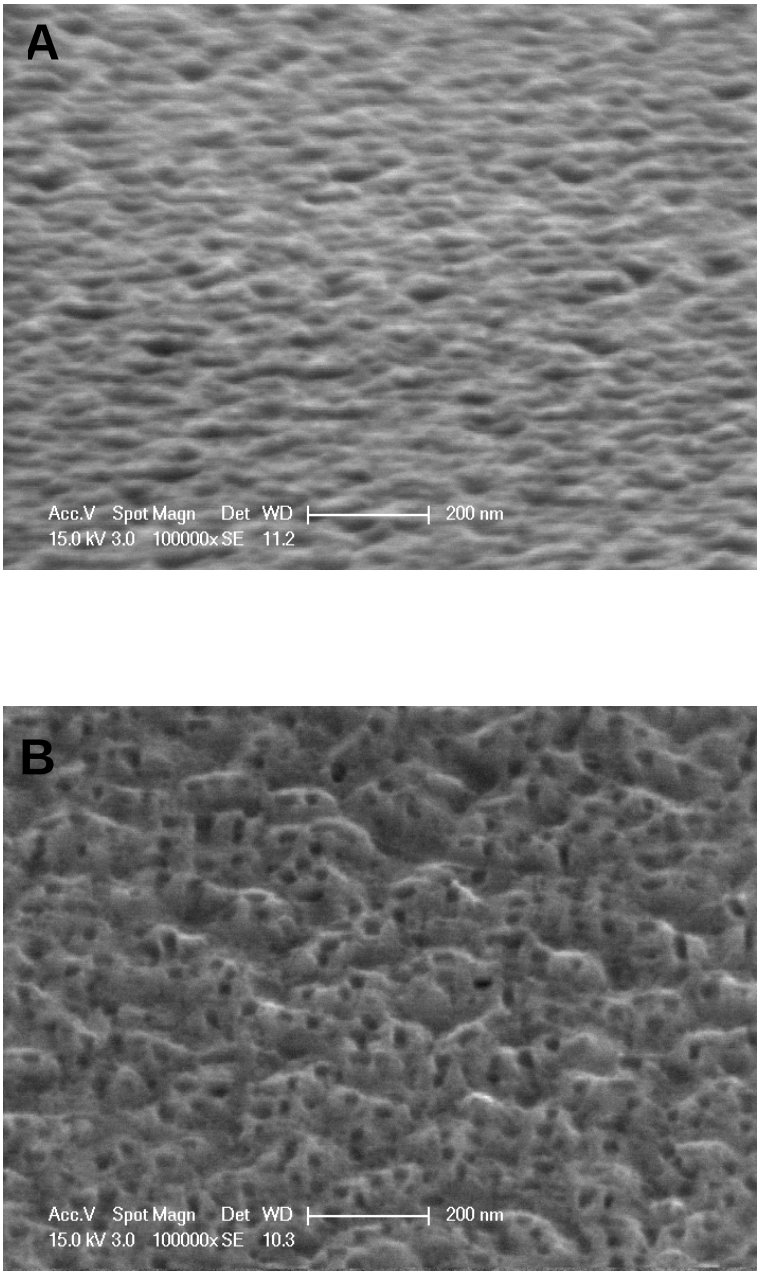

Fig.6.10 ESEM images of the α-Fe nanowires; A. as deposited, B. after etching for *t* = 5 sec.

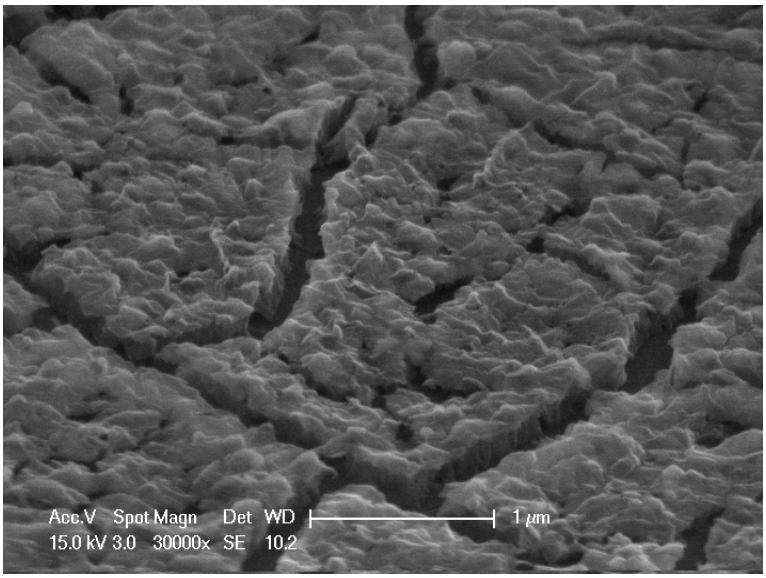

Fig.6.11 ESEM image of the iron nanowires embedded in $LaSrFeO_4$ matrix after etching for t = 30 sec.

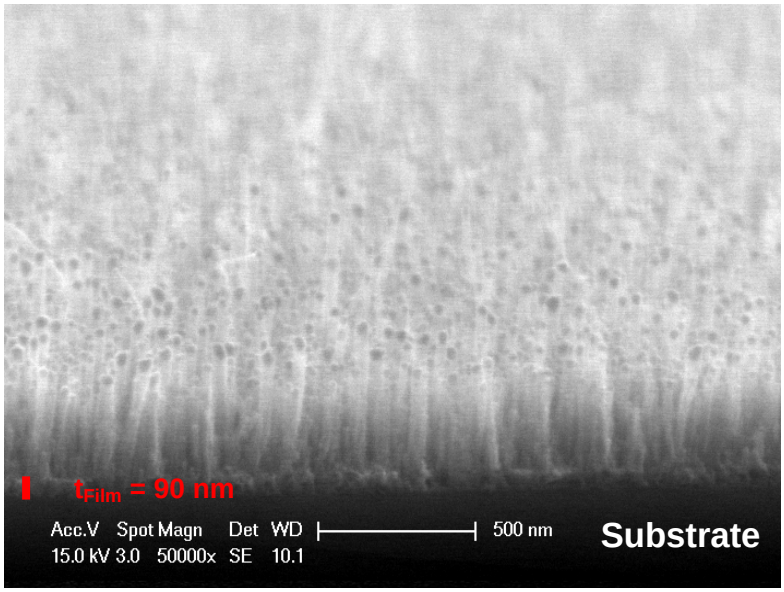

Fig.6.12 The CNTs grown on α-Fe nanowires with d_{avg} = 17 nm and l = 90 nm. The growth time was 12 sec.

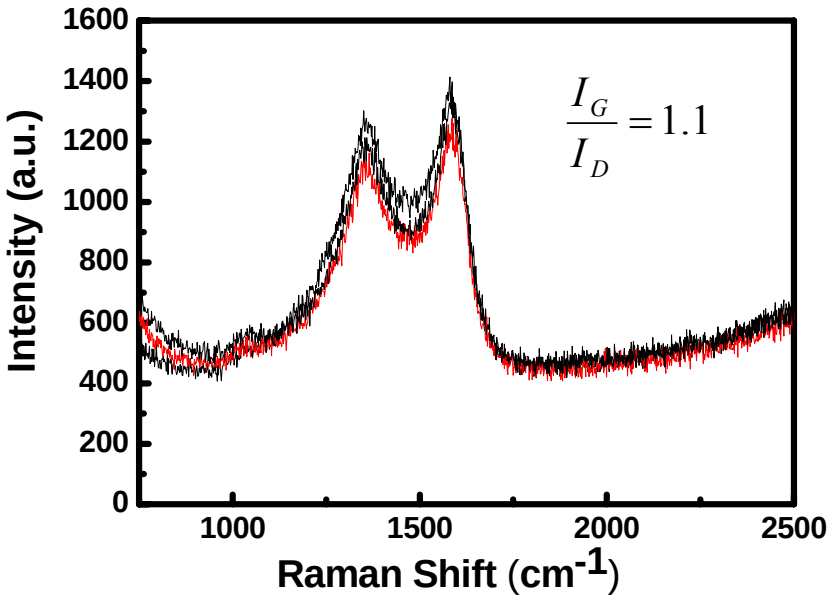

Fig. 6.13 Raman spectrum of the multi-walled CNTs grown on iron nanowires

	d_{Fe} = 17 nm								
	Growth Time = 2 min			Growth Time = 6 min			Growth Time = 12 min		
	Structure	D (nm)	L (nm)	Structure	D (nm)	L (nm)	Structure	D (nm)	L (nm)
330 nm	Cone	Tip = 40 Base = 80	290	Cone	Tip = 40 Base = 80	400	Cone	Tip = 40 Base = 80	625
90 nm	Cylinder	33	270	Cylinder	35	400	Cylinder	35	610
40 nm	Cylinder	25	170	Cylinder	25	280	Cylinder	25	440

Table 6.1 The effect of growth time on carbon nanotubes grown on iron nanowires with diameter of d = 17 nm and length of l = 330, 90 and 40 nm.

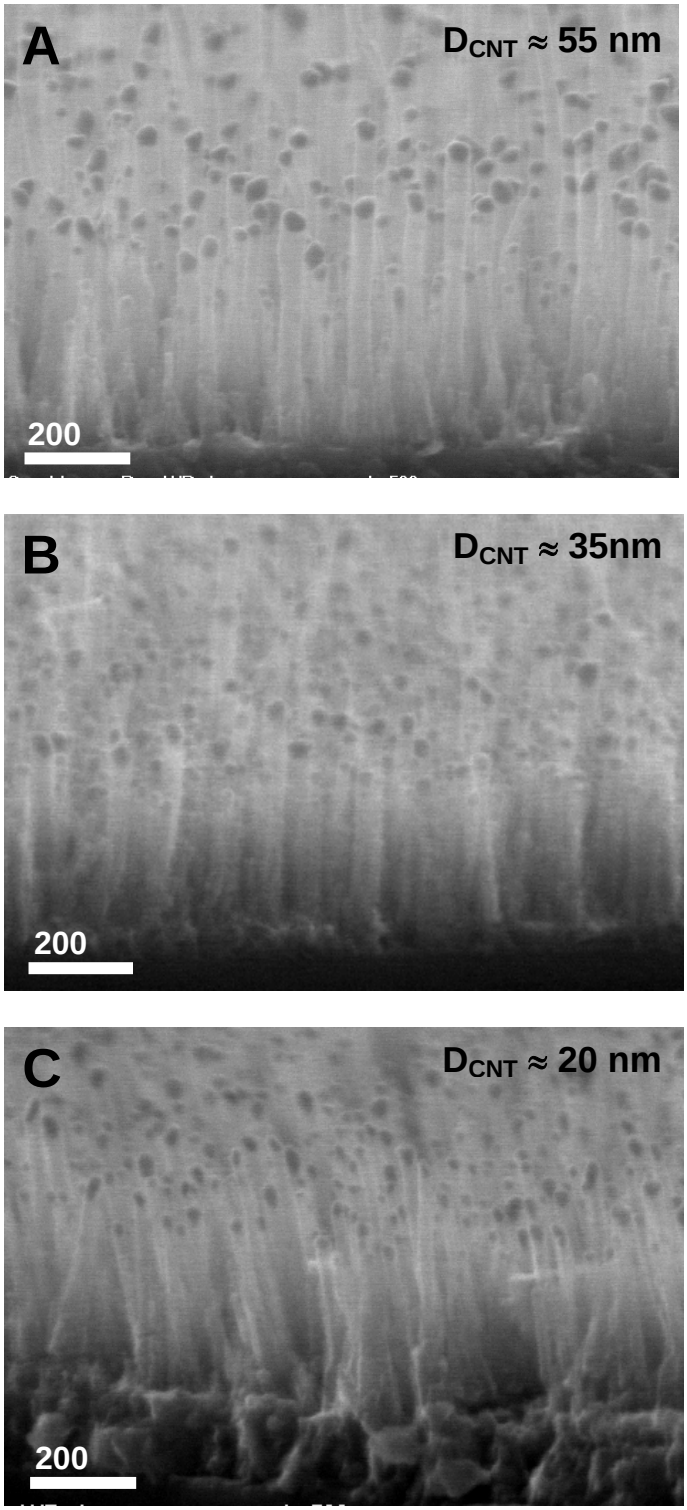

Fig 6.14 ESEM images of the CNTs grown on top of iron nanowires with diameters of A. d = 45 nm, B. d = 17 nm, and C. d = 8 nm.

As shown here, the length of the CNTs increases with the growth time for different length of iron nanowire catalysts. Also it is observed that the lengths of the carbon nanotubes are shorter when grown on the thinner samples (l = 40 nm). Increasing the growth time beyond t = 12 min did not increase the length of the CNTs significantly, indicating that t ≈ 12 min is the point of dc-PECVD diminishing growth in our experiments.

Fig.6.14 shows the ESEM images of the carbon nanotubes grown on the iron nanowires with length of l = 90 nm and varying diameter of d = 45, 17, and 8 nm. The growth time was around t = 12 min. As is observed in these ESEM pictures, the diameter of the carbon nanotubes changes from D = 55 to 35 and 20 nm as the iron catalyst diameter changes from d = 45 to 17 and 8 nm, respectively.

Transmission electron microscopy was used to verify the structure of the carbon nanotubes. TEM specimens were prepared by immersing the samples in an ethanol solution and then placing them in an ultrasonic bath for t = 10 min. After this a drop of the solution was placed on the coated side of the copper grid and left to be dried. Fig.6.15 shows the TEM images of CNTs grown on iron nanowires with diameter and length of d = 8 and l = 40 nm, respectively. The image and similar results from other samples clearly show that the graphene basal planes are not parallel to the central axis and therefore, multi-walled carbon nanofibers have formed.

Another interesting feature of these MWCNFs is revealed in Fig.6.16. These ESEM images are taken from the MWCNFs grown on iron nanowires catalyst with initial α-Fe nanowire diameter of d_{avg} = 17 nm and varying length of l = 40, 90, and 330 nm. As depicted in these ESEM images, the shape of the carbon nanotubes grown

on the nanowires with l = 330 nm is different from the ones grown on thinner samples. The carbon nanotubes grown on the self-assembled nanowires on the thicker samples (l = 330 nm) have a conical shape whereas the ones grown on thinner films (l = 40, 90 nm) are cylindrical. Similar results are obtained for the films grown on self-assembled iron nanowires with diameters of d = 8 and 45 nm. The resulting shape and diameter of the multi-walled CNT grown on iron nanowires of different diameter and thicknesses is summarized in Table 6.2.

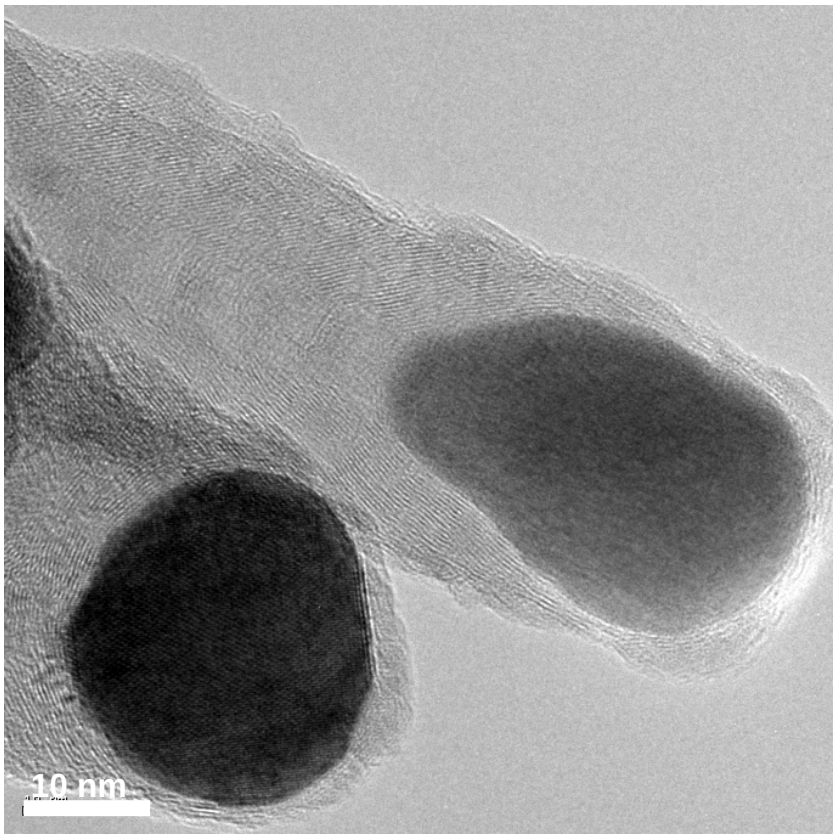

Fig.6.15 TEM images of MWCNFs grown on iron nanowires with diameter and length of d = 8 and l = 90 nm, respectively. The image shows that the graphite basal planes are not parallel to the central axis.

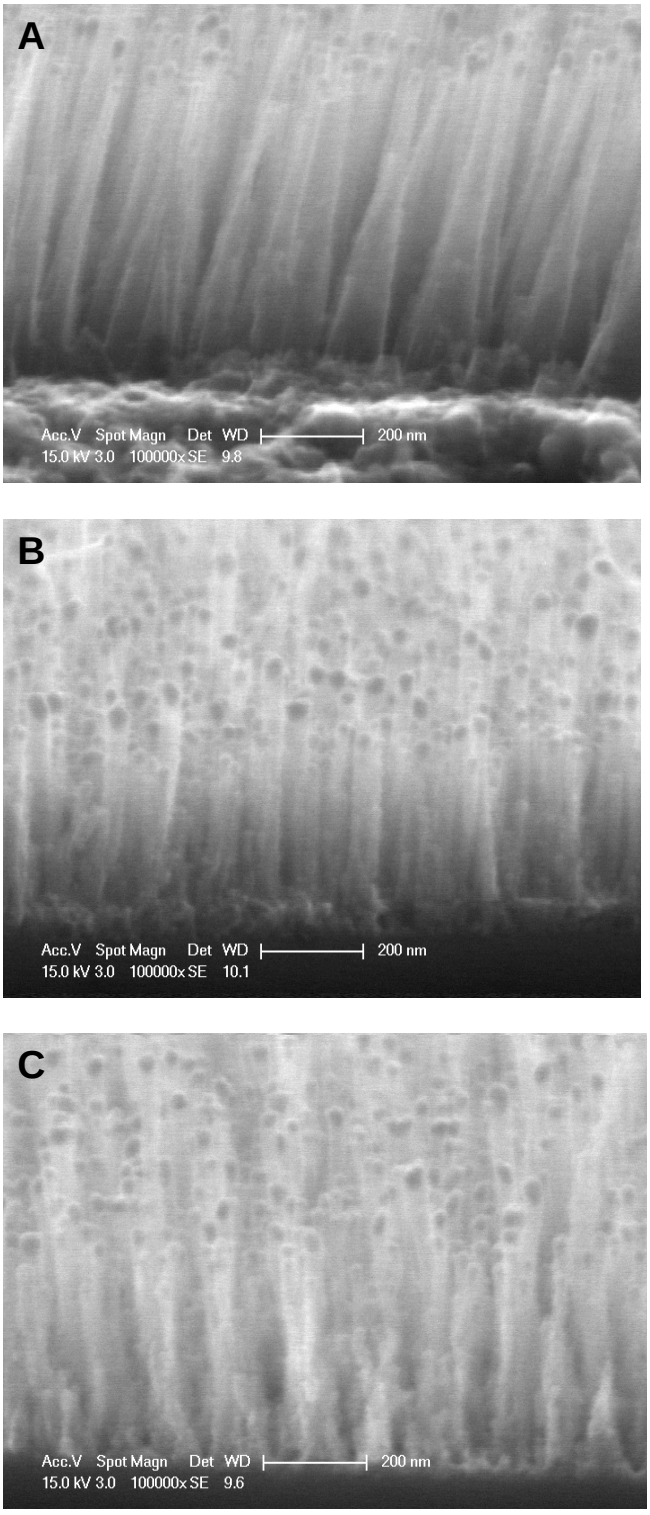

Fig.6.16 ESEM images of the CNTs grown on α-Fe nanowires with diameter of d_{avg} = 17 and length of A. l = 330, B. l = 90, and C. l = 40 nm.

The tip diameter of the vertically aligned carbon nanofibers is approximately equal to that of the catalyst nanoparticle observed on the tip. The initial tip diameter of the CNFs (D) can be roughly estimated from mass conservation of the catalyst as below:

$$D = (\tfrac{3}{2} t d^2)^{1/3} \qquad \text{Eq.6.1}$$

where d is the diameter of the catalyst dot and t is its thickness. Therefore, by knowing the diameter and thickness of the initial α-Fe nanowires, we can theoretically calculate the diameter of the obtained CNFs.

	d = 8 nm			d = 17 nm			d = 45 nm		
	Structure	D (nm) Theory	D (nm) Exp.	Structure	D (nm) Theory	D (nm) Exp.	Structure	D (nm) Theory	D (nm) Exp.
330 nm	Cone	31.6	Tip = 30 Base = 50	Cone	52	Tip = 40 Base = 80	Cone	100	Tip = 55 Base =120
90 nm	Cylinder	20.5	20	Cylinder	34	35	Cylinder	65	55
40 nm	Cylinder	16	18	Cylinder	26	25	Cylinder	49.5	50

Table 6.2 Structure and diameter of the CNFs grown on iron nanowires with different diameter and thickness.

The theoretically calculated values of the diameter of the multi-walled CNFs are summarized and compared to the observed values in Table 6.2. These values suggest that the theoretical calculations and the experimental results are in good agreement

for the CNFs grown on thinner samples where the shape of the MWCNFs is cylindrical. The small difference in the values can be attributed to the error in the averaging of the experimental values for both the CNFs and the diameter of iron nanowires.

The theoretical and experimental values for the diameter of the conical MWCNFs grown on thicker catalysts do not exactly match. To verify the composition of the CNT tip and study the possibility of the existence of other elements in the tip, EDXS analysis was carried out on the tip of the carbon nanfibers. As shown in Fig.6.17, the result of EDXS analysis indicates that the tip of the CNTs contained only iron, and lanthanum and strontium were not present on the tip. This indicates that only iron nanowires are serving as the catalyst and contributing to MWCNF growth.

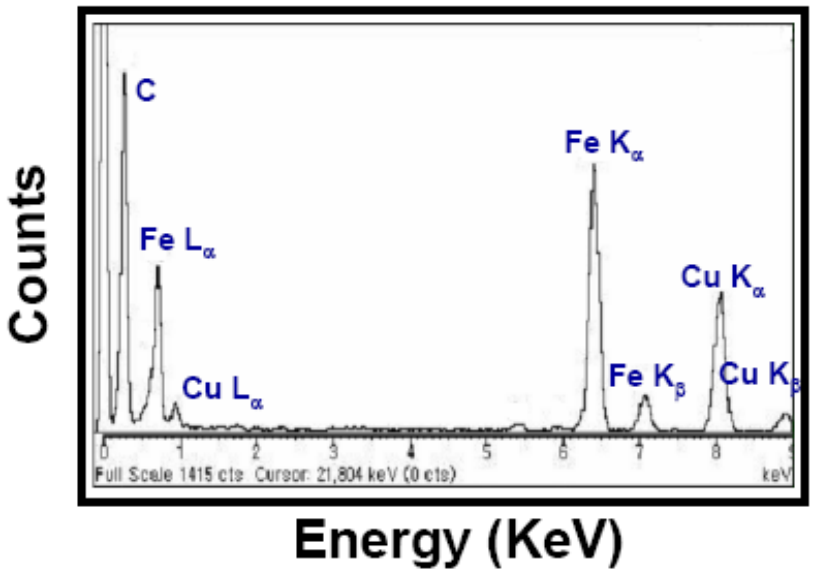

Fig.6.17 EDXS analysis of carbon nanofiber tip showing only iron peaks.

It is interesting that the length of the iron nanowires rather than their diameter is responsible for the transition from conical to cylindrical shape. The data obtained from the films with thickness of l = 180 nm shows that the CNT structure remains cylindrical. Therefore, the transition from cylindrical to conical CNT structure happens somewhere between the thickness of $180 < l < 330$ nm. To determine the approximate thickness at which this transition happens, a sample with diameter of d = 17 nm and varying thickness was prepared. The experiments showed that the transition from cylindrical to conical structure happens at around $l \approx 250$ nm.

The possibility of the formation of nanocones rather than nanofibers was ruled out as the growth condition and acetylene level for all the samples were the same and the growth on different samples was simultaneous. Also, TEM results did not show any indication of the nanocone formation. It is possible that when the length of the iron nanowires catalyst is above a critical limit, the catalysts break into smaller pieces at the initial stages of the growth. Therefore, the growth of CNFs initially starts with a large iron catalyst but when the catalyst breaks, the growth continues with smaller iron catalyst and as a result conical carbon nanofibers form. This can be indirectly proven by the TEM observation of thinner MWCNTs in samples with larger iron nanowires catalyst. Fig.6.18 shows an example of the other MWCNTs grown on samples with thicker iron catalyst along side with conical carbon nanofibers. In this picture the initial iron nanowire catalysts had an average diameter and length of d = 17 and l = 330 nm. The image of the carbon nanotube tip in Fig.6.18 B clearly shows a much smaller catalyst. In addition, as is observed in these images, the graphite basal plane in these carbon nanostructures is parallel to the central axis and multi-walled

carbon nanotubes are formed. Therefore, the difference in the carbon structure can also point to variation in the size of the iron catalyst available. These forms of MWCNTs were unique to the thicker iron nanowires catalyst and similar results were observed for the thicker samples with smaller diameters of d = 8 and 17 nm.

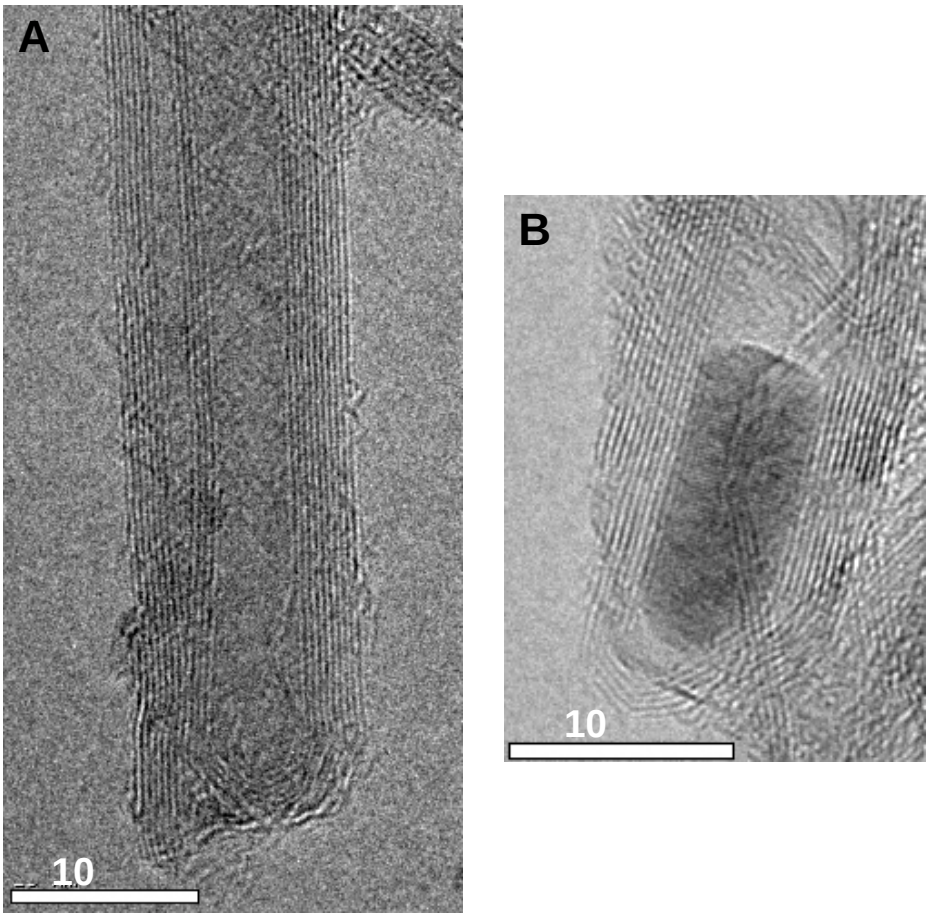

Fig.6.18 TEM images of the thinner MWCNTs grown on top of the iron nanowires with initial diameter and length of d = 17 and l = 330 nm, respectively.

6.7.3 Field emission properties of MWCNFs

Nanotubes compare very favorably with other field emission sources, as they exhibit low operating voltages and produce high current densities. Electron field emission of the carbon nanofibers was measured as a function of applied voltage using a stainless steel anode and a glass spacer. The spacing between the anode and the tip of the CNTs was approximately 0.2 mm. The measurements were performed at room temperature and in a vacuum chamber with a pressure of less than $P \leq 5 \times 10^{-6}$ Torr. Cylindrical carbon nanofibers grown on the iron nanowires catalyst (d = 17 nm and l = 180 nm) were used for FE measurements. The average diameter and length of the MWCNFs were D = 40 and l_{CNT} = 600 nm, respectively. The emission area was 0.5×0.5 cm^2. Fig.6.19 shows the field emission I-V characteristic of the MWCNTs. The emission voltage is high which is expected for catalytic MWCNTs with large diameters. The emission current density reaches 4 μAcm^{-2}.

The logarithmic I-V plot in Fig.6.19 B clearly shows the existence of two exponential regions with different slopes with knee voltage of around $V_{Knee} \approx 985$ volt. A knee voltage is defined as the breakpoint at which the emission data deviate from the low voltage, straight-line asymptote. The field emission data are analyzed using the Fowler–Nordheim model, the most commonly used model for the emission of cold electrons from a metal under a strong applied field. The total current I as a function of the local field at the emitter surface F is given approximately by:

$$I \propto (F^2/\phi)\exp(B\phi^{3/2}/F) \qquad \text{Eq.6.2}$$

with $B = 6.83\times10^9$ ($VeV^{-3/2}m^{-1}$) and ϕ being the work function. F is usually given by:

$$F = \beta E = \beta V/s \qquad \text{Eq.6.3}$$

where V is the applied potential, s is the spacing between cathode and anode, β the field amplication factor, and $E = V/s$ is the macroscopic field. Therefore, when $\ln(I/V^2)$ vs $1/V$ is plotted (Fowler-Nordheim or F–N plot) a straight line should be obtained. The slope of the F-N plot is dependant on ϕ, β and s.

The F-N plot for the MWCNFs grown on self-assembled iron nanowires is plotted in Fig.6.20. The slope of the low voltage regime in this Fowler-Nordheim plot is equal to S = -12856.5. Hence, the field amplification factor (β) can be estimated by taking s = 200 μm and ϕ = 5 eV, as for graphite and C_{60}.

This is valid only as an approximation, as the work functions between the basal plane and the edge plane of the graphite might be different. However, the precise values of work functions depending on the crystallographic surfaces of graphite are not yet known[97]. Assuming the numbers mentioned above, this will result in an amplification factor of β = 1188. The field amplification factor depends directly on the form of the emitter; the value obtained is in very good agreement with the values obtained for multi-walled carbon nanotube [98] and is slightly improved compared to the values reported for catalytic MWCNTs[99].

Additionally, in the frame of the Fowler-Nordheim model, the F-N equation can be rearranged in terms of experimentally measured quantities such as the total current I and applied voltage V:

$$Ln(\frac{1}{V^2}) = \frac{1}{V}(-6.8\alpha R_{tip}\phi^{3/2}) + offset \qquad \text{Eq.6.2}$$

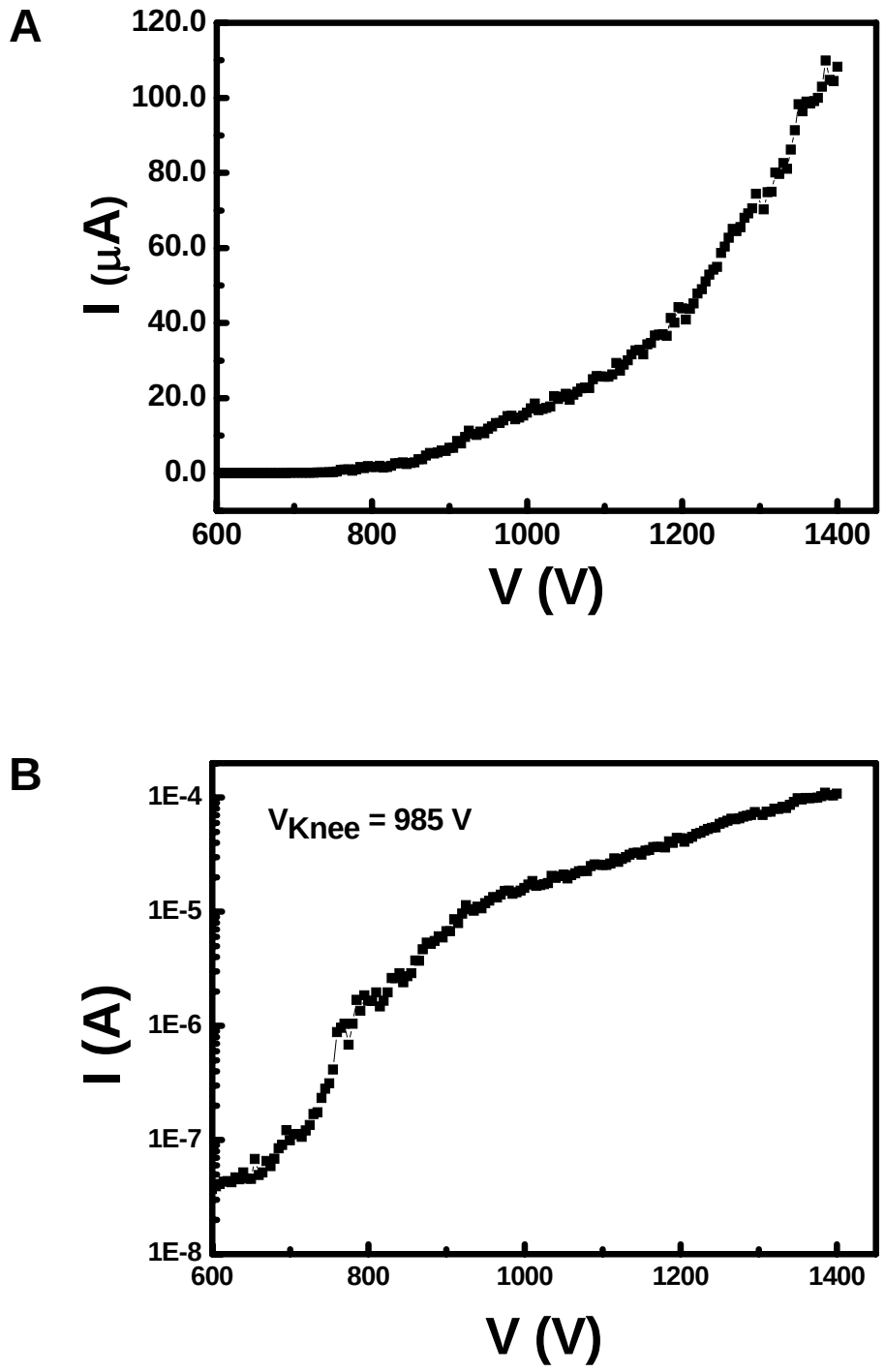

Fig.6.19 Single I-V curve for field emission of the MWCNTs grown on self-assembled iron nanowires, A. linear current scale, B. logarithmic current scale.

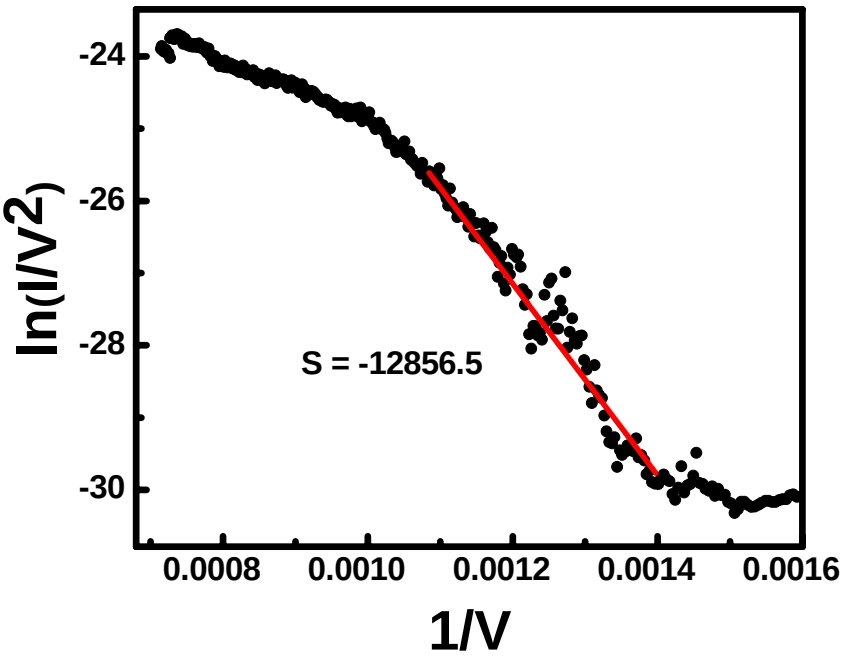

Fig.6.20 Fowler-Nordheim plot for a multi-walled nanotube grown on self-assembled iron nanowires.

where R_{tip} is the radius of curvature in nm and α is a modifying factor determined by local geometric and electronic factors[100]. The modifying factor, α, in the low current regions can be estimated by taking R_{tip} = 20 nm from the ESEM images and ϕ = 5 eV. Taking into account the slope of the F-N plot in Fig.6.20, the modifying factor is calculated to be α = 8.4 which is higher than the theoretical value of α = 5 calculated for an isolated tip shaped as hemisphere which is solely resulted from screening due to image charges. Larger values of α up to 10 have been observed by Collins and Zettl where it also includes the effects of screening by nearby protrusions, including

the nonemitting nanotubes, and the not-so-distant matrix. In addition, α may include electronic effects of the presumably low dimensional nanotubes. Therefore, a value of $\alpha = 8.4$ is not unreasonable for the nanotube emitters[100].

These results indicate that the straight line in the low voltage regime of the I-V plot is in accordance with the Fowler-Nordheim theory. The emitted current begins to saturate and the slope declines and deviates from the F-N theory in the high voltage regime. This saturation behavior in the high voltage regime is attributed to non-metallic characteristics of the carbon nanotube emitters (where the density of states at the tip appears in the form of localized states with well-defined energy levels[98, 101]) or interaction between the neighboring nanotips[100].

As mentioned earlier the emission current density reaches a maximum of 4 μAcm^{-2} in Fig.6.19 A. It has been reported that the emitted current density can be optimized by tuning the density of carbon nanotubes. By comparing the current density versus the distance between the carbon nanotubes, Nillson et al. concluded that three different emission regimes can be defined[102]. Accordingly, emission from low density CNT films is poor because there are few emitting sites of sufficient β factors, whereas emission from densely packed CNT films (as in our case) is poor because of the reduction in the field enhancement factor due to screening effects. In the intermediate regime, the distance between CNTs is sufficient to reach substantial local fields, and the available emitter density is still sufficient for adequate emission currents. Therefore, it was theoretically predicted that an intertube distance of about two times the height of the CNTs optimizes the emitted current per unit area. Suh et al.[103] studied the field-screening effect provoked by the proximity of neighboring

tubes by changing the tube height of highly ordered carbon nanotubes fabricated on porous anodic aluminum oxide templates. They confirmed that the field emission was critically affected by the tube height that protruded from the surface. But their experimental result showed that the field emission was optimal when the tube height was similar to the intertube distance (half of the intertube distance predicted by Nillson et al.). As a result it is possible to improve the current density of the MWCNTs grown on self-assembled iron nanowires by reducing the density of the MWCNTs. This can be achieved by masking, patterning and covering specific areas of the self-assembled iron nanowires catalyst films.

As shown in Fig.6.19, current oscillations in the I-V measurements were observed. We can consider a MWCNT with an iron nanotip with *n* emitting sites and separate the neighborhood of the nanotube tip in three parts a) the nanotube surface having active sites of emission, b) the inner part of the nanotube containing iron nanocrystallites and c) the tip environment. During the field emission process, the carbon nanotubes and the iron nanotips can actively participate in the electron emission process at an applied voltage. Furthermore, the probability of electron emission from these *n* sites depends on defects formed due to the interaction of the electrons emitted from the iron nanotips, and trapping of adsorbents from the tip environment. It should be noted that the thermal expansion of the iron nanotips is distinctly different from that of the carbonaceous nanotube (due to high Z); as a result, Fe nanoparticle also participate in the electron emission process, however, the contribution to the electron emission from Fe nanoparticles is not only due to field applied across the electrode but also due to thermal process in which the tip

temperature reaches $T \sim 1700 - 2000$ °C. These electrons emitted from the iron nanotips when moving towards anode, interact with carbon atoms of the graphene sheet of the nanotube. However, since the energy of these electrons depends on the applied voltage they can dissociate the graphene carbon atoms (bond dissociation energy ~ 1.7 eV) very easily, resulting in defect formation, which lead to the formation of an inactive emission site. If we assume that such *n-j* sites exist, the remaining *j* sites act as active electron emission sites and contribute to the field emission process. The *n-j* sites, which are inactive in electron emission, may actively interact with the tip environment, by acting as the trapping centers for gas molecules, such as hydrogen, oxygen, and nitrogen. During the field emission process, the emitting electrons moving from the cathode to the anode, could ionize these gas molecules near the tip. As a result these metastable ions interact with the *n-j* trapping sites because the activation energy of these trapping sites will be higher than that of the other active *j* sites. It is reported previously that, these gaseous species absorbed in the graphene sheet could also participate in the electron emission process, however, this depends on the electron affinity of the trapped ions with respect to the effective electron affinity of the trap. Considering that such *k* emitting sites exist, where $k \leq j$ and $k < n$, then there will always be fluctuations of the order of $\sim j + k$, in the *j* emitting sites which can lead to local current oscillations arising in I-V measurements.

Chapter 7 Summary and Future Work

This dissertation presented a systematic study of the formation and growth of self-assembled ferromagnetic single-crystal iron nanowires and carefully characterized their magnetic properties. The nanowires are embedded in an antiferromagnetic $La_{1-x}Sr_{1+x}FeO_4$ oxide matrix with its Neel temperature below the room temperature. The formation of these self-assembled iron nanowires takes place during the spontaneous phase decomposition of a perovskite-type oxide, $La_{0.5}Sr_{0.5}FeO_3$. This is a new and exciting method as it can open a new avenue in creating multifunctional metal-oxide or oxide-oxide nanocomposites.

The approach is novel and yet simple in that it combines two basic principles: first, the reduction of $La_{0.5}Sr_{0.5}FeO_3$ perovskite-type oxides under vacuum atmosphere, and second, three-dimensional heteroepitaxy in nanostructure thin film growth. In order to understand the formation and growth mechanism of these self-assembled nanowires, the films were deposited under various conditions by systematically changing the growth temperature, growth rate and film thickness. The thermodynamics and kinetics of the growth were then carefully studied and it was shown that the growth of the nanowires was kinetically controlled by diffusion.

The length of the nanowires is controlled by the film thickness whereas the lateral size of the nanowires can be directly controlled by the growth temperature and/or growth rate. The diameter of the nanowires increases as the growth temperature increases or the growth rate decreases. It has been shown that the lateral size and spacing between the nanowires is proportional to the surface diffusion

distance during the growth before a critical temperature in which the transition from kinetically to thermodynamically controlled growth mode occurs.

The shape of the nanowires evolves from circular to square shapes as the growth temperature and therefore the lateral size of the nanowires increases. This transition happens at a theoretically predicted diameter which takes into account the relative contribution of the surface and elastic energy effects.

The magnetic properties of the self-assembled iron nanowires were measured for all the samples with different length and diameter. The nanowires exhibited a relatively large uniaxial anisotropy with the easy access normal to the film plane (parallel to the nanowires long axis). The theoretical calculations of the anisotropy field show that the anisotropy observed is due to the shape anisotropy and results from the cylindrical shape of the nanowires. For the optimum aspect ratio, almost square shaped out-of-plane hysteresis loops are obtained.

It is believed that this approach, self-assembly of the vertically aligned nanostructures, is generic and can be applied to other metal-oxide or oxide-oxide systems as long as the target phase is reducible and the resulting phases have zero solubility in each other, as well as being epitaxial in-plane and out-of-plane with respect to each other as well as to the common substrate.

It is also shown that the self-assembled single-crystal iron nanowires can be used as the nucleation sites for the growth of the vertically aligned multi-walled carbon nanotubes using a plasma enhanced chemical vapor deposition method. The diameter of the CNTs can be controlled by changing the diameter and length of the iron nanowires catalysts. The low voltage regime of the I-V plot is a straight line

showing that the field emission properties of the nanotubes are in accordance with Fowler-Nordheim theory.

Future work based on this dissertation can be carried out in a few areas:

1. Ferromagnetic nanowires, assembled in a highly ordered fashion, are extremely valuable for applications in perpendicular recording media. However, it is still not clear how long-range order and self-organization can be achieved in these self-assembled nanowires. Increasing the density of the nanowires may lead to self-organization through elastic interaction. However, the increase in the density should be optimized to prevent the nanosized iron nuclei from coalescing and forming larger nanowires. Deposition on carefully engineered and patterned substrates such as vicinal strontium titanate may also help in achieving one dimensional ordering in these nanostructures.
2. Measuring and studying the changes in the resistivity of the metallic nanowires versus their diameter is by itself an interesting study case. However, this measurement is complicated for two reasons: First, the nanowires are deposited in vacuum and both conducting lattice-matched oxides for the bottom electrode, $SrRuO_3$ and $LaSrCoO_3$, lose their conductivity during the heating up process in vacuum. Niobium-doped $SrTiO_3$ substrate could have been a very good option but the polished side of the substrate is not very conductive. The recent growth of the conducting $SrVO_3$ oxide provides a very good lattice-matched conducting substrate to grow self-assembled nanowires as the conductivity of $SrVO_3$ is not dependent on oxygen stoichiometry. The second problem arises from the fact that the contact resistance at the top

electrode is higher than that of the nanowires and makes the measurements inaccurate. Therefore, new and creative methods for measuring the resistivity of the nanowires should be developed. Immersion of the embedded nanowires (with top and bottom electrodes) in a solution of the suspended conductive micro beads can be a starting point.

3. Self-assembled iron nanowires provide an interesting opportunity to study the thermoelectric properties and to understand the heat transport mechanism in crystalline nanostructures. An ideal thermoelectric should have high electrical as well as low thermal conductivity. The thermal conductivity is affected by a) the diffusion of the charge carriers (electrons, holes and ions) which is therefore tied to electrical conductivity and b) phonon scattering. As a result, changes in the scattering of phonons in a material can change the thermal conductivity without affecting its electrical conductivity. It seems it would be possible to control heat transport properties by nanostructuring, but the reason for this and the ways to achieve it have not yet been investigated fully. Usually, heat transport is impeded by phonon scattering in nanostructured materials because of acoustic (lattice vibration) mismatch between the different types of materials. This is strongly correlated with the size of the nanostructures and the type of materials, especially the difference in the mass and bonding strength. In this respect, conductive iron nanowires with different lateral sizes embedded in an oxide matrix can open an exciting door to fundamental understanding of phonon dynamics in nanostructures and their applications as thermoelectrics.

4. Self-assembled iron nanowires present an exciting opportunity for theoretical and experimental research on a new class of compact, electrically tunable, narrow band microwave oscillators. The iron nanowires can simultaneously act as the nano-contact to inject electrons into the underneath layers and as the medium for the spin polarization of these carriers. This dual function eliminates the need for the additional fixed spin polarizing layer, therefore simplifying the design significantly. The preliminary results have indicated a strong ferromagnetic resonance (FMR) response from the iron nanowires. Detailed experimental conduct and analysis are therefore needed to interpret the data and understand the feasibility of using these nanowires as a new generation of microwave oscillators.
5. The effect of annealing in different temperatures and oxygen pressures on iron nanowires can be investigated in more detail. The possibility of the formation of different iron oxide phases such as α-Fe_2O_3, γ-Fe_2O_3 and Fe_3O_4 and understanding the kinetics and thermodynamics of the phase transition in nanoscale by itself is a fascinating study.
6. With respect to using the iron nanowires as a catalyst for nucleation and growth of the carbon nanotubes, and their application as field emitters, creative patterning is necessary to reduce the density of the carbon nanotubes and therefore increase the emission current.

References:

[1] R. L. White, R. M. H. New, and R. F. W. Pease, IEEE Trans. Magn. **33,** 990 (1997).

[2] G. A. Prinz, Science **282,** 1660 (1998).

[3] P. R. Hammar, B. R. Bennett, M. J. Yang, and M. Johnson, Phys. Rev. Lett. **83,** 203 (1999).

[4] D. D. DiVincenzo, J. Appl. Phys. **81,** 4602 (1997).

[5] E. Blums, A. Cebers, and M. M. Maiorov, Magnetic Fluids, de Gruyter, Berlin, (1997).

[6] Magnetism in Medicine, W. Andra and H. Nowak, Eds., Wiley, Berlin, (1998).

[7] C. Haber and D. Wirtz, Rev. Sci. Instrum. **71**, 4561 (2000).

[8] T. R. Strick, J.-F. Allemand, D. Bensimon, and V. Croquette, Biophys. J. **74**, 2016 (1998).

[9] A. K. Salem, P. C. Searson, and K. W. Leong, Nature Mater. **2**, 668 (2003).

[10] J. I. Martín, J. Noguésb, K. Liuc, J. L. Vicente, I. K. Schuller, J. Magn. Magn. Mater. **256**, 449 (2003).

[11] M. Shiraki, Y. Wakui, T. Tokushima, and N. Tsuya, IEEE Trans. Magn. **21**, 1465 (1985).

[12] S. Y. Chou, M. Wei, P. R. Krauss, and P. B. Fischer, J. Vac. Sci. Technol. B **12**, 3695 (1994).

[13] M. Hehn, K. Ounadjela, J. P. Bucher, F. Rousseaux, D. Decanini, B. Bartenlian, and C. Chappert, Science **272**, 1782 (1996).

[14] A. Kuperman, S. Nadimi, S. Oliver, G. A. Ozin, J. M. Garcés, and M. M. Olken, Nature **365**, 239 (1993).

[15] F. Li, and R. M. Metzger, J. Appl. Phys. **81**, 3806 (1997).

[16] G. T. A Huysmans, J. C. Lodder, and J. Wakui, J. Appl. Phys., **64**, 2016 (1988).

[17] R. M. Metzger, V. V. Konovalov, M. Sun, T. Xu, G. Zangari, B. Xu, M. Benakli, and W. D. Doyle, IEEE Trans. Magn. **36**, 30 (2000).

[18] D. J. Sellmyer, M. Zheng, and R. Skomski, J. Phys.: Condens. Matter **13**, R433 (2001) and references therein.

[19] L. Mohaddes-Ardabili, H. Zheng, S. B. Ogale, B. Hannoyer, W. Tian, J. Wang, S. E. Lofland, S. R. Shinde, T. Zhao, Y. Jia, L. Salamanca-Riba, D. G. Schlom, M. Wuttig and R. Ramesh, Nature Materials, **3**, 533 (2004).

[20] L. Mohaddes-Ardabili, H. Zheng, Q. Zhan, S. Y. Yang and R. Ramesh, L. Salamanca Riba, and M. Wuttig, S. B. Ogale and X. Pan, Appl. Phys. Lett., **87**, 203110 (2005).

[21] J. M. D. Tascón, J. L. G. Fierro, L. G. Tejuca, J. Chem. Soc., Faraday Trans. I, **81**, 2399 (1985).

[22] J. B. Yang, W. B. Yelon, W. J. James, Z. Chu, M. Kornecki, Y. X. Xie, X. D. Zhou, H. U. Anderson, A. G. Joshi, and S. K. Malik, Phys. Rev. B **66**, 184415-1 (2002).

[23] A. Chainani, M. Mathew and D. D. Sarma, Phys. Rev. B **48**, 14818 (1993).

[24] G. Chern, W. K. Hsieh, M. F. Tai, and K. S. Hsung, Phys. Rev. B **58**, 1252 (1998).

[25] K. Pohl, M. C. Bartelt, J. de la Figuera, N. C. Bartelt, J. Hrbek, and R. Q. Hwang, Nature **397**, 238 (1999).

[26] H. Takeshida, Y Suzuki, H. Akinaga, W. Mizutani, K. Tanaka, T. Katayama, and A Itoh, Appl. Phys .Lett. **68**, 3040 (1996).

[27] H. Burne, M. Giovannini, K. Bromann, and K. Kern, Nature **394**, 451 (1998).

[28] V. A. Shchukin, and D. Bimberg, Rev. Mod. Phys. **71**, 1125 (1999).

[29] C. Teichert, Physics Report **365**, 335 (2002).

[30] P. Zeppenfeld, M. A. Krzyzowski, C. Romainczyk, R. David, and G. Comsa, Surf. Sci. **342**, L1131 (1995).

[31] Q. Xie, A. Madhukar, P. Chen, and N. P. Koboyashi, Phys. Rev. Lett. **75**, 2542 (1995).

[32] Y. G. Zhao, Y. H. Li, S. B. Ogale, M. Rajeswari, V. Smolyaninova, T. Wu, A. Biswas, L. Salamanca-Riba, R. L. Greene, R. Ramesh, T. Venkatesan, and J. H. Scott, Phys. Rev. B **61**, 4141 (2000).

[33] H. Zheng, J. Wang, S. E. Lofland, Z. Ma, L. Mohaddes-Ardabili, T. Zhao, L. Salamanca-Riba, S. R. Shinde, S. B. Ogale, F. Bai, D. Viehland, Y. Jia, D. G. Schlom, M. Wuttig, A. Roytburd, and R. Ramesh, Science **303**, 661 (2004).

[34] F. Zavaliche, H. Zheng, L. Mohaddes-Ardabili, S. Y. Yang, Q. Zhan, P. Shafer, E. Reilly, R. Chopdekar, Y. Jia, P. Wright, D. G. Schlom,Y. Suzuki, and R. Ramesh, Nano lett. **5**, 1793 (2005).

[35] S. Iwasaki, K. Ouchi, and N. Honda, IEEE Trans. Magn. **5**, 1111 (1980).

[36] T. Wielinger, J.C. Lodder, IEEE Trans. Magn., **6**, 3178, (1981).

[37] C. Brucker, T. Nolan, B. Lu, Y. Kubota, M. Plumer, P-L. Lu, R. Cronch, C-H. Chang, D. Chen, R. Michel, G. Parker, and N. Tabat, IEEE Trans. Magn. **39**, 673 (2003).

[38] B. Lu, T. Klemmer, S. Khizroev, J. K. Howard, D. Litvinov, A. G. Roy, and D. E. Laughlin, IEEE Trans. Magn. **37**, 1319 (2001).

[39] Y. Maeda, and M. Takahashi, IEEE Trans. Magn. **24**, 3012 (1988).

[40] J. C. Slonczewski, J. Magn. Magn. Mater. **159**, L1 (1996).

[41] L. Berger, Phys. Rev. B **54**, 9353 (1996).

[42] M. Tsoi, A. M. G. Jansen, J. Bass, W.-C. Chiang, M. Seck, V. Tsoi, and P. Wyder, Phys. Rev. Lett. **80**, 4281 (1998).

[43] S. I. Kiselev J. C. Sankey, I. N. Krivorotov, N. C. Emley,R. J. Schoelkopf, R. A. Buhrman , D. C. Ralph, Nature **425**, 308 (2003).

[44] W. H. Rippard, M. R. Pufall, S. Kaka, S. E. Russek, and T. J. Silva, Phys. Rev. Lett., **92**, 027201 (2004).

[45] A.N. Slavin and V.S. Tiberkevich, Phys.Rev. **72** , 092407 (2005).

[46] B. K. Kuanr, I.R. Harward, R.T. Deiotte, R.E. Camley, Z. Celinski , J. Appl. Phys. **97**,10Q103-1 (2005).

[47] D. B. Chrisey and G. K. Hubler (Eds.), Pulsed Laser Deposition of Thin Films, John Wiley and Sons, New York: (1994).

[48] M. Lorenz, H. Hochmuth, D. Natusch, M. Kusunoki, V. L. Svetchnikov, V. Riede, I. Stanca, G. Kästner, and Dietrich Hesse, IEEE Trans. Appl. Supercond., **11,** 3209 (2001).

[49] L. Reimer, Transmission Electron Microscopy, Series in Optical Science, **36**, Springer-Verlag, Berlin (1984).

[50] A. Tonejc, Acta Chim. Slov., **46**, 435 (1999).

[51] J. Benedict, R. Anderson, and S. J. Klepeis, MRS Proc., edited by R. Anderson, B. Tray, and J. Bravman, Pittsburgh, USA, **254**,121 (1992).

[52] http://cnsm.kaist.ac.kr/vsm.html

[53] R. Kleiner, D. Koelle, F. Ludwig, and J. Clarke, Proc. IEEE, **92**, 1534 (2004).

[54] http://hyperphysics.phy-astr.gsu.edu/hbase/solids/squid.html

[55] M. Nagao, N. Tanaka, and K. Mihama, Jpn. J. Appl. Phys. **25**, L215 (1986).

[56] A. Catana, R. F. Broom, J. G. Bednorz, J. Mannhart, and D. G. Schlom, Appl. Phys. Lett. **60**, 1016 (1992).

[57] P. Lu, Y. Q. Li, J. Zhao, C. S. Chern, B. Gallois, P. Norris, P. Kear, and F. Cosandey, Appl. Phys. Lett. **60**, 1265 (1992).

[58] M. Atzmon, D. A. Kessler, and D. J. Srolovitz, J. Appl. Phys. **72**, 442 (1992).

[59] V. Moshnyaga, B. Damaschke, O. Shapoval, A. Belenchuk, J. Faupel, O. I. Lebedev, J. Verbeek, G. Van Tendeloo, M. Mücksch, V. Tsurkan, R. Tidecks, and K. Samwer, Nature Mater. **2**, 247 (2003).

[60] T. Omata, K. Ueda, H. Hosono, M. Katada, N. Ueda, H. Kawazoe, Phys. Rev. B **49**, 10194 (1994).

[61] T. Omata, K. Ueda, N. Ueda, M. Katada, S. Fujitsu, T. Hashimoto, and H. Kawazoe, Solid State Commun. **88**, 807 (1993).

[62] T. Omata, K. Ueda, H. Hosono, T. Miyazaki, S. Hasegawa, N. Ueda, and H. Kawazoe, Phys. Rev. B **49**, 10200 (1994).

[63] A. Aharony, R. J. Birgeneau, A. Coniglio, M. A. Kastner, and H. E. Stanley, Phys. Rev. Lett. **60**, 1330 (1998).

[64] R. J. Cava, B. Batlogg, T. T. Palstra, J. J. Krajewski, W. F. Peck, A. Ramirez, and L. W. Rupp, Phys. Rev. B. **43**, 1229 (1991).

[65] G. Le Flem, J. Less-Common Metals **94**, 255 (1983).

[66] J. L. Soubeyroux, P. Courbin, P. Fournes, D. Fruchart, and G. Le Flem, J. Solid State Chem. **31**, 313 (1980).

[67] M. Meixner, E. Schöll, V. A. Shchukin, and D. Bimberg, Phys. Rev. let. **87**, 236101-1 (2001).

[68] F. Léonard, M. Laradji, and R. C. Desai, Phys. Rev. B **55**, 1887 (1997).

[69] M. Meixner, R. Kunert, and E. Schöll, Phys. Rev. B **67**, 195301-1 (2003).

[70] P. Haasen, Physical Metallurgy, 3rd edition, Cambridge University Press, Cambridge, 1996.

[71] J. W. Cahn, and G. Kalonji, Proceedings of an International Conference on Solid-Solid Phase Transformations, Edited by H. I. Aaronson, D. E. Laughlin, R. F. Sekerka, and C. M. Wayman, 3 (1982).

[72] W. C. Johnson, and J. W. Cahn, Acta metal. **32**, 1925 (1984).

[73] M. McCormack, A. G. Khachaturyan, and J. W. Morris J. W., Acta. Metall. Mater. **40**, 325 (1992) and the references there in.

[74]P. Söderlind, R. Ahuja, O. Eriksson, J. M. Wills, and B. Johansson, Phys. Rev. B **50**, 5918 (1994).

[75] W. R. Tyson, and W. A. Miller, Surf. Sci. **62**, 267 (1977).

[76] L. Vitos, A. V. Ruban, H. L. Skriver, and J. Kollár, Surf. Sci. **411**, 186 (1998).

[77] M. J. S. Spencer, A. Hung, I. K. Snook, and I. Yarovsky, Surf. Sci. **513**, 389 (2002).

[78] M. Aldén, H. L. Skriver, S. Mirbt, and B. Johansson, Surf. Sci. **315**, 157 (1994).

[79] E. C. Stoner, and E. P. Wohlfarth, Phil. Trans. R. Soc. A **240**, 599 (1948).

[80] R. Skomski, J. Phys.: Condens. Matter **15**, R841 (2003).

[81] H. Kronmuller, K. D. Durst, and M. Sagawa, J. Magn. Magn. Mater. **74**, 291 (1988).

[82] R. M. Bozorth, *Ferromagnetism*., IEEE Magnetics Society, Piscataway, (1993).

[83] R. Skomski, H. Zeng, M. Zheng and D. J. Sellmyer, Phys. Rev. B **62**, 3900 (2000).

[84] R. Skomski, and J. M. D. Coey, Permanent Magnetism, Institute of Physics, Bristol (1999).

[85] R. H. Baughman, A. A. Zakhidov, and de Heer, W. A., Science **297**, 787 (2002).

[86] R. Saito, G. Dresselhaus, and M. S. Dresselhaus, Physical Properties of Carbon Nanotubes, Imperial College Press, London (1998).

[87] M. Meyyappan, L. Delzeit, A. Cassel, and D. Hash, Plasma Sources Sci. Technol. **12**, 205 (2003).

[88] P. E. Nolan, D. C. Lynch, and A. H. Cutler, J. Phys. Chem. B **102**, 4165 (1998).

[89] P. E. Nolan, M. J. Schable, D. C. Lynch, and A. H. Cutler, Carbon **33**, 79 (1995).

[90] R. T. K. Baker, M. A. Barber, P. S. Harris, F. S. Feates, and R. J. Waite, J. Catal. **26**, 51 (1972).

[91] V. I. Merkulov, A. V. Melechko, M. A. Guillorn, D. H. Lowndes, and M. L. Simpson, Appl. Phys. Lett.**79**, 2970 (2001).

[92] L. Delzeit, I. McAninch, B. A. Cruden, D. Hash, B. Chen, J. Han, and M. Meyyappan, J. Appl. Phys. **91**, 6027 (2002).

[93] A. V. Melechko, V. I. Merkulov, T. E. McKnight, M. A. Gillorn, K. L. Klein, D. H. Lowndes, and M. L. Simpson, J. Appl. Phys. **97**, 1 (2005).

[94] T. Kato, G. H. Jeong, T. Hirata, R. Hatakeyama, K. Tohji, and K. Motomiya, Chem. Phys. Lett. **381**, 422 (2003).

[95] V. I. Merkulov, M. A. Guillon, D. H. Lowndes, M. L. Simpson, and E. Voelkl, Appl. Phys. Lett. **79**, 1178 (2001).

[96] L. H. Chen, J. F. AuBuchon, A. Gapin, C. Daraio, P. Bandaru, S. Jin, D. W. Kim, I. K. Yoo, and C. M. Wang, Appl. Phys. Lett. **85**, 5373 (2004).

[97] Y. Saito, K. Hamaguchi, R. Mizushima, S. Uemura, T. Nagasako, J. Yotani, and T. Shimojo, Appl. Surf. Sci. **146**, 305 (1999).

[98] J-M. Bonard, J-P. Salvetat, T. Stöckli, W. A. de Heer, L. Forró , and A. Châtelain, Appl. Phys. Lett. **73**, 918 (1998).

[99] J-M. Bonard, J-P. Salvetat, T. Stöckli, L. Forró, and A. Châtelain, Appl. Phys. A **69**, 245 (1999).

[100] P. G. Collins, and A. Zettl, Phys. Rev. B **55**, 9391 (1997).

[101] K. A. Dean, and B. R. Chalamala, Appl. Phys. Lett. **76**, 375 (2000).

[102] L. Nilsson, O. Groening, C. Emmenegger, O. Kuettel, E. Schaller, L. Schlapbach, H. Kind, J-M. Bonard, and K. Kern, Appl. Phys. Lett. **76**, 2071 (2000).

[103] J. S. Suh, K. S. Jeong, J. S. Lee, and I. Han, Appl. Phys. Lett. **80**, 2392 (2002).